X-ray Observations of Young Neutron Stars

Marjorie Emily Gonzalez

Physics Department

McGill University

A thesis submitted in partial fulfilment
of the requirements for the degree of

Doctor of Philosophy

Abstract

The extreme physical properties of neutron stars make them efficient emitters at all wavelengths of the electromagnetic spectrum and, traditionally, they have been extensively studied at radio wavelengths. The neutron stars with the highest estimated magnetic fields (so-called "magnetars") have remarkably different characteristics from the rest of the population: they emit no persistent radio emission but show large amounts of high-energy radiation that is thought to be powered by their large magnetic fields. For this thesis we have studied the X-ray emission properties of various types of young neutron stars, discovering unusual characteristics, constraining long-term behaviour and finding associated nebulae.

We have observed the neutron stars PSR B0154+61 and PSR J1119−6127, which have high magnetic fields but otherwise emit normal radio emission. For the latter, unusual thermal X-ray emission was discovered that points to the possible effects of a magnetic field on the surface. Also, this source now represents the youngest neutron star from which thermal emission from the surface has been detected. However, we find no evidence for clear magnetar-like characteristics in these sources. The reason for this discrepancy, as yet unclear and a matter of debate, poses a great challenge to our understanding of the evolution of neutron stars and their emission mechanisms.

We have also studied the long-term properties of the 'anomalous X-ray pulsar' 4U 0142+61, thought to be a magnetar. We find that changes are present in almost all of its emission characteristics over the last 7 years. The observed changes agree with the general predictions made by the magnetar model of such sources. However, the details of these changes suggest that further work is still needed on the expected emission from these objects.

In addition, neutron stars are seen to power extended structures, called pulsar wind nebulae (PWNe), which can radiate large amounts of high-energy emission. Here we also present the discovery of one such nebula around the young, energetic neutron star PSR B1046−58. While both the star and its PWN are possible γ-ray sources

(a very unusual characteristic), we find that their X-ray emission is similar to those seen around other neutron stars with similar ages and energetics. The nebula has a peculiar morphology and we explore various scenarios to account for its properties. The discovery of this nebula presents a new testing site for current theories of PWNe production and emission characteristics.

Résumé

Les propriétés extrêmes des étoiles à neutrons font de ces objets compacts des émetteurs efficaces dans toutes les longueurs d'ondes du spectre électromagnétique. Cependant, elles ont historiquement été étudiées principalement dans les ondes radios. Les étoiles à neutrons ayant un fort champ magnétique (appelées "magnétars") ont des caractéristiques remarquablement différentes du reste de la population: elles n'émettent pas d'ondes radios mais elles présentent de grandes quantités de radiations à haute énergie causées par le champ magnétique. Pour ce projet, nous avons étudié les propriétés des rayons X provenant de différents types de jeunes étoiles à neutrons, découvert des caractéristiques inattendues, contraint le comportement à long terme et enfin trouvé des nébuleuses associés aux étoiles à neutrons.

Tout d'abord, nous avons observé les étoiles à neutrons PSR B0154+61 et PSR J1119–6127. Ces deux objets ont un fort champ magnétique mais ils émettent cependant des ondes radios normales. Pour la seconde, des émissions de rayons X thermiques ont également été découvertes, ce qui suggère les possibles effets du champ magnétique sur la surface. Aussi, cette source est maintenant la plus jeune étoile à neutrons émettant une radiation thermique depuis sa surface. Il n'y a cependant aucune preuve permettant d'associer ces sources aux caractéristiques des magnétars. La raison de cette différence, toujours incomprise et sujette à de nombreux débats, pose un énorme défi à notre compréhension de l'évolution des étoiles à neutrons et de leurs mécanismes d'émission.

Ensuite, nous avons également étudié les propriétés à long terme du "pulsar anormal à Rayons X" 4U 0142+61, que l'on pense être un magnétar. Nous trouvons des changements de presque toutes ces caractéristiques d'émission sur les 7 dernières années. Les variations observées sont en accord avec les prédictions suggérées par le modèle "magnétar" de telles sources. Cependant, les détails de ces changements requièrent des études plus profondes sur les émissions attendues provenant de ces objets.

Enfin, des étoiles à neutrons ont été observé produisant des structures étendues, appelé “Pulsar Wind Nebulae” (PWNe, de l’anglais signifiant nébuleuse de vent de pulsar), pouvant émettre de larges quantités de radiations à haute énergie. Nous présentons également dans cette thèse la découverte d’une telle nébuleuse autour de la jeune et énergétique étoile à neutron PSR B1046–58. Bien que l’objet lui-même et sa nébuleuse sont des possibles émetteurs de rayons Gamma (caractéristique très inhabituelle), nous trouvons que leur émission de rayons X est comparable à celle d’autres étoiles à neutrons ayant un ge et une énergie similaires. La nébuleuse observée a une morphologie particulière et nous explorons les différents scénarios pouvant conduire à de telles propriétés. La découverte de cette nébuleuse se présente comme un nouveau test des théories de formation des PWNe et de leur émissions.

Acknowledgements

I would like to give many thanks to my supervisor, Vicky Kaspi. The incredible dedication she has to her family, our group and the research field are inspiring in many, many ways. The work done during this thesis would not have been nearly as enjoyable or as scientifically enriching as it was without her enthusiasm, patience, kindness, knowledge and experience. The large group of dedicated postdocs and graduate students that she fearlessly leads is a testament to her seemingly endless energy. It would be hard to think of a more deserving person for all the praise and respect that she (humbly) receives.

It was not only a pleasure and honor to work with Vicky during this time, but also with the rest of the great people in the pulsar group at McGill. To give a complete list (and prove what I mean by 'large group' above), past and present members while I was here include: Anne Archibald, Cees Bassa, René Breton, David Champion, Rim Dib, Fotis Gavriil, Claude-André Giguère, Jason Hessels, Patrick Lazarus, Maggie Livingstone, Mallory Roberts, Cindy Tam, Zhongxiang Wang, and WeiWei Zhu.

Within my first year at McGill, I was part of the initial group of astrophysics grad students who moved to the second floor of the physics building in order to, partly, warn the rest of the research groups of our firm intention to take over the floor. Unfortunately, this came at the price of losing natural sunlight in our office. Luckily, this sacrifice was made more than bearable, enjoyable even, thanks to the great officemates I was happy to have with me. Among them were: René Breton, Jon Dudley, Alex van Engelen, Kelsey Hoffman, Dan O'Donnell, and Yoshi Yamamoto.

I am also happy to count most of the above people as my friends as well as colleagues. The list would not be complete without Rhiannon Gwyn, Audrey MacLeod and many more McGill students, you know who you are. All of you made grad school as enjoyable an experience as it's expected to be, and much more! I will miss our get-togethers, late-night parties, curry runs, philosophical conversations, silly dances, and the things that made all of you such a great bunch of people to be around.

I would also like to thanks the co-authors in the articles written during my degree who have not been mentioned above, especially Bryan Gaensler, Fernando Camilo and Pete Woods, for their help and very valuable insights. In addition, the research presented in this thesis has been been generously funded by various Canadian and international agencies including the FQRNT, NSF, and CFI. I would personally like to thank the Natural Science and Engineering Research Council of Canada (NSERC) for their support during my masters, Ph.D., and my upcoming postdoc position. It's been much appreciated.

Furthermore, I would like to say thanks to all the great people I worked with while volunteering for "Let's Talk Science"[1], especially Isabel Deslauriers, Karen Lee and Sarah Wilson. Their dedication and enthusiasm for the program made it easier for me to remember how lucky we are to be members of the scientific community and how important it is that we share our knowledge with young people and the general public. Seeing the effect that the program has on students and how much our help is needed and valued in the education system made all the hard work worth it.

Last, but definitely not least, I would like to thank my parents for their unconditional love and support. Neither living in El Salvador nor immigrating to Canada was easy, and I am incredibly grateful for everything that you've done for us. If I am here it's because of you. To my brothers, Edgar and Fernando, I would like to thank you for keeping me up to date with everything that's going on outside of physics (yes, there's a world out there!). It seems amazing to me that you are both in University already, but I am very proud of the people you have become and I'm glad to be your older sister. Para mi familia y amigos en El Salvador, ustedes son la razón por las que creo que el país puede salir adelante. Siempre los llevamos con nosotros y siempre vamos a estar aquí cuando nos necesiten. Los quiero mucho a todos, y cuando estemos juntos vamos a celebrar como se debe, con pupusas y todo.

[1] http://www.medicine.mcgill.ca/expmed/LTSM/

The work presented in this thesis has made use of state-of-the-art facilities. The *Chandra* X-ray Observatory is operated by the National Aeronautics and Space Administration (NASA). *XMM–Newton* is operated by the European Space Agency (ESA). *Swift* is operated by an international consortium from the United States, United Kingdom, and Italy. The Gemini Observatory is operated by the Association of Universities for Research in Astronomy, Inc., under a cooperative agreement with the NSF on behalf of the Gemini partnership: the National Science Foundation (United States), the Particle Physics and Astronomy Research Council (United Kingdom), the National Research Council (Canada), CONICYT (Chile), the Australian Research Council (Australia), CNPq (Brazil) and CONICET (Argentina). This work has also made use of archival data obtained through the High Energy Astrophysics Science Archive Research Center (HEASARC), provided by the NASA/Goddard Space Flight Center.

Preface

Statement of Originality

The results presented in this thesis are original work that was, or will be, published in the following refereed articles:

Chapter 3 *Gonzalez, M. E.*, Kaspi, V. M., Lyne, A. G., & Pivovaroff, M. J., An XMM-Newton Observation of the High Magnetic Field Radio Pulsar PSR B0154+61, Astrophysical Journal Letters, 610, L37−L40, 2004.

Chapter 4 *Gonzalez, M. E.*, Kaspi, V. M., Camilo, F., Gaensler, B. M., & Pivovaroff, M. J., Unusual Pulsed X-Ray Emission from the Young, High Magnetic Field Pulsar PSR J1119−6127, Astrophysical Journal Letters, 630, 489−494, 2005, and

Gonzalez, M. E., Kaspi, V. M., Camilo, F., Gaensler, B. M., & Pivovaroff, M. J., PSR J1119−6127 and the X-ray emission from high magnetic field radio pulsars, Astrophysics and Space Science, 308, 89−94, 2007

Chapter 5 *Gonzalez, M. E.*, Dib, R., Kaspi, V. M., Woods, P. M., Tam, C. R., & Gavriil, F. P., Long-term X-ray changes in the emission from the Anomalous X-ray Pulsar 4U 0142+61, Astrophysical Journal, submitted, 2007

Chapter 6 *Gonzalez, M. E.*, Kaspi, V. M., Gaensler, B. M., & Pivovaroff, M. J., Chandra and XMM-Newton Observations of the Vela-like Pulsar PSR B1046−58, Astrophysical Journal, 652, 569−575, 2006

These papers show the derived characteristics of a number of neutron stars obtained from X-ray observations. The non-thermal X-ray emission seen from rapidly-spinning neutron stars (called "pulsars") is thought to be powered by the loss of rotational kinetic energy due to magnetic dipole radiation. Thermal X-ray emission from the surface of young stars is thought to arise from the hot interior as it cools due to

a number of possible high-density processes or to arise from heated regions due to accelerated particles striking the surface from the magnetosphere. In turn, the large amount of high-energy radiation, persistent and in bursts, seen from neutron stars with the highest magnetic fields ("magnetars") is thought to be powered by the decay of this field.

In Chapters 3 and 4 we present observations of two pulsars that appear to be normal rotation-powered sources, yet have large magnetic fields close to those of magnetars. Unusual thermal emission is detected from one of these pulsars and points to the possible effects of a large magnetic field on the temperature distribution of the surface. However, no magnetar-like emission was detected for these sources and none has been reported for similar objects. The reason for this discrepancy posses a great challenge to our understanding of the evolution and emission processes of neutron stars.

In Chapter 5 we present a study of the long-term evolution in the emission of a well-established magnetar. We find that changes to all of its emission properties are present, supporting the view that they are very active sources. We also find that the largest changes in the emission are seen to coincide with a period of increased burst activity from this previously stable source. The properties of these changes are seen to agree with the predictions made by current magnetar models of these sources. However, the detailed properties of the source before the observed bursts cannot be completely accounted for with these models and suggest that additional emission processes and/or improved models are needed.

In Chapter 6 we report the discovery of a faint, arc-second nebula powered by a young, rapidly-rotating neutron star. The nebula is highly asymmetric about the star and various mechanisms for the origin of this morphology are explored. The observed properties of the system suggests that emission from both the magnetosphere and from the surface of the star are present. The size and energetics of the nebula are consistent with those of other nebulae found to be powered by neutron stars with similar properties. In addition, the star and/or its nebula are also possible γ-ray sources that will likely be confirmed (or not) as such with current and future telescopes.

Contribution of Authors

Here I would like to acknowledge the contribution of my coauthors in the above manuscripts. Victoria M. Kaspi played a crucial role in the scientific content and interpretation of all results. The bulk of the data presented here were reduced and analyzed by myself with software provided by the operating centres for the corresponding observatories. In the case of individual papers the following contributors deserve mention:

Chapter 4 (Gonzalez, Kaspi, Camilo, Gaensler & Pivovaroff, 2005 and 2007): Fernando Camilo provided the radio ephemeris of the pulsar so that the X-ray pulse properties could be studied and the phase offset between the radio and X-ray profiles could be constrained. Fernando Camilo and Bryan M. Gaensler provided valuable comments during the writing process of the manuscript.

Chapter 5 (Gonzalez, Dib, Kaspi, Woods, Tam & Gavriil, 2007): Rim Dib contributed the updated *RXTE* results presented here. Cindy Tam provided the Gemini observations and results. Peter M. Woods provided the reduced *Chandra* and *Swift* data and I performed the spectral and pulse analyses. He also reanalyzed some of the *XMM–Newton* data to confirm our results. All authors provided valuable comments during the writing process.

Chapter 6 (Gonzalez, Kaspi, Gaensler & Pivovaroff, 2006): Michael J. Pivovaroff initially analysed the *XMM–Newton* data, providing a cross-check for the results obtained here. Bryan M. Gaensler provided valuable comments on the manuscript.

Para toda mi familia y para...

"los sembradores de maíz en plena selva extranjera,
los que nunca sabe nadie de dónde son,
los mejores artesanos del mundo,
los hacelotodo, los vendelotodo, los comelotodo,
los tristes más tristes del mundo,
mis compatriotas,
mis hermanos."
– Roque Dalton, "Poema de amor" (partes)

Table of Contents

List of Figures

List of Tables

Chapter 1

Introduction

"How big is the biggest of its kind? And how did it get to the point where the conditions called for something so massive to be constructed? It's baffling. Beautiful though."
– Jack White

Neutron stars (NSs) represent some of the most extreme objects in the Universe due to their high density, high magnetic fields, and large rotation speeds. The study of their properties provides important insights into the processes that govern such extreme areas of physics that cannot be reproduced in laboratory experiments. The wide range of observational properties seen in NSs is thought to reflect the various formation and evolutionary mechanisms they can follow. NSs also emit radiation at all wavelengths of the electromagnetic spectrum, attesting to the varied physical processes associated with them. In this chapter we will review our current physical understanding of these objects (§1.1–1.4) and their observed characteristics (§1.5–1.8).

1.1 A (Very Short) History of Neutron Stars

After the discovery of the neutron by Chadwick in 1932, Walter Baade and Fritz Zwicky brought forward the idea that a condensed star made up of neutrons would be the end product of stellar evolution as follows: "With all reserve we advance the view

that a super-nova represents the transition of an ordinary star into a *neutron star*, consisting mainly of neutrons. Such a star may possess a very small radius and an extremely high density" (Baade & Zwicky, 1934). Oppenheimer and Volkoff (1939), making use of results obtained by Tolman (1934), presented the first upper limit for the mass of a star composed of degenerate neutron matter. Observationally, by the 1960s astronomers had found a star near the centre of the Crab nebula and estimated that large magnetic fields must be present inside the nebula. In 1967, Pacini proposed that a rapidly rotating neutron star, with a strong dipolar magnetic field, would act as a very energetic electric accelerator and could provide the source of energy for radiation from a surrounding nebula, such as the Crab.

In late 1967, the first four pulsating radio sources (now called "pulsars") were discovered by Anthony Hewish and his graduate student Jocelyn Bell. The nature of the observed signals required compact and distant sources. Their discovery paper (Hewish et al., 1968) proposes oscillations from white dwarfs or NSs as a possible origin. Theories involving compact binary systems were ruled out after the slow increase in the period of the signals was confirmed (as opposed to the decrease that would be expected from the loss of energy in the form of gravitational radiation from a compact binary). The lower limits on the period of rotating white dwarfs were found to be too large to account for the slowest periods observed from these objects. Gold (1968) and Pacini (1968) were the first to correctly identify the newly found objects as rotating NSs.

In the 40 years since their discovery, NSs have established their place as prime testing sites for physics under extreme conditions.

1.2 Neutron Star Basics

The stable configuration of normal stars is dictated by the balance in hydrostatic equilibrium between gravity and thermal pressure (see Page et al., 2006, for a recent review). The cores of stars with masses below $\sim$8 $M_{\odot}$ are believed to collapse into white dwarfs after they run out of nuclear fuel to sustain the thermal pressure. Stars

with masses higher than $\sim$40 $M_\odot$ are believed to produce compact cores massive enough to result in black holes (e.g., Muno, 2007, and references therein). Stars of intermediate masses are thought to produce cores where the large gravitational pressure makes it energetically favorable for electron capture to occur:

$$p^+ + e^- \rightarrow n + \nu_e. \tag{1.1}$$

The star will then be supported against gravity due to neutron degeneracy pressure and will have an estimated average density of $\sim 7\times10^{14}$ g cm^{-3}.

The inner structure of NSs is thought to be as follows (see also Figure 1.1). The surface of the star, with an estimated density of 10^4–10^6 g cm^{-3} is composed of normal nuclei and non-relativistic electrons. The thermal radiation observed from NSs is emitted from this region, while the source of the radiation is thought to be nuclear processes taking place at the inner layers (such as modified Urca, see §1.4.3). As the density increases to $\rho < 4\times10^{11}$ g cm^{-3}, the electrons form a relativistic electron gas and the atomic nuclei form a solid Coulomb lattice while becoming neutron-rich due to electron capture. At densities of $\sim 4\times10^{11}$ g cm^{-3}, enough energy is available so that the lowest energy state is one where neutrons *drip* out of the neutron-saturated nuclei and populate free energy states outside of them. At these densities, the star contains a mixture of neutron-rich nuclei in a lattice, non-relativistic free neutrons and relativistic free electrons. The free neutrons will pair, resulting in a bosonic fluid in its lowest energy state that will flow without resistance (a *neutron superfluid*). Neutron degeneracy pressure takes over from electron degeneracy pressure at densities of $\sim 4\times10^{12}$ g cm^{-3} and holds the star up against gravitational pressure (see, e.g., Carroll & Ostlie, 1996, for a review).

At densities close to the nuclear density ($\rho_c \sim 2.3\times10^{14}$ g cm^{-3}), the neutron-rich nuclei dissolve into their individual components, creating a mixture of free neutrons, protons and electrons. The positively-charged protons pair to form a superfluid which is also *superconducting* and thus has no electrical resistance. The properties of this mixture at densities $\rho > \rho_c$ is not well understood. The physics is made

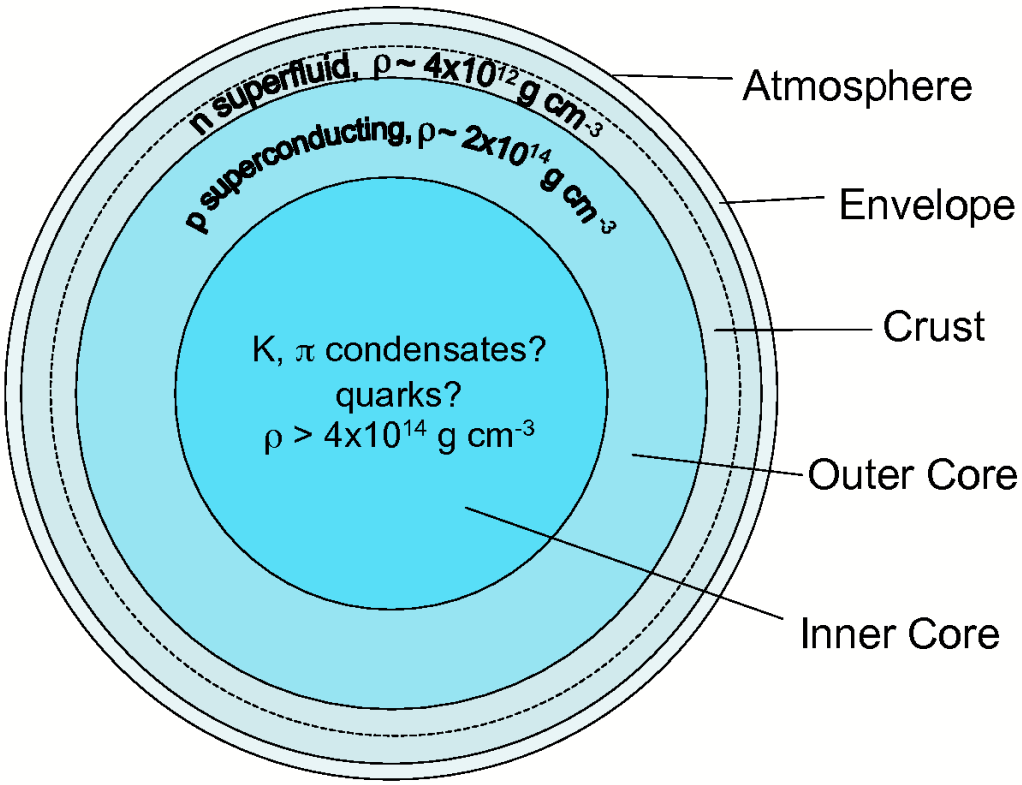

Figure 1.1: Estimated structure of a neutron star. The core, with extremely high densities and largely unknown physical properties, makes up most of the star. The dashed line separates the inner and outer crusts, defined as the transition towards neutron drip. The transition to the inner core occurs when densities reach nuclear values.

more uncertain by the possibility that additional particles might be created, such as negatively-charged pions through the process: $n \rightarrow p^{+}+\pi^{-}$, which is expected to become important at densities $\rho > 2\rho_c$.

Therefore, the density of matter inside NSs spans an incredibly large range, from atomic densities on the surface to supernuclear densities in the core. The functional dependence of pressure on density at every density range ($p \propto p(\rho)$, the so-called *equation of state*) is fundamental for our understanding of the basic properties of NSs and the physical phenomena associated with them.

1.3 Pulsar Basics

As the progenitor star collapses, it is thought that conservation of angular momentum and conservation of magnetic flux will give rise to a rapidly-rotating and highly-magnetized NS[1]. Wherever we detect emission only at specific phases of their rotation they are detected as pulsating sources and are known as pulsars (PSRs, see Figure 1.2). The dipole magnetic fields of NSs are estimated to span the range of 10^{8}–10^{14} G. Despite these extremely large values, the magnetic field is not thought to be strong enough to affect the internal structure of the star. However, the large field directly affects the properties of the star close to the surface and completely dominates the physical processes associated with the outside of the star.

The rotation periods of pulsars span the range of 1.39 ms to tens of seconds and these periods are found to increase with time with an average rate of $\dot{P} = dP/dt$ $\sim 10^{-14}$–10^{-16} (although the full range of values is much larger, see Figure 1.7). These characteristics are understood in light of a strong dipole field that is misaligned with the rotation axis of the star (see Figure 1.2). As the star rotates, it will emit electromagnetic radiation at the rotation frequency and lose rotational kinetic energy

[1] See §1.4.2 for further discussion on the origin of magnetic fields in neutron stars.

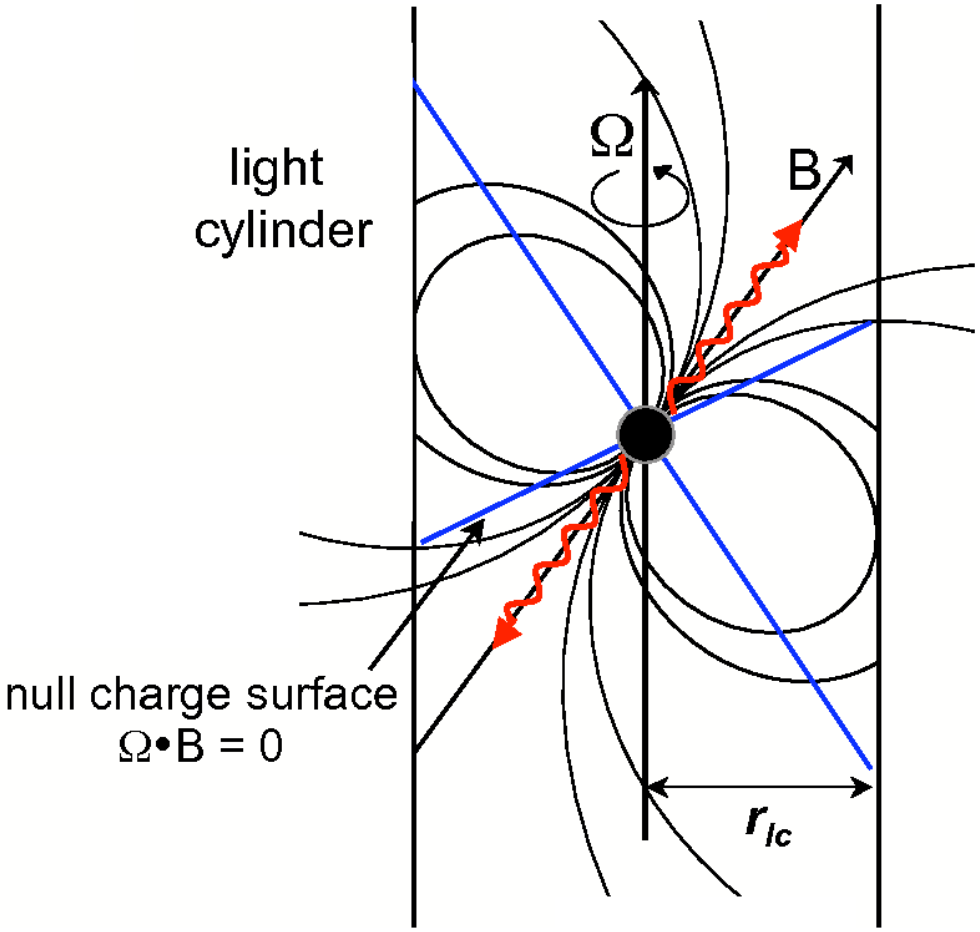

Figure 1.2: Schematic of a pulsar and its magnetosphere. In this case the rotation and magnetic axes are misaligned. The light cylinder radius is shown. The null charge density lines ($\mathbf{\Omega} \cdot \mathbf{B} = 0$) separate the regions of positive and negative charges. Radiation beams inclined to the rotation axis will then result in periodic signals if they are intercepted by our line of sight and the star will be detected as a pulsar.

in the process. A local electric field is also induced by the rotating magnetic field:

$$\mathbf{E} = -\frac{1}{c}(\mathbf{\Omega} \times \mathbf{r}) \times \mathbf{B}. \tag{1.2}$$

The electric field overcomes the pull of gravity by many orders of magnitude and lifts charged particles from the surface. The structure of the induced electric field and its associated particle charge density is a quadrupole. The charge density is estimated to be $\rho = \mathbf{\Omega} \cdot \mathbf{B}/2\pi c$ and its distribution in the magnetosphere is bounded by the surface $\Omega \cdot \mathbf{B} = 0$ (see also §1.4.4). The magnetosphere is filled with plasma and moves with the star as it rotates. At a distance from the star of $r_{lc} = c/\Omega$ the rotation speed of the magnetosphere would have to exceed the speed of light. Outside this region (called the *light cylinder*) magnetized plasma leaves the system and produces a pulsar "wind". The continuous ejection of these particles and accompanied magnetic fields is believed to power the extended nebulae associated with energetic pulsars, the prime example of which is the Crab nebula.

Inside the light cylinder, the induced electric field accelerates charged particles to relativistic speeds. In turn, moving electrons that interact with a magnetic field are expected to emit synchrotron radiation if the motion is circular around the magnetic field lines and curvature radiation if the motion is primarily along the field lines (see, e.g., Rybicki & Lightman, 1979). This radiation is emitted in a narrow beam parallel to the instantaneous direction of motion of the electrons. The accelerated electrons are thought to produce very high energy γ-rays through curvature radiation as they accelerate along the curved field lines. These γ-rays would be energetic enough to spontaneously produce electron-positron pairs ($\gamma \rightarrow e^- + e^+$) which would in turn radiate themselves. A cascade of pair-production begins, the products of which are thought to be responsible for the observed magnetospheric emission from pulsars across the electromagnetic spectrum.

1.4 Properties of Neutron Stars

Due to the immense range of physical properties they exhibit, NSs are considered prime testing sites for current theories of nuclear physics, particle physics, general relativity, plasma physics and more. As such, the interplay between their observed characteristics and theoretical expectations can help us gain insight into the properties of matter that are not achievable in laboratory experiments.

1.4.1 Masses and Radii

The global structure of the interior of a NS is determined by solving the equations of hydrostatic equilibrium (see Lattimer & Prakash, 2007, for a recent review). These depend mainly on the nature of strong forces for matter at high densities, which are currently not well understood. Several possible models have been explored in the frameworks of general relativity, field-theory and non-relativistic potential models. As an example, in general relativity and for a spherical object, the Einstein Field Equations can be solved to give the following expressions for hydrostatic equilibrium:

$$\frac{dP}{dr} = -\frac{G(m(r) + 4\pi r^3 P/c^2)(\rho + P/c^2)}{r(r - 2Gm(r)/c^2)}, \qquad \frac{dm(r)}{dr} = 4\pi\rho r^2, \tag{1.3}$$

where P and ρ are the pressure and mass-energy density, respectively, and $m(r)$ is the gravitational mass enclosed in a radius r (Lattimer & Prakash, 2001, and references therein). Properties such as the mass, radius and moment of inertia are obtained by numerically solving these equations for realistic models of the P-ρ relationship (the equation of state, EOS).

Figure 1.3 shows the predicted M-R relationships for various EOSs. Traditionally, EOSs where the radius depends weakly on mass at specific ranges are referred to as "hard", while those showing the opposite behavior are called "soft" EOSs. The observed radius of the star measured at Earth will be redshifted to a valuef of $R^{\infty} = R(1-2GM/Rc^2)^{-1/2}$. For EOSs describing so-called "normal" NSs, the radius is found to be nearly independent of mass and strongly dependent on the pressure of matter around ρ_c. This effect can be seen in Figure 1.3, where estimated radii remain almost

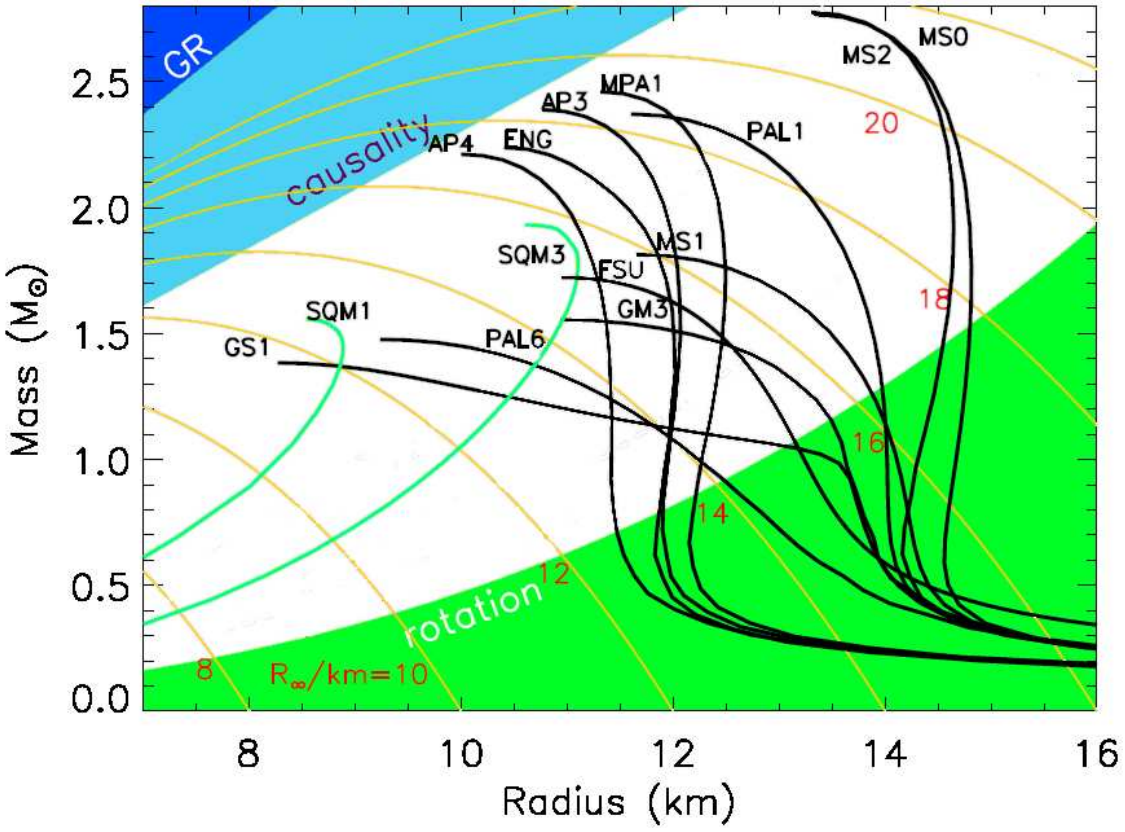

Figure 1.3: Mass–radius curves for various equations of state (EOS). Typical NS curves are shown in black, while self-bound quark stars are shown in green (SQM1, SQM3). Orange curves represent redshifted values of the radii to infinity. The dark blue region shows the parameter space eliminated by the General Relativity constrain that $R > 2GM/c^2$. The light blue region is eliminated by causality, $R \gtrsim 3GM/c^2$. The green region is eliminated by the requirement that the fastest spinning NS should remain gravitationally bound against centrifugal forces, giving $R \lesssim 13\ {\nu_{716}}^{-2/3}\ {M_\odot}^{1/3}$ km, where $\nu_{716} = 716$ Hz as observed for the pulsar J1748-2446ad (Hessels et al., 2006). Adapted from Figure 2 of Lattimer & Prakash (2007).

independent of mass in the range ∼1–1.5 $M_\odot$ for a large number of EOSs. However, nuclear matter studied in laboratory experiments has a proton fraction of ∼1/2, while in NSs this fraction is expected to be <0.1. The extrapolation of the associated energy and pressure in the neutron-rich case is highly uncertain and different EOSs predict pressures at densities close to ρ_c that differ by a factor of ∼6. This accounts for the ∼50% variations in the radius that is seen for various EOSs. Allowing for exotic particles to become abundant (such as hyperons, kaons, pions) at high densities is predicted to result in softer equations of state (such as that labeled GS1 in Figure 1.3).

An upper limit to the radius of a neutron star can be made by excluding the parameter space that violates the General-relativistic radius of an object of mass M, $R > 2GM/c^2$. A larger parameter space can be excluded by requiring that the speed of sound inside the object does not exceed the speed of light (called the "causality" constraint), estimated to give $R \gtrsim 3GM/c^2$ (e.g., Lattimer & Prakash, 2007). These regions are shown in Figure 1.3. In turn, the lowest allowed mass for a normal NS is $\sim 0.1 M_\odot$. However, the accepted minimum mass lies in the range ∼1.0–1.2 $M_\odot$, derived from the estimated minimum mass of a proto-NS after the collapse of the progenitor. The maximum accepted mass for a neutron star is ∼3 $M_\odot$, this being the limit implied from causality. In general, radii at infinity of ∼12–20 km are possible for NSs with masses $\gtrsim$1 $M_\odot$ (see §1.4).

Normal EOSs have vanishing pressure as the density goes to zero. However, "self-bound" EOSs have a pressure that vanishes at a non-zero density and are thought to represent the behavior of strange quark matter (SQM). These self-bound stars have finite density but zero pressure at their surfaces and no minimum mass.

1.4.2 Magnetic Fields

Magnetic main sequence stars (with fields in the order of 10^3 G) and magnetic white dwarfs (with fields of tens of MG) are good candidates to provide the initial fields needed to result in highly magnetised NSs by conservation of magnetic flux as

they collapse. The flux of a magnetic field through a surface $\mathcal{S}$ is defined by:

$$\Phi \equiv \int_{\mathcal{S}} \mathbf{B} \cdot d\mathbf{A}. \tag{1.4}$$

Conservation of this flux as the area changes results in the condition: $B_i 4\pi R_i^2 = B_f 4\pi R_f^2$, where i and f denote the initial and final values, respectively. For example, the collapse of a magnetic white dwarf with an initial field $B_i = 5{\times}10^6$ G and radius $R_i = 5{\times}10^7$ cm results in a field of

$$B_f = B_i \left(\frac{R_i}{R_f}\right)^2 \sim 10^{14} \text{ G}. \tag{1.5}$$

The values are high enough to account for the large fields estimated to be present in NSs. However, it is unclear whether magnetic progenitors can account for the large number of magnetars (NSs with estimated fields at the surface of $\sim 10^{14}$ G) currently estimated to exist in the galaxy (at least $\sim$10% of all NSs; Kulkarni & Frail, 1993; Kouveliotou et al., 1994; Ibrahim et al., 2004). Thompson & Duncan (1993) have proposed a dynamo mechanism in order to enhance the magnetic field of newly-born NSs. In this model, the field is enhanced by the combined effects of differential rotation (which wraps the star's poloidal field around the star, stretches the field and serves as a source of the large-scale toroidal field) and convection (which twists the toroidal field lines and replenishes the poloidal field).

There is also the question of how large a field can be sustained before the star becomes unstable. An estimate can be made by equating the gravitational binding energy of the star ($\sim 3GM^2/5R$) with the magnetic field energy ($\sim [B^2/8\pi][4\pi R^3/3]$). This results in what is called the virial limit:

$$B \sim 1.4 \times 10^{18} \left(\frac{M}{1.4\ M_\odot}\right) \left(\frac{R}{10\ \text{km}}\right)^2 \text{ G}, \tag{1.6}$$

where M and R are the mass and radius of the NS, respectively. Studies of the structural stability of stars when a large magnetic field is introduced have yielded maximum fields at the center of the star of $\sim 3{\times}10^{18}$ (Cardall et al., 2001).

We can also estimate how a large field affects the EOS by looking at how it interacts with individual particles (Lattimer & Prakash, 2007). First, a strong magnetic field quantizes the orbital motion of charged particles around it (called Landau quantization). Relativistic and quantum effects become important when the particle's cyclotron energy ($e\hbar B/mc$) is comparable to its rest-mass energy (mc^2). For electrons and protons, the resulting fields are

$$B^e_{qed} = 4.414 \times 10^{13} \text{ G}, \quad B^p_{qed} = (m_p/m_e)^2 B^e_{qed} = 1.487 \times 10^{20} \text{ G}. \tag{1.7}$$

B^e_{qed} is commonly referred to as the *quantum critical field*. If the internal field of NSs can reach values as high as 10^{18} G, Landau quantization of the electron energies can decrease the rate of electron capture and soften the EOS. However, additional effects (e.g., increased energy contributions from the anomalous magnetic moments of the neutrons and protons) can counteract this softening. Therefore, fields as large as the upper limit mentioned above are not *currently* expected to have a significant effect on the EOS (Lattimer & Prakash, 2007). On the other hand, the compositional changes that result from these fields can affect the cooling history of the star by enhancing the direct Urca process (see below). In addition, fields larger than $\approx 4.4 \times 10^{13}$ G are expected to affect the low density regions of the star significantly (i.e., the outer layers from which the observed emission is radiated away).

1.4.3 Neutron Star Cooling Emission

As NSs are born from explosive events, they are expected to have a hot interior from their birth. Neutrinos are thought to become momentarily trapped during collapse and their sudden release in the first few seconds of the star's life is thought to heat the core to temperatures of $T_c \sim 10^{11-12}$ K. However, the continuous escape of neutrinos causes the core to cool rapidly ($T_c \sim 10^9$ K), while the crust remains warm. In the first 10–100 yrs of its life, the interior of the star eventually becomes isothermal as heat is transported inward to the core. As the temperature of the interior continues to decrease due to neutrino emission ($T_c \sim 10^{8-9}$ K), the temperature of

the outer layer (referred to as the *envelope* and the source of the observed emission from the star) is a factor of $\sim$100 lower than that of the interior. The envelope follows the thermal evolution of the core, which continues to cool by neutrino emission processes until the star is $\sim 10^5$ yrs old. After such time, neutrino emission stops and the star loses its residual heat through photon emission by the envelope. For most of this thermal evolution (see, e.g., Lattimer & Prakash, 2004, and references therein), the temperature of the star is high enough to be observed in the X-ray range of the electromagnetic spectrum.

Thermal Evolution

Cooling models depend on the EOS of dense matter (including the properties of the superfluid components), the NS mass and the envelope composition (see Page et al., 2006, for a recent review). As such, comparing the predicted values of temperature vs. age, or luminosity vs. age, provides insights into the internal properties of NSs and the physics associated with them. First, the equations of hydrostatic equilibrium for a specific EOS are numerically solved to obtain the NS structure. The thermal evolution is then followed by solving the equations of energy transport assuming an isothermal interior:

$$C_V(T)\frac{dT}{dt} = -L_\nu(T) - L_\gamma(T_e), \quad C_V(T) = CT, \quad L_\nu(T) = QT^\delta, \quad L_\gamma(T_e) \equiv 4\pi R^2 \sigma_{SB} T_e^4, \tag{1.8}$$

where C_V is the total specific heat, T is the internal temperature, L_ν is the neutrino luminosity, Q is the neutrino emissivity, δ is the temperature dependence of the neutrino emission process, R is the radius of the star, σ_{SB} is the Stephan-Boltzmann constant and T_e is the effective surface temperature of the star. In addition, relating the internal temperature T to the effective temperature T_e requires independent modeling of the stellar envelope, although in general it is expected that $T_e \propto T^{1/2}$ (Page et al., 2006, and references therein). The cooling history of neutron stars is commonly divided into the neutrino cooling era ($L_\nu \gg L_\alpha$, ages $\lesssim 10^5$ yrs old) and

the photon cooling era ($L_\nu \ll L_\alpha$, ages $>10^5$ yrs old). Cooling curves that track the thermal evolution of the star as it ages are shown in Figure 1.4.

Historically, the mechanisms responsible for cooling through neutrino emission have been divided into "standard" and "enhanced" processes. Standard cooling refers to slow processes involving modified Urca (mUrca, e.g., $n + n' \rightarrow p + n' + e^- + \bar{\nu}_e$) and nucleon bremsstrahlung (e.g., $n + n' \rightarrow n + n' + \nu_e + \bar{\nu}_e$). Enhanced cooling refers to rates with highly increased neutrino emissivities due to direct Urca processes (dUrca) involving nucleons, hyperons, meson condensates, strange quark matter or a mixture of these phases (e.g., $n \rightarrow p + e^- + \bar{\nu}_e$). The onset of dUrca requires charge fractions $\geq 1/9$ (in the absence of muons or hyperons), which sets a restriction on the density needed for this process to be present. In addition, the strong interaction is thought to allow nucleons (n and p) to produce Cooper pairs at temperatures below a critical value $T_c(\rho)$ that is a function of density and allows for superfluid components to arise. The formation and breaking of these pairs (PBF) decreases the efficiency of the mUrca and bremsstrahlung processes and is thought to dominate the neutrino cooling efficiencies at temperatures $\lesssim T_c(\rho)$. However, PBF is expected to have higher emissivities than the standard cooling processes and when taken into account the star cools at a faster rate.

In the photon cooling era, neutrino emission becomes inefficient and the evolution of the star is dominated by the loss of thermal energy in the form of photon emission from the envelope. As such, the evolution is highly dependent on the nature of the envelope.

For a given EOS of dense matter, a variety of NSs with different masses, radii and central densities can be constructed. In general, stars with low masses would have slow-cooling cores, while stars with high masses have fast-cooling cores. The composition of the envelope also has a large effect on the cooling rate. If light elements are present, the increased thermal conductivity produces higher temperatures at the surface of the star and increases the cooling rate. On the other hand, heavy elements lower the temperature and slow down the cooling rate. The presence of a high magnetic field in the envelope is thought to have a smaller effect than the chemical

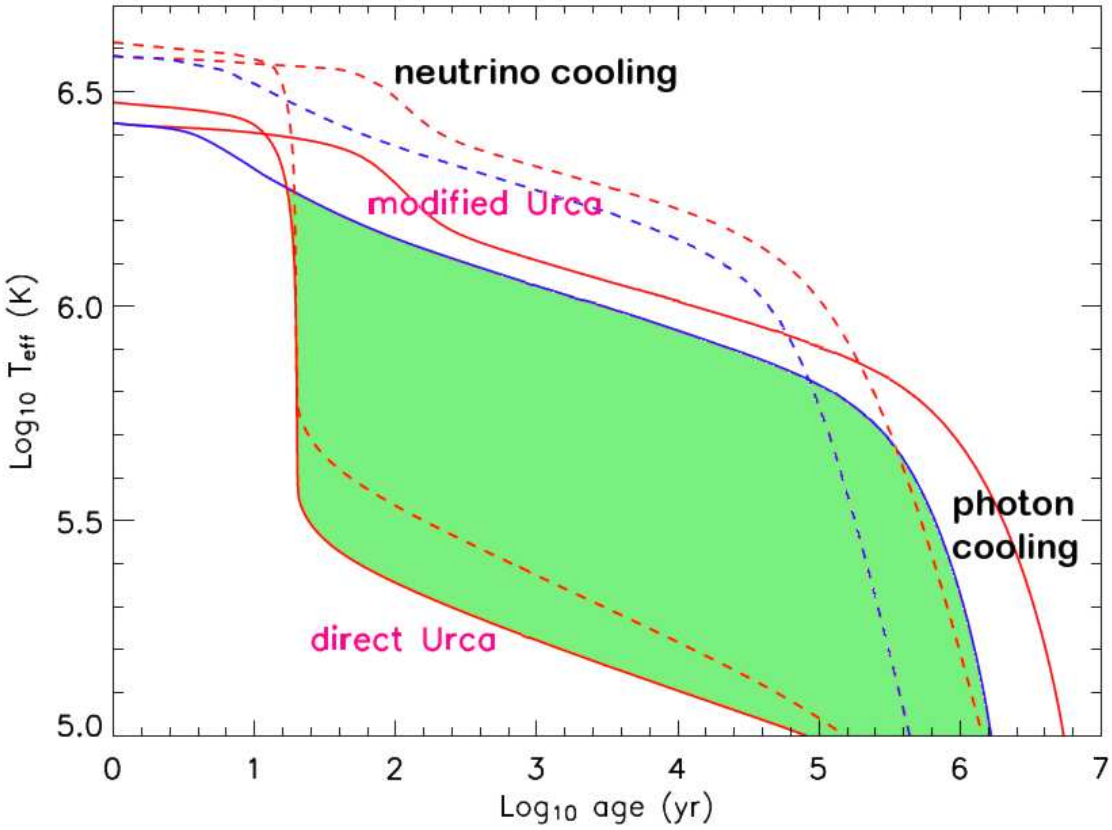

Figure 1.4: Sample cooling curves for neutron stars. The upper four curves include cooling through mUrca only, while the bottom two include only dUrca. Blue lines include the effects of superfluidity and subsequent enhanced cooling through PBF while red lines do not. Dashed curves assume an envelope composed of H, while solid curves have an Fe envelope. The shaded green region represents the allowed parameter space for various dUrca models with the effects of PBF. Adapted from Figure 4 of Lattimer & Prakash (2004).

composition (unless the field is confined to the crust). In addition, the composition and magnetic field will both have a large effect on the spectrum of the emergent radiation.

Emergent Radiation

The thermal emission observed from NSs can be very different from a blackbody and its angular distribution on the surface can be anisotropic depending mainly on the composition of the atmosphere and its magnetic field (see, e.g., Zavlin & Pavlov, 2002; Yakovlev et al., 2004; van Adelsberg & Lai, 2006). The atmospheres of NSs are very thin ($\sim$a few cm) and very dense (up to $\sim 10^4$ g cm^{-3}). These outer layers can be gaseous or condensed depending on the temperature, composition and magnetic field (e.g., Hydrogen is expected to transition into a condensed phase for temperatures $\leq 10^6$ K and magnetic fields $>5\times 10^{14}$ G). A high magnetic field strongly affects the distribution of surface emission as the radiative opacities are proportional to the magnetic field and the direction and polarization of the radiation. In addition, a strong field changes the heat conductivity such that it is largest along the magnetic field lines, greatly affecting the emission distribution. The structure of atoms also becomes very distorted in these conditions, changing the binding (ionization) energy of these atoms and affecting the ionization equilibrium conditions of the atmosphere.

Modeling of NS atmospheres requires solving the equations for radiative transfer, radiative equilibrium and hydrostatic equilibrium by assuming a plane-parallel atmosphere and local thermodynamic equilibrium (see, e.g., Zavlin & Pavlov, 2002):

$$\mu \frac{d}{dy} I_\nu = \kappa_\nu (I_\nu - S_\nu), \quad \int_0^\infty d\nu \int_{-1}^{1} \mu I_\nu d\mu = \sigma_{SB} T_e^4, \quad P = gy, \tag{1.9}$$

where

$$\mu = \cos\theta, \ dy = \rho dz, \ \kappa_\nu = \alpha_\nu + \sigma_\nu, \ S_\nu = (\sigma_\nu J_\nu + \alpha_\nu B_\nu)\kappa_\nu^{-1}, \ J_\nu = \frac{1}{2}\int_{-1}^{1} I_\nu d\mu, \tag{1.10}$$

and where θ is the angle between the normal to the atmosphere and the wave vector of the outgoing radiation, y is the column density (with z being the geometrical

depth), κ_ν is the total radiative opacity at a specific frequency ν (with α_ν being the "true absorption" and σ_ν the scattering opacity), S_ν is the source function, J_ν the mean spectral intensity, B_ν the Planck function and P is the atmospheric pressure (where the radiative force is not expected to contribute significantly to the pressure for temperatures $< 10^7$ K). In addition, the ionization states of the plasma have to be taken into account in order to derive the electron number density in the atmosphere and the fraction of ions in different ionization states (important for the radiative opacities contributed by free-free, free-bound and bound-bound transitions). Finally, the emission detected by a distant observer must be integrated over the visible part of the NS surface and gravitational redshift and photon-bending must be taken into account (e.g., the redshifted temperature observed at infinity is $T_e^\infty = T_e[1 - 2GM/Rc^2]^{1/2}$).

If the atmosphere contains light elements (H, He) it is expected that the fast decrease of opacities with energy ($\sim E^{-3}$, mainly due to free-free transitions) will allow for the high-energy radiation to arise from deeper, hotter layers of the atmosphere. These models then show a high-energy tail that deviates from the blackbody case. In addition, since the opacities are large at low energies, the low-energy photons escape from higher depths with temperatures $< T_e$ and low-energy tails are suppressed. Therefore, fitting such emission with a blackbody model will give higher temperatures than present on the star. Spectral fits to X-ray data have found blackbody temperatures higher by a factor of $\sim$2–3, while atmospheric models also give larger emitting areas by factors of $\sim$50–200. If the atmosphere contains heavy elements, the opacities have a flatter energy dependence and the emergent spectra will be closer to a blackbody. However, many spectral lines and absorption edges can be present. Figure 1.5 (left) shows simulated spectra for different compositions and temperatures.

Even in the absence of a high magnetic field, the emergent emission from an atmosphere can be highly anisotropic due to limb-darkening, where at large θ the emerging photons are produced in shallow layers with lower temperature. In the presence of a large magnetic field, the emission will be highly polarized and radiative opacities depend on the polarization and direction of the radiation (see, e.g., van Adelsberg & Lai, 2006). Atmospheres with high magnetic fields are then found to

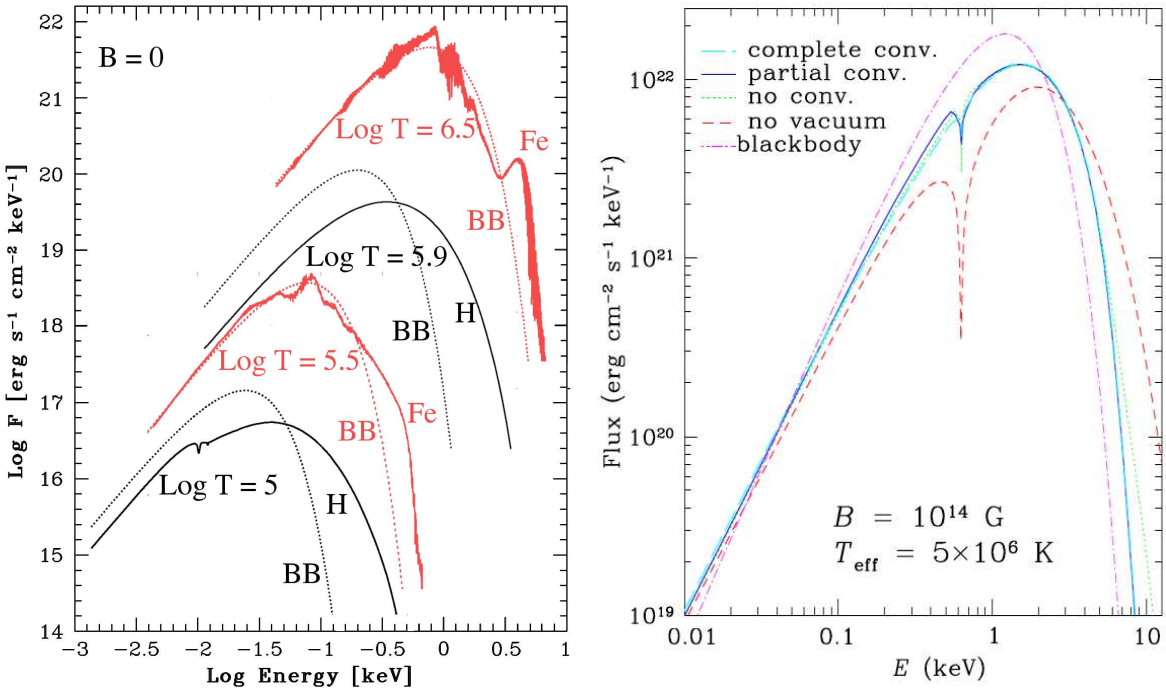

Figure 1.5: Sample emergent spectra from the atmosphere of a NS at various temperatures, compositions and magnetic fields. *Left*: H (*black*) and Fe (*red*) atmospheres at different temperatures and zero magnetic field. Dashed lines show the corresponding blackbody spectrum. The effect of a light element atmosphere is clearly visible: a high energy tail is produced and at low temperatures weak spectral features are present. Heavy elements result in a large number of spectral features and shape closer to a blackbody. This figure was produced using data by Pavlov et al. publically available at http://www.ioffe.rssi.ru/astro/Stars/. *Right*: Spectra of a fully ionized H atmosphere in the presence of a large magnetic field. A large proton cyclotron line and hard-energy tail are visible when vacuum polarization is not taken into account, which together with mode conversion results in softer spectra (though still harder than a blackbody) and less significant spectral features. Adapted from van Adelsberg & Lai (2006).

have harder spectra compared to a blackbody with the same T_e, though not as hard as for light element atmospheres alone (opacity dependence on energy is flatter, $\sim E^{-1}$). At $T_e < 10^6$ K, the photo-ionization opacity in a H atmosphere is important and the spectral shape is very sensitive to the magnetic field value. At high enough T_e to provide strong ionization, the spectrum may have strong spectral features from proton or electron cyclotron lines with energies of $E_{cp} \approx 6.3\ (B/10^{12}\ \mathrm{G})$ eV and $E_{ce} \approx 11.6\ (B/10^{12}\ \mathrm{G})$ keV, respectively.

For large enough fields ($B \gtrsim 7 \times 10^{13}$ G), it is estimated that the QED effects of vacuum polarization and mode conversion will significantly affect the emergent radiation by softening the spectrum and reducing the width of any spectral features (see, e.g., van Adelsberg & Lai, 2006, and references therein). In high magnetic fields, as photons propagate they have two polarization modes (parallel $-$ O $-$ and perpendicular $-$ X $-$ to the plane that the magnetic field makes with the direction of propagation), with one of them (X) having a much smaller opacity and therefore carrying the bulk of the thermal energy. For fields larger than B^e_{qed}, the vacuum itself is polarized due to presence of virtual e^-/e^+ pairs, changing the dielectric properties of the medium. In addition, vacuum polarization allows for a photon to change its polarization (an effect called "mode conversion") which, when combined with propagation effects through the medium, can significantly affect the observed spectrum (X photons from deep in the atmosphere are changed to O photons and suppressed, while O photons are changed to X photon at lower densities and thus lower temperatures; van Adelsberg & Lai, 2006). Figure 1.5 (right) shows the effects of vacuum polarization in the spectra of NSs with high magnetic fields.

Therefore, while the surface emission from NSs provides important clues to the physics of the interior, we also need to account for the important effects of the atmosphere and magnetic field on the emergent radiation.

1.4.4 Magnetospheric Emission

Rotating NSs are known to produce active magnetospheres where charged particles are accelerated, electron-positron pairs are produced and a bulk outflow of magnetized plasma leaves the system. The energy flow out of the magnetosphere is thought to be the main driving force behind the slow-down with time that is observed in rotation-powered pulsars. The central theme of pulsar magnetosphere research is to determine the global structure of the magnetosphere: how currents are generated, how they flow and how they close.

Structure of the Magnetosphere

The rotating magnetosphere is thought to extract charged particles from the surface of the star (Goldreich & Julian, 1969). Treating the star as a perfectly conducting sphere in a magnetic field, the rotation separates charges inside the conductor due to the Lorentz force ($\mathbf{F} = \mathbf{E} + q(\mathbf{v} \times \mathbf{B})$) and induces an electric field on the surface (Eq. 1.2). This electric field outside the conductor develops an accelerating component ($E_{||} = \mathbf{E} \cdot \mathbf{B}/|\mathbf{B}|$) responsible for the extraction of particles from the surface that populate the magnetosphere with an estimated charge density of (Goldreich & Julian, 1969):

$$\rho_{GJ} = \frac{1}{4\pi} \nabla \cdot \mathbf{E} = -\frac{1}{4\pi c} \nabla \cdot ((\mathbf{\Omega} \times \mathbf{r}) \times \mathbf{B}) = -\frac{\mathbf{\Omega} \cdot \mathbf{B}}{2\pi c}, \tag{1.11}$$

where the last identity was found using $\nabla \cdot ((\mathbf{\Omega} \times \mathbf{r}) \times \mathbf{B}) = \mathbf{B} \cdot (\nabla \times (\mathbf{\Omega} \times \mathbf{r})) - (\mathbf{\Omega} \times \mathbf{r}) \cdot (\nabla \times \mathbf{B})$, with $\nabla \times (\mathbf{\Omega} \times \mathbf{r}) = 2\Omega\hat{z} = 2\mathbf{\Omega}$ and for a dipolar magnetic field $\nabla \times \mathbf{B} = 0$. The induced $\mathbf{E}$ from a dipolar magnetic field has a quadrupolar form. As particles populate the magnetosphere, charges of one sign are extracted from the poles while opposite charges are extracted from the equator. These electric "gaps" are expected in the magnetosphere, in regions where $\mathbf{E} \cdot \mathbf{B} \neq 0$, which cause particles to accelerate. The magnetic field lines and particles corotate with the star out to a distance $R_{LC} = c/\Omega$ where their velocities would exceed the speed of light. This radius defines the boundary of the light cylinder, outside which the dipolar magnetic field lines open and allow particles to escape. These particles can in turn induce a

toroidal magnetic component. However, once particles populate the magnetosphere, the quadrupolar space charge they create would tend to cancel the accelerating electric field, reducing the surface charge, turning off the particle injection and approaching a quasi-steady state.

The problem of solving for a steady-state magnetosphere using a physically meaningful representation has been approached in the context of force-free electrodynamics (FFE, see, e.g., Komissarov, 2002; Spitkovsky, 2004). Here, instead of solving magneto-hydrodynamic (MHD) equations for plasma in strong fields, the dynamics of the field in the presence of conducting plasma are solved. In this case, the electromagnetic field is so strong that the inertia and pressure of the plasma itself can be ignored. In this "force-free" case, the balance of forces on the plasma is given by $\rho\mathbf{E} + \frac{1}{c}\mathbf{J} \times \mathbf{B} = 0$, where $\mathbf{J}$ is the plasma current density. This equation can be rewritten in terms of a nonlinear, second-order differential equation, known as the "pulsar equation" (Michel, 1973; Sieber & Wielebinski, 1973). Exact solutions to this equation are only possible for simplified cases and it was only recently that a numerical solution was obtained for the case of a rotating magnetic dipole where the magnetic and rotating axes are aligned (Contopoulos et al., 1999).

In the case of aligned magnetic and rotation axes, the magnetosphere shows the configuration that is expected from the idealized rotating dipole: a corotating closed zone extending to the light cylinder and an open wind zone with asymptotically monopolar field lines. Current flows along the open field lines to infinity, and the bulk of the return currents flow in an equatorial current sheet and on the boundary between open and closed field lines. There is also a current flowing between the magnetic axis and the edge of the open field line region, thought to be responsible for the spin-down torque (Contopoulos et al., 1999; Contopoulos & Spitkovsky, 2006). The energy that is lost by the star is found to be consistent with the idealised rotating dipole in vacuum:

$$\dot{E} = \frac{c}{4\pi} \int \mathbf{E} \times \mathbf{B} d\mathbf{s} \sim \frac{\mu^2 \Omega^4}{c^3}, \tag{1.12}$$

where in this case μ is the magnetic dipole moment. The fact that we observe pulsations from NSs implies that their magnetic and rotation axes are not aligned. For an angle between these axes of α, the energy loss has been traditionally estimated using $\dot{E}_{inc} = \dot{E} \sin^2 \alpha$, with *inc* denoting the inclined value. However, numerical solutions to an inclined pulsar magnetosphere (Spitkovsky, 2006) suggest an energy loss of $\dot{E}_{inc} = \dot{E}\ (1 + \sin^2 \alpha)$. The estimates of NS surface magnetic fields derived from the aligned dipole case are similarly affected, resulting in values of $B_{inc} = B\ (1 + \sin^2 \alpha)^{-1/2}$. Therefore, it should be kept in mind that deviations from an aligned rotator could produce energy losses and magnetic fields higher by up to a factor of $\sim$2 and lower by up to a factor of $\sim$1.7, respectively, than those estimated from the aligned, vacuum case.

Emission Regions and High-Energy Mechanisms

The magnetospheres of rotation-powered pulsars are thought to be filled with ultra-relativistic electron-positron pairs that can emit radiation up to, at least, TeV energies. The accelerating potential drop is estimated to be $\Phi \simeq \Omega^2 B R^3/2c \sim 10^{12} B_{12} P^{-2}$ eV (e.g. Harding & Lai, 2006), where B_{12} is the surface magnetic field in units of 10^{12} G and P is the period in seconds. The radio emission from pulsars is believed to require coherent emission processes involving electron-positron pairs, while the emission at higher energies is thought to arise from incoherent processes involving highly accelerated particles. Two regions have been proposed to be the accelerating sites: the polar cap regions just above the magnetic poles and the outer regions of the magnetosphere along the last open field lines. However, the emission geometries of both models have changed significantly, leading to the development of "slot" gap regions (see, e.g., Harding, 2005, and Figure 1.6).

In polar cap models, particle acceleration takes place along open field lines close to the magnetic poles, where the magnetic field is higher (Harding & Muslimov, 2001a, 2002). The size of these regions is estimated to be $r_{pc} = R\theta_{pc} \simeq R(R/r_{lc})^{1/2} = (2\pi R^3/cP)^{1/2}$. Pulsars with high surface fields can accelerate particles to high energies (Lorentz factors of $\sim 10^7$) and emit γ-ray curvature radiation (CR) as the particles

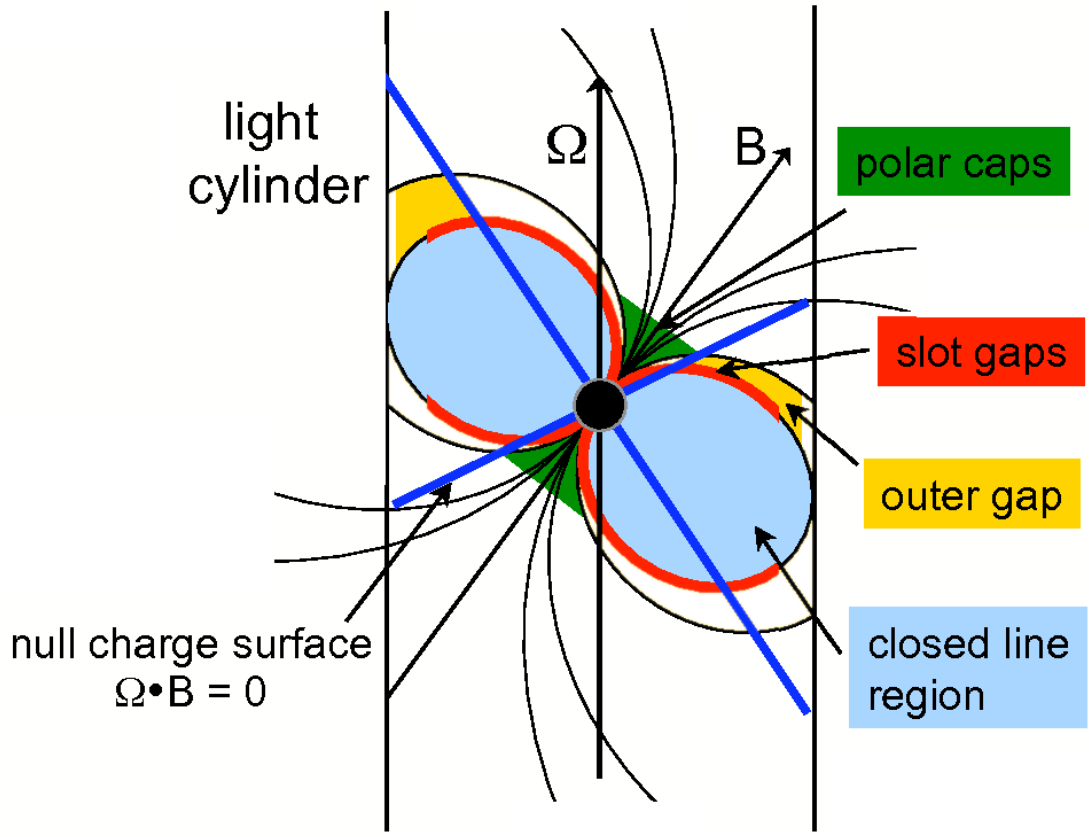

Figure 1.6: Expected emission regions in the magnetospheres of pulsars as predicted by the polar cap, outer gap and slot-gap models. Image produced following the geometries shown in Figures 1 and 2 from Harding et al. (2007).

follow the curvature of the magnetic field lines. These γ-rays are energetic enough to produce electron-positron pair cascades ($\gamma \rightarrow e^- + e^+$) and further radiation. Pulsars with lower surface fields accelerate particles to lower energies ($\gamma \sim 10^{4-6}$) which are thought to produce γ-ray photons through inverse-Compton scattering (ICS) of lower-energy thermal X-ray photons from the surface. Other pulsars with lower magnetic fields are thought to produce pairs through the interaction of low-energy γ-rays from the accelerated particles with X-ray photons from the surface ($\gamma + \gamma \rightarrow e^- + e^+$).

Slot-gap models invoke acceleration in narrow regions close to the last open field line where the potential is lower and larger distances are needed to accelerate particles to high enough Lorentz factors to produce further pairs (Muslimov & Harding, 2004). Pair formation cascades then do not happen close to the surface of the star but in a narrow slot bordered by the last open field line. Outer gap models (Cheng et al., 1986) involve acceleration in a vacuum gap in the outer magnetosphere along the last open field line and above the "null charge surface" (the surfaces given by $\mathbf{E} \cdot \mathbf{B} = 0$ where the charge density changes sign and thus borders the quadrupole charge distribution). Here, high-energy radiation results from pair cascades produced from the interaction of two photons, as above.

The emission at optical, infrared and X-ray energies has been proposed to arise due to synchrotron emission of charged particles accelerated to Lorentz factors of $\sim 10^{2-5}$ (e.g., Crusius-Wätzel et al., 2001; O'Connor et al., 2005).

1.5 Rotation-Powered Pulsars

Rotating NSs whose spin periods (P) are observed to increase with time are thought to lose rotation kinetic energy due to magnetic dipole braking. The rate at which the star loses energy as it slows down can be found by taking a time derivative of the available rotational kinetic energy ($E = \frac{1}{2} I \Omega^2 = 2\pi^2 I P^{-2}$), which gives:

$$\dot{E} = I \Omega \dot{\Omega} = -4\pi^2 I \frac{\dot{P}}{P^3}, \tag{1.13}$$

where I is the star's moment of inertia and $\dot{P}$ is the rate at which the period increases with time. The quantity $\dot{E}$ is referred to as the "spin-down luminosity" of the star. In general, this slow-down is thought to arise from the loss of energy in the form of magnetic dipole radiation. The power radiated by a rotating magnetic dipole is given by:

$$\dot{E} = -\frac{2}{3c^3}|\ddot{\boldsymbol{\mu}}|^2 = -\frac{2\mu^2 \sin^2\alpha}{3c^3}(\dot{\phi}^4 + \ddot{\phi}^2) \sim -\frac{2B^2R^6 \sin^2\alpha\Omega^4}{3c^3}, \tag{1.14}$$

where the dipole magnetic moment is given by $\boldsymbol{\mu} = \mu(\sin\alpha\sin\phi\hat{\mathbf{i}} + \sin\alpha\cos\phi\hat{\mathbf{j}} + \cos\alpha\hat{\mathbf{k}})$, for a dipole moment $\mu = BR^3$, α is the (fixed) angle between the rotation and magnetic axes, and we have used the fact that $\dot{\phi} = \Omega$ and $\dot{\Omega}^2 \ll \Omega^4$. Making the assumption that all of the observed pulsar's spin-down luminosity arises due to the magnetic dipole radiation, setting Equations 1.13 and 1.14 equal to each other results in an expression for the star's surface magnetic field strength of

$$B = \sqrt{\left(\frac{3Ic^3}{8\pi^2R^6\sin^2\alpha}\right)(P\dot{P})}. \tag{1.15}$$

Furthermore, assuming aligned rotation and magnetic axes ($\sin\alpha = 1$), a uniform sphere with moment of inertia $I = 2MR^2/5$, a mass $M = 1.4\ M_\odot$ and radius $R = 10$ km we find the following expression for the spin-down luminosity and magnetic field strength:

$$|\dot{E}| = 3.9 \times 10^{32}(P^{-3}\dot{P})\ \text{ergs s}^{-1}, \quad B = 3.2 \times 10^{19}(P\dot{P})^{1/2}\ \text{G}, \tag{1.16}$$

where P is in seconds and $\dot{P}$ is in units of 10^{-14} s s^{-1}. In addition to magnetic dipole braking, the large number of particles extracted from the surface of the star and accelerated in the magnetosphere is expected to create an additional amount of torque that contributes to the slow-down. This theory has been supported by observations of the radio pulsar PSR B1931+24 (Kramer et al., 2006), which shows a larger spin-down rate when it is observed as an active emitter of radio waves (for about 5–10 days) than when it "turns off" (for about 25–35 days) intermittently.

We can also make an estimate of the age of the star by making the assumption that it slows down at a rate proportional to the rotation frequency raised to some power n in the form

$$\dot{\Omega} = K\Omega^n, \tag{1.17}$$

where K is a constant of proportionality and n is called the 'braking index'. Taking the derivative with respect to time of Equation 1.17 results in the expression $n = \Omega\ddot{\Omega}/\dot{\Omega}^2$, allowing for n to be a measurable quantity once Ω and its first and second time derivatives are also measured. Integrating Equation 1.17 out to a present time τ results in the following

$$\begin{aligned} \int_{\Omega_0}^{\Omega} \frac{d\Omega}{\Omega^n} &= -K \int_0^{\tau} dt \\ \tau &= -\frac{1}{(n-1)} \frac{\Omega}{\dot{\Omega}} \left[1 - \left(\frac{\Omega}{\Omega_0} \right)^{(n-1)} \right] \end{aligned} \tag{1.18}$$

where Equation 1.17 was substituted into an intermediate expression to arrive at Equation 1.18. Comparing the intermediate expression in Equation 1.13 and the last expression in Equation 1.14 with Equation 1.17, we see that the case of a star spinning down solely due to magnetic dipole braking gives $n = 3$ and $K = 2B^2R^6 \sin^2 \alpha / 3Ic^3$. In this case, and further assuming that the star's initial spin frequency was much greater than its current spin frequency ($\Omega_o \gg \Omega$), we also obtain

$$\tau_c = -\frac{\Omega}{2\dot{\Omega}} = \frac{P}{2\dot{P}} \text{ s}, \tag{1.19}$$

where τ_c is referred to as the star's characteristic age.

The measured period and period derivatives of known pulsars then allow us to estimate key physical parameters for these objects using Equations 1.16 and 1.19. However, it should be kept in mind that many assumptions have gone into arriving at these expressions and these results should be taken as general estimates for the stars' properties and allow for overall comparisons between different objects. Figure 1.7 shows the parameter space of known pulsars and their inferred physical properties. In general, pulsars with small periods and large period derivatives are estimated to

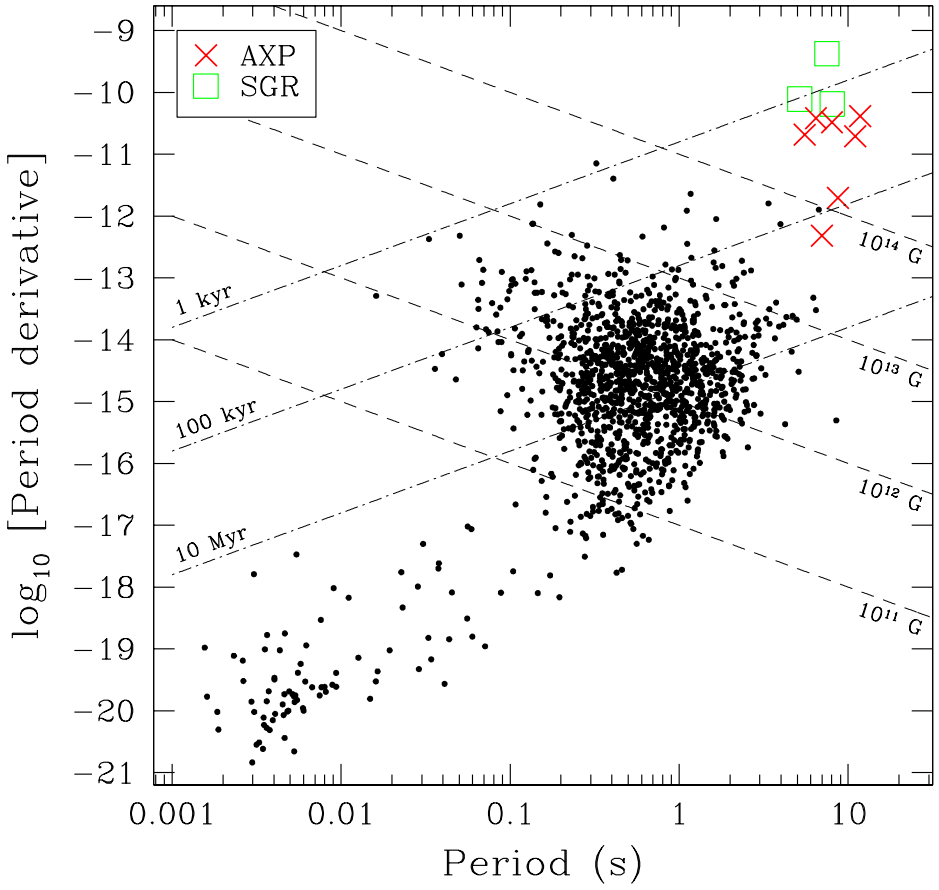

Figure 1.7: Period−period derivative diagram of known pulsars to date. Dashed and dash-dotted lines show the lines of constant magnetic field and constant characteristic ages, respectively. Radio pulsars are shown as black dots, while magnetars are shown by squares and crosses as labelled. High-energy X-ray and γ-ray pulsars in general occupy the area denoted by young, fast-spinning sources with high magnetic fields (the top, left corner). Magnetars in turn represent the extreme of the population having the largest magnetic fields, longest periods and young ages. A total of 1,700 pulsars are included. Data points were obtained from the online pulsar catalogue of the Australia Telescope National Facility (Manchester et al., 2005, available at http://www.atnf.csiro.au/research/pulsar/psrcat). Figure provided by C. Tam.

be young and have a large amount of rotational energy. In order of increasing age and decreasing rotational energy, the youngest and most energetic pulsars are known as Crab-like ($\tau_c \lesssim 5\times10^3$ yrs, $\dot{E}\sim10^{37-38}$ ergs s^{-1}), Vela-like ($\tau_c\sim10^{3-4}$ yrs, $\dot{E}\sim10^{36-37}$ ergs s^{-1}) and Geminga-like ($\tau_c\sim10^5$ yrs, $\dot{E}\sim10^{35-36}$ ergs s^{-1}). These pulsars occupy the top, left region of Figure 1.7 and represent $\approx$5% of the known population. The large amount of spin-down energy available in these sources is believed to make them efficient high-energy emitters and some have been observed up to TeV energies. While most of their observed emission is believed to arise from accelerated particles in the magnetosphere, the youngest NSs are also observed to have thermal X-ray emission from the surface that are believed to be powered by cooling radiation and/or hot-spots heated by back-flowing particles from the magnetosphere. Many of them are also seen to power extended nebulae around them (see §1.6). The top, right of Figure 1.7 is occupied by slower pulsars with lower spin-down luminosities. At the highest estimated magnetic fields we find the so-called "magnetars" ($B\sim10^{14-15}$ G, see §1.7) with high-magnetic field radio pulsars having slightly smaller inferred fields ($B\sim10^{13-14}$ G).

1.6 Pulsar Wind Nebulae

A significant fraction of the spin-down power of NSs is believed to escape from the star as a relativistic wind of particles and magnetic fields. When this wind is confined by the surrounding medium, an observable "pulsar wind nebula" (PWN) is produced (see, e.g., Gaensler & Slane, 2006; Bucciantini, 2007, for recent reviews). These sources have been observed from radio to γ-ray energies and represent some of the most efficient particle accelerators known. Young pulsars are expected to reside inside the supernova remnants (SNRs) created during their birth, while older pulsars with high velocities are expected to have abandoned their birth sites and travel through the interstellar medium (ISM) with typical velocities of $\sim$400–500 km s^{-1} and values as high as $\sim$1,000 km s^{-1}.

The wind from the star is believed to be accelerated to ultra-relativistic speeds until it is confined by the pressure from its surroundings and slowed down at a termination shock (TS). The bulk of the observed radiation from the nebula is emitted beyond the TS once the particles are slowed down to velocities $\sim 0.3 - 0.5c$ and emit synchrotron radiation. The nebula then extends to an outer boundary delimited by the location of the SNR shell or ISM (see Fig. 1.8) The best studied PWN is that associated with the Crab pulsar, where a large-scale torus and jet structure is clearly visible (Weisskopf et al., 2004). Some pulsars show a more cometary morphology, where the PWN is believed to be confined by the ram pressure of a fast-moving pulsar (Gaensler et al., 2004). A total of $\sim$50 PWNe are currently known.

The pulsar wind, driven by the spin-down energy, is terminated at a TS shock radius where the ram pressure of the wind is balanced by the pressure of its surroundings

$$R_{TS} = \sqrt{\frac{\dot{E}}{4\pi c f P_s}}, \tag{1.20}$$

here f is the filling factor of the wind (scaled to the isotropic case) and P_s is the pressure of the surroundings. In the case of a wind confined by the pressure of the surrounding large-scale nebula, and assuming equipartition between particles and magnetic fields, then $P_s = B_n^2/4\pi$, where B_n is the mean nebular magnetic field. In the case of a wind confined by the ram pressure of a fast-moving pulsar, then $P_s = \rho V_{psr}^2$, where ρ is the density of the medium through which the pulsar is traveling (for young pulsars this could be ejecta from the SNR, for older pulsars the ISM) and V_{psr} is the pulsar's space velocity.

The presence of asymmetric morphologies in PWNe support the view that the outflowing wind for the star is highly anisotropic, with most of the energy being transported out through the equatorial belt (corresponding to the observed tori). The presence of jets indicate that collimation occurs at high latitudes close to the poles. The morphology of these nebulae can then be used to estimate the orientation of the stars' rotation and magnetic axes in space (and in the case of fast-moving pulsars their proper motion direction). In addition, the morphology of PWNe is seen

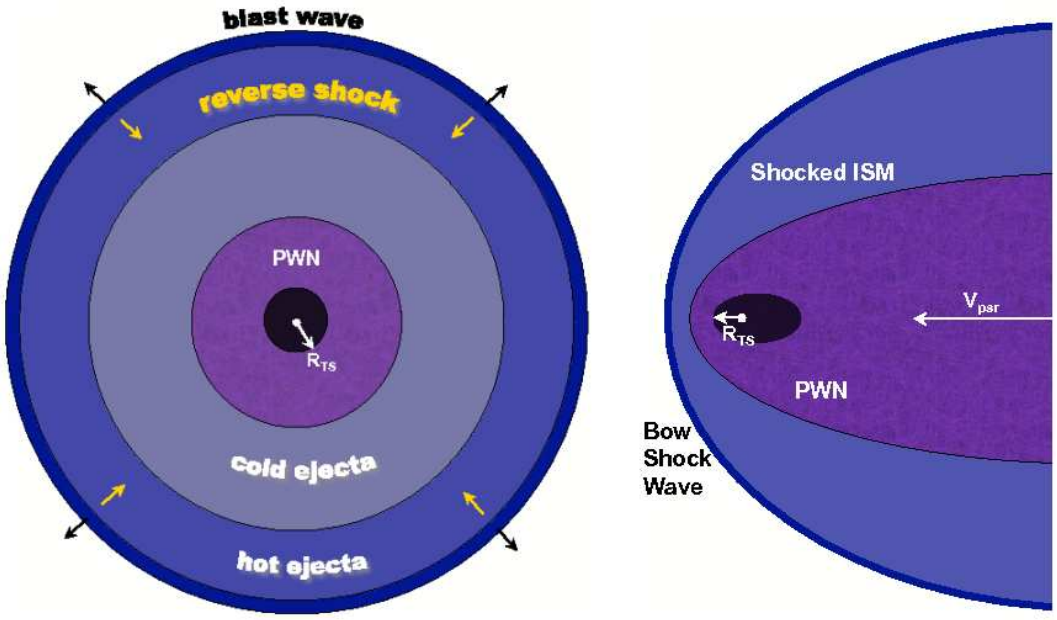

Figure 1.8: Schematics of the confinement of a PWN. *Left*: The nebula resides inside the cavity created by the expanding ejecta of a supernova remnant. The pulsar wind is decelerated at a termination shock where it encounters slowing-moving matter from the larger (static) PWN. *Right*: The nebula resides inside the cavity created by the large velocity of the pulsar. In this case, the termination shock and large nebula are both extended in the direction of the pulsar's velocity. Note: the relative sizes of the different PWN components are not to scale; R_{TS} is estimated to be much smaller than the radius of the extended nebula.

to vary with photon energy, on average being larger at larger frequencies. This effect is thought to arise from the lower synchrotron lifetimes of more energetic electrons in a given magnetic field (see §1.8). In this case, the high energy X-ray emission is thought to trace the recent history of particle injection in the nebulae, while the emission at lower energies traces the long-term evolution of the system.

The X-ray spectra of PWNe are found to be non-thermal and can be well described by a power law with photon indices $\Gamma \sim 1.5 - 2.5$ ($S_E \propto E^{-\Gamma}$). At radio and optical wavelengths, the emission has spectral index $\alpha \sim 0 - 0.3$ and $\alpha \sim 0.7$, respectively ($S_\nu \propto \nu^{-\alpha}$, $\alpha \equiv \Gamma - 1$). Therefore, one or more spectral breaks are needed to model the broad-band emission from PWNe, indicating that multiple accelerating mechanisms (or emitting particle populations) are present.

1.7 Magnetars

The class of NSs that are now identified as "magnetars" is made up of two groups of objects, known as Soft Gamma Repeaters (SGRs) and Anomalous X-ray Pulsars (AXPs; see Woods & Thompson, 2006; Kaspi, 2007, for recent reviews). Currently, the number of known (unconfirmed) magnetars is 4(1) SGRs and 8(2) AXPs. SGRs exhibit bursts of γ-ray emission with average energies of 10^{40-41} erg that repeat on a timescale of years. Three of them have been shown to have rare giant superflares with total released energies of 10^{45-47} erg. AXPs were discovered as persistent X-ray sources where the observed pulsations imply spin-down energies (from a rotating magnetic dipole) of 10^{33-34} erg s^{-1}, which fall below their observed X-ray luminosities of 10^{35-36} erg s^{-1}. In this case, rotation of the neutron star is not the source of the observed emission from these sources. It was proposed early on that SGRs might be powered by large magnetic fields (see references above), while various scenarios were originally considered to power the emission from AXPs (accreting X-ray binaries and accreting stars with "fall-back" disks). Some of these sources are proposed to be associated with supernova remnants, suggesting that they are young NSs with unusual properties. Support for the magnetar model was found when pulsations were

detected for SGR 1806–20 and a spin-down rate was measured which implied a dipole magnetic field of $\approx 10^{15}$ G (Kouveliotou et al., 1998). In addition, SGR-like bursts have now been detected in many AXPs (Kaspi, 2007), strongly favoring a similar magnetar mechanism being responsible for the emission of both types of objects.

Observationally, these objects are characterized by spin periods in the range 2–12 s and inferred dipole magnetic fields of $\sim 10^{14-15}$ G. The observed spectrum at X-ray energies in the 0.5–10 keV range is usually fitted by a thermal plus non-thermal component, presumably due to surface and magnetospheric emission, respectively. Counterparts at optical and infrared (IR) have been detected for many of these objects, the emission from one (AXP 4U 0142+61) being pulsed at the period of the pulsar. Emission at X-ray energies above 10 keV has recently been found having similar luminosity as in the soft X-ray range ($\sim 10^{36}$ erg s^{-1}) but with a flatter spectrum, in addition to being highly pulsed. Despite numerous searches, no persistent radio emission from magnetars has been observed. However, the AXPs XTE J1810–197 and 1E 1547.0–5408 have shown remarkable, transient radio emission after large bursts, having flatter radio spectra than any NS known and being the brightest NSs at high radio frequencies (Camilo et al., 2006, 2007a).

The main features of the magnetar model that is currently used to describe the physics of these objects were first proposed by Duncan & Thompson (1992) and Thompson & Duncan (1995,1996). Here, the energy provided by a large magnetic field ($\sim 10^{14-15}$ G) is the origin of the persistent and burst emission observed from these sources. Such a large magnetic field decays rapidly, heating the core and inner crust of the star, which can account for the persistent thermal emission observed from magnetars. Field decay is thought to take place inside the star due to ambipolar diffusion (the combined drift of the magnetic field and electron-proton fluid relative to neutrons) and possibly due to Hall drift (the drift of the magnetic field and electron fluid relative to the ions).

The persistent non-thermal emission seen from magnetars below 10 keV is thought to arise from magnetospheric processes (Thompson et al., 2002; Lyutikov & Gavriil, 2006; Fernández & Thompson, 2007). In this case, it is speculated that the dynamo

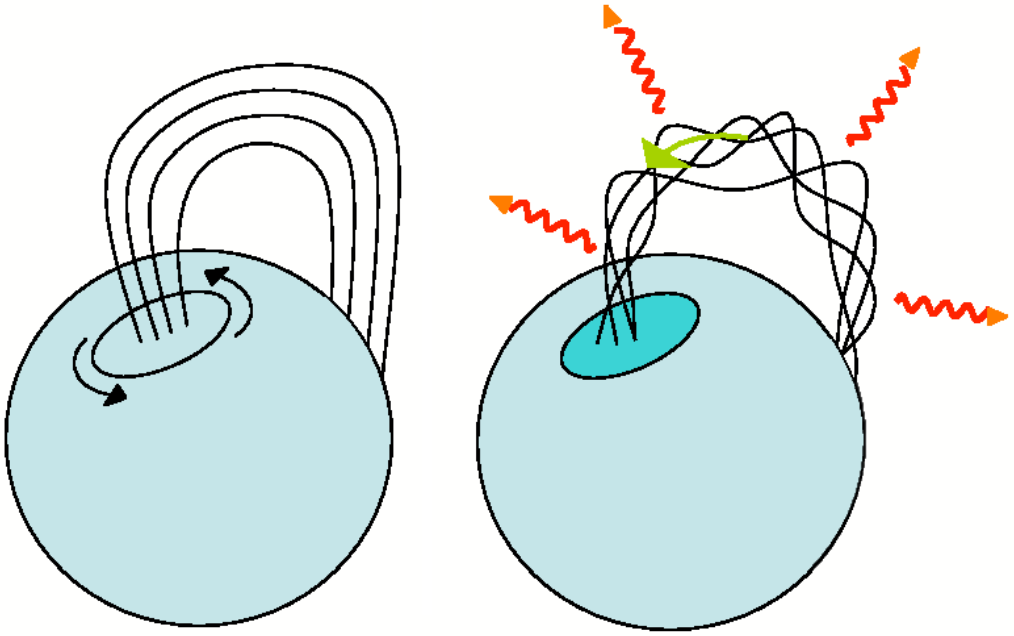

Figure 1.9: Schematic of magnetic field lines with an imparted twist. *Left*: Field lines anchored on the surface without a twist. Arrows show the possible directions in which the surface region can be moved due to the unwinding field in the interior. *Right*: As the surface moves it drags the magnetic field lines with it. The twisting of the field lines allows current to flow (denoted by the green arrow). In this model, currents can strike the surface and heat it, producing observable radiation. The currents in the magnetosphere can also upscatter low-energy photons to higher energies. Figure produced following that of Robert C. Duncan available at http://solomon.as.utexas.edu/∼duncan/magnetar.html.

process that creates a large magnetic field also winds it up internally. As it slowly unwinds and decays, it can impart stresses on crust regions and cause them to move. The magnetic field anchored on these regions also twists and causes currents to flow through it. Heavy charged particles (ions) can strike the surface and cause further heating, while electrons can be accelerated by the field and radiate non-thermal emission. The currents in the magnetosphere can also upscatter thermal photons from the surface (due to internal or magnetospheric heating) to higher energies and produce further non-thermal emission. In this way, twists in the magnetosphere are expected to alter the brightness and hardness of the observed spectrum, with larger twists producing brighter and harder emission. A schematic is shown in Figure 1.9.

The small bursts observed from these sources can be explained as crustal fractures on the surface due to the large stress that a twisted internal magnetic field can impart on it. Large bursts are proposed to arise by large-scale rearrangement and/or reconnection of the magnetic field after a large external twist. The origin of the quiescent emission in the hard X-ray/soft γ-ray band above 10 keV has been proposed to arise from various mechanisms (Baring, 2004; Thompson & Beloborodov, 2005; Heyl & Hernquist, 2005). These include upscattering of thermal photons to higher energies, synchrotron emission from highly accelerated particles, thermal free-free emission from a hot transition layer between the atmosphere and a corona, and pair-synchrotron cascades due to the breakdown of fast-mode MHD waves. The origin of the optical/IR emission in the magnetar scenario is not well understood, with a possible mechanism being accelerated particles in the corona (Beloborodov & Thompson, 2007).

Additional models have been put forward to explain the observed emission from these sources (Ertan et al., 2007a; Wang et al., 2006; Heyl & Hernquist, 2005). Active disk models propose that the quiescent X-ray emission arises due to accretion onto a NS with a dipole field of $\sim 10^{13}$ G from a surrounding disk. However, a magnetar strength field in the quadrupole or higher component is needed to account for the bursting behavior. Passive disk models suggest that a non-accreting disk is present, which is irradiated by the central source and is the source of the (unpulsed) optical/IR

emission (as is also the case in active disk models). QED models also propose that the energy released during a burst is not transported by the assumed Alfvén waves along the magnetic field lines, but by fast-mode MHD waves.

The absence of persistent, pulsed radio emission from magnetars has been hard to explain physically (Thompson & Duncan, 1996; Baring & Harding, 2001; Lyutikov, 2002). Although a large amount of pair-producing plasma is present in their magnetospheres, the pair instabilities that produce radio emission in normal rotation-powered pulsars must be inefficient in magnetars. The possibility that this mechanism is suppressed due to the high field is not supported by the fact that radio pulsars with *inferred* magnetic fields as high as some magnetars have been detected (and show no anomalous radio emission). The possibility that radio emission could be absorbed is also possible, although it is complicated by the fact that such absorption should only take place close to the surface during quiescence (where the particle densities are higher) and would imply that particle densities decrease below the quiescent value after large bursts (so radio emission can be seen at those times). On the other hand, the large periods seen in magnetars also imply small polar cap radii, so that the resulting small radio beams could be hard to detect and a large number of objects is needed to sample the parameter space.

1.8 Emission Mechanisms

Neutron stars and their associated structures emit electromagnetic radiation through a large number of physical mechanisms (Rybicki & Lightman, 1979). In the X-ray range, thermal and non-thermal emission is detected. Thermal emission from the surface is first simimated as blackbody radiation described by the Planck spectrum:

$$B_\nu(T) = \frac{2h\nu^3/c^2}{e^{h\nu/kT} - 1}, \tag{1.21}$$

where kT is the temperature of the object. The integrated luminosity over the surface area of the emitting region with radius R is given by $L_\nu d\nu = 4\pi^2 R^2 B_\nu d\nu$. In terms of the observed photon energy and assuming isotropic emission, the flux measured by

a distant observer is given by

$$F_E dE = \frac{L_E}{4\pi D^2} dE = 1.034 \times 10^{-3} \frac{E^3}{e^{E/kT} - 1} \left(\frac{R_{km}}{D_{10kpc}} \right)^2 dE \text{ ergs s}^{-1} \text{ cm}^{-2} \text{ keV}^{-1}, \tag{1.22}$$

where E is the photon energy in keV, kT is the temperature in keV, R_{km} is the emitting area in km, and D_{10kpc} is the distance to the source in units of 10 kpc. The peak of the spectrum is located at $E_{max} = 2.82\ kT$. Surface emission can also be described using atmosphere models as discussed in §1.4.3.

Non-thermal emission mechanisms observed in these objects include synchrotron radiation and ICS. In the case of synchrotron radiation produced as electrons spiral around magnetic field lines at high velocities, the angular frequency is given by $\omega_G = eB/\gamma m_e c$. The average power emitted by a single electron is then given by:

$$\langle P \rangle = \langle P' \rangle = \frac{2e^2 \langle a_\perp'^2 \rangle}{3c^3} = \frac{2e^2 \gamma^4 \langle a_\perp^2 \rangle}{3c^3} = \frac{2e^2 \omega_G^2 v^2 \gamma^4 \langle \sin^2 \alpha \rangle}{3c^3} = \frac{4}{3} \sigma_T \beta^2 \gamma^2 c U_B, \tag{1.23}$$

where the local and observer's reference frames are denoted by primed and unprimed quantities, respectively, α is the angle between the velocity $\boldsymbol{v}$ and the field $\mathbf{B}$, the Thomson cross-section is $\sigma_T = \frac{8\pi}{3}(e^2/m_e c^2)^2$, and the magnetic field energy density is $U_B = B^2/8\pi$. A synchrotron source is then assumed to have a power-law distribution of electron energies given by

$$N(E) = N_0 E^{-p} dE, \tag{1.24}$$

where p is the associated power law index. We then make the assumption that most of the power radiated by a single electron (Eqn. 1.23) is given off at a frequency $\nu \sim \gamma^2 \nu_G = \gamma^2 \omega_G / 2\pi$. The electron energy will then be given by

$$E = \gamma m_e c^2 \sim (\nu/\nu_G)^{1/2} m_e c^2 \propto B^{-1/2}, \tag{1.25}$$

which implies $dE/d\nu \sim m_e c^2 \nu^{-1/2}/2\nu_G^{1/2}$. The emission coefficient for synchrotron radiation from this ensemble of electrons is then given by

$$\begin{aligned} \epsilon_\nu d\nu &= -\frac{dE}{dt} N(E) dE = \langle P \rangle N(E) dE \\ \epsilon_\nu &\sim \left(\frac{4}{3}\sigma_T \beta^2 \gamma^2 c U_B\right) (N_0 E^{-p}) \left(\frac{m_e c^2 \nu^{-1/2}}{2\nu_G^{1/2}}\right) \propto B^{(1+p)/2} \nu^{-(p-1)/2}, \quad (1.26) \end{aligned}$$

which corresponds to an observed spectrum that is also described as a power law with spectral index of $\alpha = (p-1)/2$ or, interchangeably, a photon energy index of $\Gamma = (p+1)/2$. Over time, these electrons will lose energy as they radiate synchrotron emission. The timescale for this to happen, also known as the synchrotron lifetime, is given by

$$\tau_s = \frac{E}{dE/dt} \propto E^{-1/2} B^{-3/2}. \quad (1.27)$$

For X-ray emitting electrons, the estimated lifetime is given by $\tau_{X,s} = 1.2 E_{keV}^{-1/2} B_{-5}^{-3/2}$ kyr, where E_{keV} is the energy of the synchrotron photon in keV and B_{-5} is the magnetic field strength in units of 10^{-5} G.

In the case of non-thermal emission due to inverse-Compton upscattering (ICS) of low-energy photons by accelerated electrons, the power transferred to the photon radiation field by a single electron is given by:

$$P_{ICS} = \frac{1}{4}\sigma_T \beta^2 \gamma^2 c U_{rad}, \quad (1.28)$$

where U_{rad} is the energy density of the radiation field. For a power-law distribution of electron energies as in Equation 1.24, the observed spectrum has the same frequency dependence as that shown for synchrotron radiation in Equation 1.26 and in this case the lifetime of ICS-emitting electrons is given by $\tau_{\gamma,ICS} = 4.8 E_{TeV}^{-1/2} B_{-5}^{-2}$ kyr, where E_{TeV} is the energy of the ICS photon in units of TeV.

1.9 Thesis Outline

The results presented in this thesis deal with X-ray observations of a variety of NSs, including normal radio pulsars and anomalous X-ray pulsars. The goals of our work were to constrain their properties at these wavelengths and thus provide insight into the physical processes that determine their behavior. The rest of the thesis is structured as follows:

Chapter 2: Here we summarize the properties of the X-ray telescopes mainly used during the observations of our sources: the *XMM–Newton* and *Chandra* satellites (and to a lesser extent *Swift*). We also summarize the reduction and analysis techniques applied to the data during this work.

Chapter 3: In this chapter we describe our results of an *XMM–Newton* observation of the radio pulsar PSR B0154+61. The pulsar has a period of 2.35 s, characteristic age of 197 kyr and is one of the so-called "high magnetic field" radio pulsars with an inferred dipole magnetic field strength of 2.1×10^{13} G. The goal of this study was to search for enhanced X-ray emission due to the effects of a high magnetic field as is seen from magnetars. However, no emission from the source was detected and our derived upper limits show that magnetar-like mechanisms are not present in this source.

Chapter 4: In this chapter we present the results obtained from an *XMM–Newton* observation of the high magnetic field radio pulsar PSR J1119−6127. This pulsar has a period of 408 ms, characteristic age of 1,700 yrs and inferred magnetic field of 4.1×10^{13} G. We report the discovery of unusual X-ray emission from the source which, while not exactly magnetar-like, shows for the first time the possible effects of a high magnetic field in the heat transfer mechanism of the crust and envelope. We also summarize the currently known X-ray properties of other high magnetic field radio pulsars and speculate on the absence of magnetar-like emission from all of these sources.

Chapter 5: Here we describe our results of *XMM–Newton*, *Chandra*, *Swift* and *Gemini* observations of the AXP 4U 0142+61 expanding from 2000–2007. The goal of this work was to monitor the long-term behavior of this AXP, which despite being

very stable in the past has shown an unusual period of burst activity from 2006–2007. We report the discovery of changes to the total emission associated with this recent burst activity. However, these changes are present at a low level and imply that, unlike in other magnetars, long-term recovery regions (such as the crust) have not been significantly affected by the recent large bursts.

Chapter 6: In this chapter we present the results obtained from *XMM–Newton* and *Chandra* observations of the Vela-like radio pulsar PSR B1046−58. This pulsar has a period of 124 ms, characteristic age of 20.4 kyrs, inferred magnetic field of 3.5×10^{12} G and spin-down luminosity of 2×10^{36} ergs s^{-1}. PSR B1046−58 is also one of a handful of possible γ-ray pulsars and a possible unpulsed γ-ray component. Here we report the discovery of a pulsar wind nebula around this pulsar, which is both faint and has an elongated structure a few arcseconds in size. If the γ-ray emission can be confirmed with current and/or future γ-ray instruments (such as HESS and GLAST) this pulsar/PWN will belong to the growing class of NSs with reasonably faint X-ray emission ($\sim10^{32-33}$ ergs s^{-1}) while being some of brightest γ-ray sources in the population.

Chapter 7: Here we summarize our results for the NSs studied in this thesis and discuss future avenues of work for these sources and the questions they raise for the neutron star population as a whole.

Appendix: Here we present initial results from a *Chandra* observation of the Vela-like pulsar PSR B1823−13, whose PWN has been proposed to be the counterpart for the TeV source HESS J1825−137. Many questions are raised by these data regarding the association between these objects and our understanding of the production of such high-energy emission.

Chapter 2

X-ray Observatories and Data

In the past 40 years, the advances in X-ray astrophysics have mirrored those made by optical astrophysics over the last 400 years. The main drive for these advances has been the development of state-of-the-art technology. In this part of the electromagnetic spectrum, signals from astronomical objects are detected as individual photons of varying energy. Recording individual photons and their characteristics allows us to differentiate those produced by the astronomical source of interest and those produced by background processes. In this chapter we provide an overview of the X-ray observatories used during the course of this thesis, as well as an overview of the processing and analysis techniques carried out for X-ray data.

2.1 X-ray Observatories

2.1.1 Overview

The first X-rays of cosmic origin were detected in 1949, when radiation detectors aboard rockets were carried above the atmosphere and detected X-ray from the Sun. More than a decade later, improved detectors discovered X-ray coming from sources beyond the Solar System when NASA launched the *Uhuru X-ray Satellite* in the early 1970's. Over the next three decades, advances in the field were made systematically with the launch of observatories such as *Einstein*, *ROSAT*, *ASCA* and more recently *Chandra* and *XMM–Newton*, among many others.

Table 2.1: Characteristics of Different X-ray Satellites[a]

	Spatial Resolution (arcsec)	Energy Range (keV)	Area at 1 keV (cm^2)	FOV (arcmin)	Spectral Resolution ($E/\Delta E$)
XMM–Newton	MOS1/2 = 6/4.5	0.15–12	600	30	20–50
	PN = 6.6	0.15–15	1200	30	20–50
Chandra	ACIS-I/S = 0.5	0.2–10	800	17/8×48	20–50
	HRC = 0.4	0.2–10	800	30	–
Swift	XRT = 7	0.2–10	100	23	20–50
ASCA	GIS = 30	0.5–12	350	50	1–15
	SIS = 30	0.5–12	350	22	9–40
ROSAT	HRC = 2	0.1–2.4	400	38	–
	PSPC = 30	0.2–2.4	400	60	1–4
Einstein	IPC = 60	0.2–20	200	75	0.5–1
	HRC = 5	0.2–20	200	25	100–1000

[a] General properties derived for point sources on-axis. Spatial resolution varies with energy; value at optimal Full-Width at Half Maximum (FWHM) is listed. For additional details check the High Energy Astrophysics Science Archive Center (HEASARC, http://heasarc.gsfc.nasa.gov/), as well as the individual operating centres for each observatory (*Chandra*: http://cxc.harvard.edu/, *XMM–Newton*: http://xmm.vilspa.esa.es/, *Swift*: http://swift.gsfc.nasa.gov/).

NASA's *Einstein* Observatory, launched in 1978, was the first X-ray telescope with focussing mirrors. The *Roentgensatellit (ROSAT)*, a joint satellite project between Germany, the United Kingdom and the United States, carried an even larger X-ray telescope than *Einstein* into orbit in 1990. The *ASCA* satellite was launched in 1993 and was the first X-ray telescope that employed charged coupled devices (CCDs) in addition to having a significant effective area above 2 keV. The "new generation" of X-ray observatories (such as *Chandra* and *XMM–Newton*) used for the work presented in this thesis provide an unprecedented combination of large collecting area and large spatial resolution that allows the study of astronomical objects with great accuracy. Table 2.1 provides an overview of the main capabilities of past and present X-ray observatories. In the following sections we summarize the main capabilities offered by the *Chandra*, *XMM–Newton* and *Swift* satellites, used in this thesis. Figure 2.1 shows the effective areas of these telescopes for comparison[1] .

2.1.2 Optics

Imaging X-ray telescopes work on the principle of "grazing incidence" in order to focus X-ray photons. For example, in contrast to optical photons, X-rays would have enough energy to penetrate into a facing mirror instead of being reflected. In turn, grazing incidence works on the principle of re-directing the X-ray photons if they are reflected off mirrors that are positioned almost parallel to the incoming direction (the analogy to bullets ricocheting off walls at grazing angles is often made). Therefore, mirrors with a shallower incidence angle are able to focus X-ray photons of higher energies.

[1] For additional details check the High Energy Astrophysics Science Archive Center (HEASARC, http://heasarc.gsfc.nasa.gov/), as well as the individual operating centres for each observatory (*Chandra*: http://cxc.harvard.edu/, *XMM–Newton*: http://xmm.vilspa.esa.es/, *Swift*: http://swift.gsfc.nasa.gov/) and references therein.

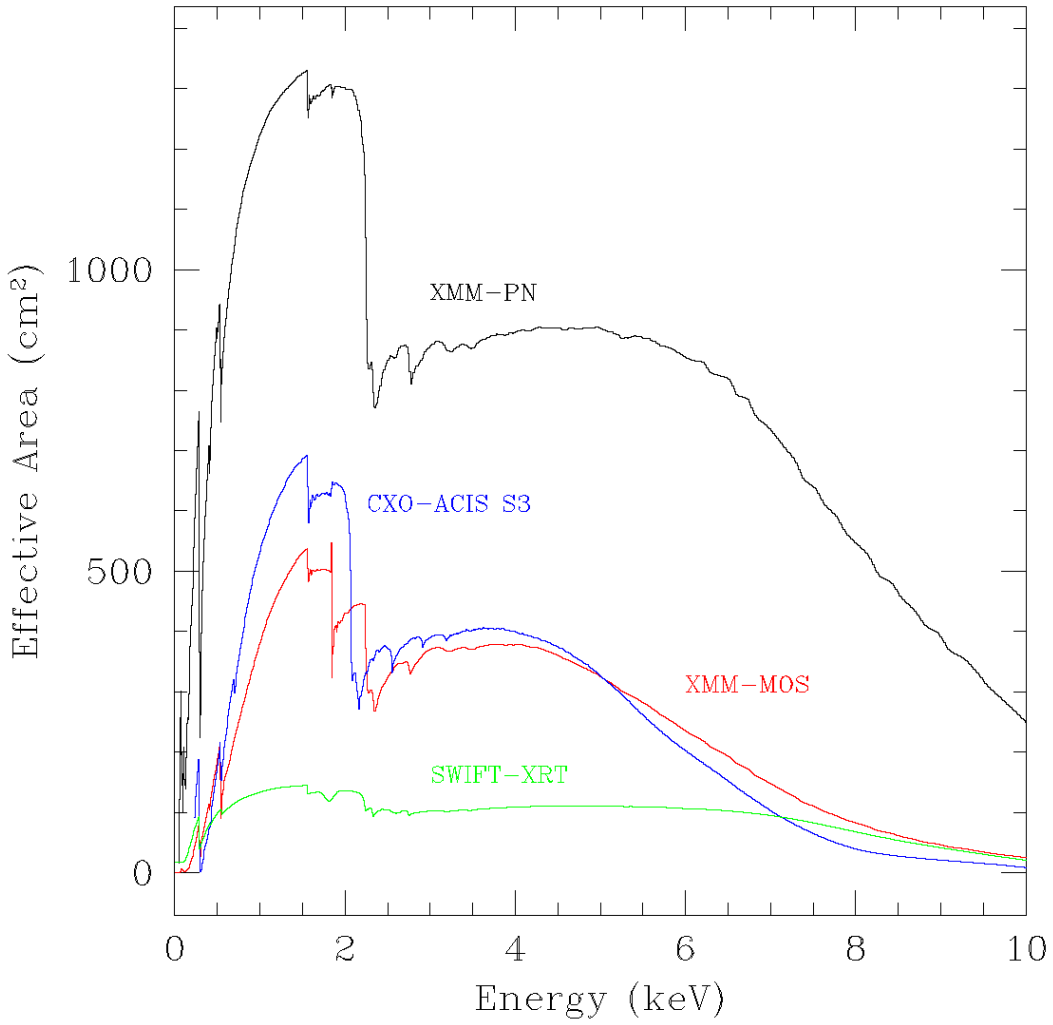

Figure 2.1: Effective areas for the X-ray telescopes used in this thesis. The curves are labeled according to the telescope and, in the case of *XMM–Newton*, the individual instruments used. These values take into account instrumental effects such as quantum efficiency and bad pixels, as well as the mirrors' effective areas. A point source on axis was assumed.

A set of two-stage mirrors are needed to redirect the photons to a focal point that is not too far away from the mirrors themselves: photons first encounter a paraboloid section followed by a hyperbolic section (as shown in Figure 2.2). In this way, barrel-shaped mirrors are created. The effective area of the telescope is increased by nesting mirrors inside each other and filling up the available space as much as possible. The thinner the mirror shells are and the nearer the shells are spaced, the larger the collecting area is (up to a point where nesting becomes inefficient mainly due to the gain in mass, and thus financing cost, being greater than the gain in effective area).

2.1.3 Detectors

In general, CCDs are a series of Metal Oxide Semiconductors (MOS) capacitors packed together for operation as a single array primarily composed of Silicon. Charge is generated through photo-absorption as a high-energy photon strikes the instrument and results in the liberation of a number of electrons proportional to the incident photon energy. This charge is collected in a potential well and transferred from neighbouring capacitors to an amplifier stage, where the output is converted from an analog to a digital signal by read-out electronics.

Normally, radiation is incident on the surface of the CCD that has "gates". These gates define the pixel boundaries by alternating voltages on three electrodes spanning a pixel. Photons must first pass through the gate structure before they can interact in the depleted Silicon (the region below the gates where most of the absorption takes place). These devices are then called "front-illuminated" CCDs. At low energies ($<$ 2keV), the characteristic absorption length of photons can be comparable to the thickness of the gates, reducing the low-energy detection efficiency.

One approach for increasing the low energy efficiency is to reverse the orientation of the device, such that the radiation does not have to propagate through the gates to interact with the depleted Silicon. A device operated in this fashion is called "back-illuminated" (BI). These CCDs can have lower high-energy ($<$ 5 keV) detection efficiency, increased non-linearity and lower spectral resolution. Therefore, the

choice of device depends on its applications and the specific scientific objectives of the instrument.

2.1.4 *Chandra*

The *Chandra* X-ray Observatory (CXO, formerly the Advanced X-ray Astrophysics Facility [AXAF]) was launched by the Space Shuttle Columbia on July 23, 1999. The *Chandra* orbit is highly elliptical and varies with time. As of December 2006, the apogee height was ≈122,500 km and the perigee height was ≈26,300 km. The orbit allows for reasonably high observing efficiency as the satellite spends most of the time well above the radiation belts (≈75%) and long continuous observations (≈160 ks) are made possible by the orbital period of 63.5 h.

The telescope uses a grazing incidence optic (called the High Resolution Mirror Assembly, or HRMA) that allows for spatial resolution of $0\farcs5$, the best available at X-ray energies. The HRMA consists of four nested mirrors of paraboloid and hyperboloid incidence with a focal length of 10 m. The capabilities of these mirrors are fully used by the CCD detectors coupled with them. The Advanced CCD Imaging Spectrometer (ACIS) and the High Resolution Camera (HRC) are the two primary focal plane instruments employed by *Chandra*. Data mainly from the ACIS detector was used for the work presented here.

As shown in Table 2.1, the ACIS detectors have excellent spatial resolution, moderate spectral resolution and high detector efficiency in the 0.2–10 keV band. They consist of ten individual CCDs, each of 1024×1024 pixels, arranged in two separate arrays. A schematic of the ACIS instrument is shown in Figure 2.3. Four of the chips are placed in a 2×2 array with a $17'\times17'$ field of view (FOV) intended for imaging of extended objects (ACIS-I). The other six chips are arranged in a 1×6 array (ACIS-S) intended primarily as a read-out detector for the High Energy Transmission Grating (HETG). However, two of the CCDs in ACIS-S are back-illuminated (see below) and

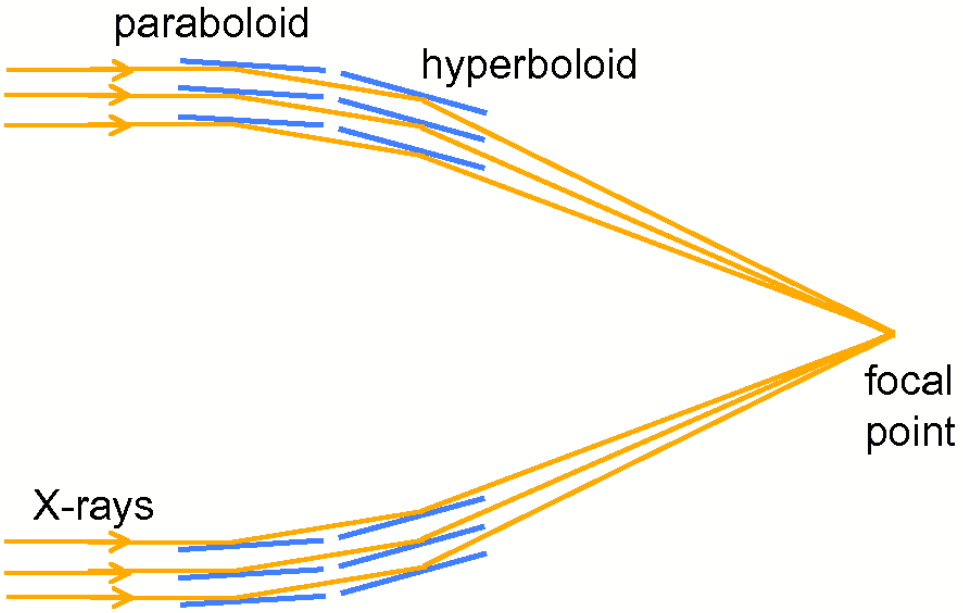

Figure 2.2: Schematic showing grazing incidence mirrors. A nested pattern of three mirrors is shown, each with paraboloid and hyperboloid sections.

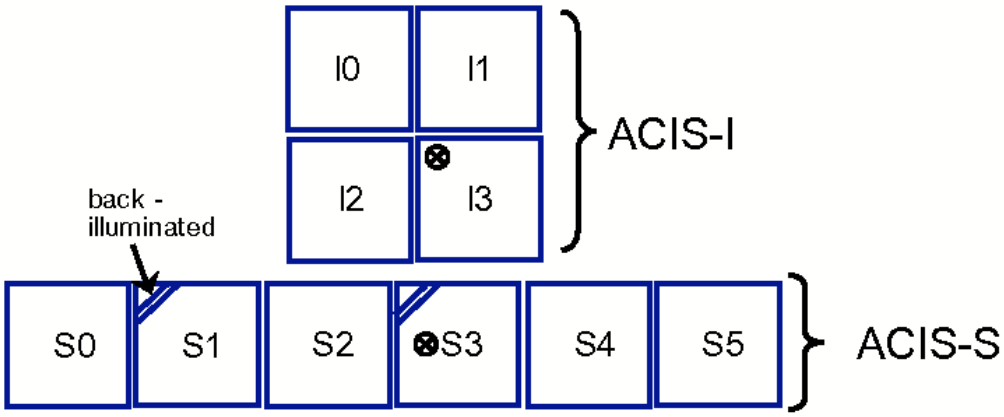

Figure 2.3: Configuration of the *Chandra* ACIS-I (*top*) and ACIS-S (*bottom*) instruments. The aimpoints of each configuration are marked with the crossed circles. Diagonal lines indicate those chips that are back-illuminated.

offer superior low-energy detection efficiency than the rest of the chips. Imaging observations with moderate spectral resolution using ACIS-S are therefore common.

2.1.5 *XMM–Newton*

XMM–Newton was launched on December 10, 1999 and is the largest science satellite ever built in Europe. The first part of its name refers to its X-ray Multi-Mirror design, while the second part honours Sir Isaac Newton (1642-1727). *XMM–Newton* also has a highly elliptical orbit, with an apogee of ≈115,000 km and a perigee of ≈6000 km. Its orbit provides the best visibility in the southern celestial sky and long (≈145 ks) uninterrupted observations.

XMM–Newton offers the largest effective area at X-ray energies of the telescopes used here as it carries three co-aligned X-ray telescopes, each consisting of 58 nested mirrors of grazing incidence having spatial resolution in the 4″.5–6″.6 range. The three accompanying focal plane instruments make up the European Photon Imaging Camera (EPIC), having two 'MOS' instruments and one 'PN' instrument.

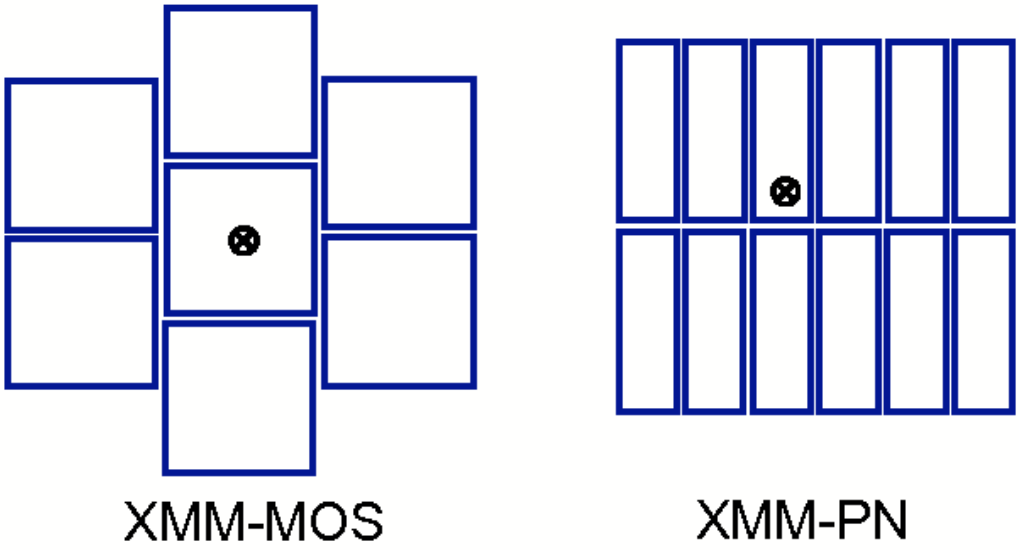

Figure 2.4: Configuration of the *XMM–Newton* MOS (*left*) and PN (*right*) instruments. The aimpoints of each configuration are marked with the crossed circles.

Each MOS camera consists of 7 front-illuminated CCDs with a central CCD in the focal plane and six surrounding ones. Each CCD consists of 600×600 pixels with a pixel size of $1\farcs1 \times 1\farcs1$ of the sky. The cameras have a total FOV of $30'$ and spatial resolutions, when combined with their respective mirror systems, of $6''$ (MOS1) and $4\farcs5$ (MOS2). The PN camera has 12 back-illuminated CCDs of 64×200 pixels each arranged in two rows of six CCDs. This camera has a FOV of $30'$, pixel size of $4\farcs1 \times 4\farcs1$ and spatial resolution of $6\farcs6$. Figure 2.4 shows a schematic configuration of the EPIC instrument.

2.1.6 *Swift*

Swift was launched on November 20, 2004 and is designed mainly to study gamma-ray bursts at optical/ultraviolet, X-ray and γ-ray wavelengths. The spacecraft was put into a circular orbit with a radius of ≈600 km. The Burst Alert Telescope (BAT) is its main instrument, designed to cover one sixth of the sky at all times at γ-ray energies. The X-ray Telescope (XRT) aboard *Swift* can also be used to study objects in the 0.2–10 keV range. It has grazing incidence mirrors with a FOV of $23'$. The XRT has a single MOS CCD camera at its focus with 600×600 pixels, each $2\farcs4 \times 2\farcs4$ in size, and a spatial resolution of $7''$.

2.2 X-ray Data

In the X-ray range, data are collected one photon at a time. In the case of the CCD instruments used for this work, the energy, position and time at which each photon was collected are recorded. From these data we can obtain several products: an image of where photons were detected, an energy spectrum of the photons collected, and a lightcurve of when the photons were detected. In addition, a combination of these properties can be used to create a wide range of by-products, such as energy-specific lightcurves, region-specific spectra, etc. The fact that all of this information is available for each detected photon also makes it easier to differentiate between background and source emission.

In general, the study of X-ray data can be separated into two different stages. First, the processing of the data is carried out, during which time the properties of the each photon are generated from the raw data that is recorded by the instruments. This allows for screening and filtering of a large number of background effects (such as cosmic rays). Second, the analysis of these data is done in order to derive images, spectra, lightcurves, etc, that can then be studied to derive the properties of the observed astronomical objects. An overview of these stages of X-ray data analysis is given next.

2.3 Data Processing

The raw data recorded by the spacecraft is first stored in FITS[2] (Flexible Image Transport System) files. These files are then processed by using information about the telescope and instruments to create "event files". For example, processing steps include applying corrections to the corresponding sky position of the photons detected according to the pointing position of the telescope with time (generally called an "aspect" correction). Each photon is also assigned a quality, or "grade", according to how many surrounding pixels it overlaps with when detected. In this way, trailed events produced by background high-energy particles (e.g., electrons and protons) can be distinguished from source events. In addition, for a given location in the CCD, a "gain" table is used to map the total charge per pixel (called the event's pulse height amplitude, PHA) to its corresponding physical energy value. Other corrections applied can include those accounting for the loss of charge in a CCD as it is shifted from one pixel to the next during readout (called "charge transfer inefficiency"), identifying pixels behaving anomalously ("hot pixels"), etc.

[2] The content of FITS files is not restricted to contain only images. They are meant to provide a convenient way of transporting data and are organized into a sequence of header-data units (HDU). The header contains "keyword=value" statements that describe the data, how it is organized and additional information about, e.g., the instruments or history of the data. The data itself can contain images, tables, and matrices.

Files that contain information about the spacecraft and instruments (usually contained in a Calibration Database) are needed to correct for most of these effects and are provided by the operating centre of each observatory. In addition, the software used to make these corrections and for subsequent analysis is also provided by the different mission centres. The event files produced after the above corrections are made contain information about each photon detected, including its energy, position, time of detection, and grade. Additional filtering of these data can be done by searching for periods of unusually high background and excluding photons with grades suggestive of a particle origin. After these final preparations, the resulting event files can then be analyzed to derive the properties of the objects being studied.

2.4 Data Analysis

The photons collected during the observation not only originate from the astronomical object of interest, but also from instrumental sources of noise, from the surrounding X-ray background (mainly other sources in the field, either resolved or unresolved, and possibly diffuse X-ray regions), and from charged particles and cosmic rays. The information available about each photon collected allows for easier discrimination between background and source events.

The data used in the work shown here allow for imaging, spectral and timing analyses to be performed. In the following we summarize the techniques used for each of these analyses.

2.4.1 Imaging Analysis

The location of each photon is recorded, allowing for a spatial map of the observed FOV to be made. Different regions can be selected as needed to study the sources of interest. For images representing a sizable fraction of the FOV, corrections due to the change in effective area at each position, including the effects of dithering of the telescope (when it applies), need to be made (called an "exposure correction"). In addition, since the energy and time of detection of each photon are also recorded,

images at a specific range of energies or times can be selected. Colour-coded images can be made by assigning different colours to images at different energy ranges and later combining them.

The faint regions of a source can be enhanced by applying a "smoothing" algorithm to the image. The purpose of this technique is to analyze the image in such a way as to blur low-level noise, however at the expense of blurring detail as well. A 2D symmetric Gaussian distribution has the form $\frac{1}{2\pi\sigma}\exp(-\frac{x^2+y^2}{2\sigma^2})$, where σ is the standard deviation of the distribution. The degree of smoothing (called the "smoothing scale" or "kernel size") is determined by the size of σ. The smoothing is then carried out by producing a discrete approximation of this function and "sliding" it over the image continuously until the whole original image is covered.

2.4.2 Spectral Analysis

The measured energy of each photon detected can be used to make a spectrum, defined as the number of counts per unit time per unit area as a function of energy. Spatial regions close to the object of interest and remote, source-free regions are used to determine the "source" and "background" spectra, respectively. In certain energy bins a low number of counts might have been detected (due to, e.g., the intrinsic spectrum of the source or the effective area of the instrument). In this case, χ^2 statistics (see below) cannot be used to assess the best-fit spectral model and its uncertainties. It is therefore common to rebin (or regroup) the energy bins in a spectrum such that ≥ 15 cts are present in each new bin. The improved signal-to-noise ratio then comes at the expense of reduced energy resolution.

Before the analysis of these spectra can be performed, it is necessary to generate "response matrices" to take into account instrumental effects on the detected photon energies. The redistribution matrix file (RMF) relates the observed PHA into energy units taking into account changes in the gain of the instrument over time and position. In turn, the ancillary response file (ARF) incorporates the effects of the effective area and sensitivity of the detectors as a function of position on the chip and time.

Once the spectra and response matrices are generated, different emission models can be fit to the spectra in the following way. A model is first assumed for the observed emission, which is then convolved with the instrumental responses and a predicted spectrum is produced. This assumed spectrum is then compared to the real spectrum and the quality of the match is computed. When using the χ^2 test, if $S_o(c)$ and $S_p(c)$ are the (spectrally independent) observed and predicted spectral counts as a function of the energy channel c, respectively, the χ^2 is given by:

$$\chi^2 = \sum_c \frac{[S_o(c) - S_p(c)]^2}{\sigma_o^2(c)} \tag{2.1}$$

where $\sigma_o(c)$ are the errors of the observed spectral counts at each energy channel. The best fit is obtained when the computed χ^2 is minimized. A good fit is generally given by $\chi^2_\nu = \chi^2/\nu \approx 1$, where χ^2_ν is called the reduced χ^2 and ν is the number of degrees of freedom in the fit (given by the number of spectral channel minus the number of free parameters).

The confidence level for each fitted parameter can also be estimated. For example, if the intrinsic value of a parameter is given by X_i and the fitted value is $X_f \pm \Delta X_f$, a 90% confidence level means that there is a 90% chance that $(X_f - \Delta X_f) < X_i < (X_f + \Delta X_f)$. To find the confidence interval for a parameter(s), the model is fixed at its best-fit values and the parameter(s) in question is varied while keeping note of the increase in χ^2 value. Specific values for the change in χ^2, $\Delta\chi^2$, correspond to different confidence intervals. If one parameter is being studied, a value of $\Delta\chi^2 = 1$ (2.706) corresponds to a 68% (90%) confidence interval as the parameter is changed to higher and lower values to derive the upper and lower limits, respectively. We can then say that there is a 32% (10%) that X_i lies outside the specified range.

2.4.3 Timing Analysis

The time recorded for each photon is given in terms of the internal clock carried by each spacecraft as it orbits the Earth. These times first need to be transformed to an inertial frame of reference; for astronomy this is the Solar System Barycenter

(SSB). A history of the position of the spacecraft with respect to the Earth (contained in the "orbit files") is used to correct for the photon travel times between the different locations and transform the recorded times to the SSB (called "barycentering").

The objects studied in this thesis are rapid rotators and the data used allowed for a study of their pulse properties. The rotation periods in this case are much smaller than the lengths of the observations. In order to increase the signal-to-noise ratio, the photons at each rotation phase throughout the observation can be added together (called "folding") to create a final histogram of the observed changes in the signal (called "pulse profile"). The barycentered times of detection first need to be transformed into a rotation phase using a reference epoch describing the rotation properties of the source. In the case of pulsars, the rotation phase can be found using:

$$\phi(t) = \phi_0(t_0) + \nu_0(t - t_0) + \frac{1}{2}\dot{\nu}_0(t - t_0)^2 + \frac{1}{6}\ddot{\nu}_0(t - t_0)^3 + \cdots \tag{2.2}$$

where ϕ is the phase of the photon (between 0 and 1), t is the time at which this photon was detected, t_0 is the epoch at which the reference phase (ϕ_0), rotation frequency (ν_0), and frequency derivatives ($\dot{\nu}_0$, $\ddot{\nu}_0$, ...) are measured. In addition, when the period of a signal is not well-known, a period search can be done by folding the data at various trial periods and measuring the changes in the resulting pulse profiles.

2.5 Summary

The excellent capabilities of the observatories and instruments used here have allowed for a broad study of the X-ray properties of the neutron stars included in this work. In the following chapters we provide further details of the specific data available, as well as the results and conclusions derived from our work.

Chapter 3

The High Magnetic Field Radio Pulsar PSR B0154+61

This chapter presents the results obtained from an *XMM–Newton* observation of the high magnetic field radio pulsar PSR B0154+61. This relatively nearby pulsar has a period of 2.35 s and an inferred dipole surface magnetic field strength of 2.1×10^{13} G. The goal of this observation was to search for enhanced X-ray emission possibly powered by its large magnetic field. However, no X-ray emission was detected from the position of PSR B0154+61 and the upper limit on its luminosity results in values much lower than those exhibited by known, persistent magnetars.

These results were first presented in the following publication: *Gonzalez, M. E.*, Kaspi, V. M., Lyne, A. G., & Pivovaroff, M. J., *An XMM-Newton Observation of the High Magnetic Field Radio Pulsar B0154+61*, Astrophysical Journal Letters, 610, L37−L40, 2004.

3.1 Introduction

The past two decades saw the emergence of a new class of X-ray pulsars (PSRs), which do not appear to be powered by the common rotation or accretion mechanisms. These "anomalous" X-ray pulsars (AXPs) are characterized by their long periods (∼2–12 s), persistent X-ray luminosities several orders of magnitude higher than their

spin-down luminosities and high inferred surface magnetic field strengths ($\sim 10^{14}$–10^{15} G). Together with Soft Gamma Repeaters (SGRs), these sources are thought to be "magnetars" (see §1.7 and references therein). Here, magnetic field decay from the stellar interior heats the star and results in the observed, persistent X-ray luminosities.

On the other hand, the X-ray emission of rotation-powered neutron stars (NSs) is believed to arise mainly from three regions – the magnetosphere, surface and polar caps (see §1.4.3 and §1.4.4). In particular, the surface emission arises from processes taking place deep within the stars. In young NSs ($\lesssim 10^5$ yrs) cooling through neutrino emission from the interior, the surface emission follows the thermal evolution of the core and is modified as it passes through the outer stellar envelope. In older stars ($\gtrsim 10^5$ yrs) cooling through photon emission, the neutrino production mechanism becomes inefficient and the thermal radiation from the surface governs the energy loss from the interior. The "standard" cooling predictions of NSs involve slow processes such as the modified Urca and bremsstrahlung mechanisms. The "fast" cooling predictions involve more exotic, efficient processes such direct Urca and possibly hyperons, pions, kaons and quarks. Therefore, observing the cooling radiation from these NSs offers the opportunity of constraining the structure of matter at supranuclear densities. In addition, this emission can provide insights into basic properties of the stellar surface, such as its temperature, composition and effective emitting area.

In order to test the above models of NS evolution, a broad sample of interesting sources must be studied. One such source is PSR B0154+61. It has a period $P = 2.35$ s, period derivative $\dot{P} = 1.89\times10^{-13}$, characteristic age $\tau_c = 197$ kyr, spin-down luminosity $\dot{E} = 5.7\times10^{32}$ ergs s^{-1} and inferred dipole surface magnetic field strength $B = 2.1\times10^{13}$ G (Arzoumanian et al., 1994). The pulsar's rotation period and inferred magnetic field are close to those exhibited by magnetars. In fact, its properties are very similar to those of the isolated neutron stars RX J0720.4–3125 and RX J1308.6+2127 (Kaplan & van Kerkwijk, 2005; Kaplan & van Kerkwijk, 2005), which show enhanced thermal emission and have been proposed to be old magnetars (Pons & Geppert, 2007). In addition, the intermediate age and low spin-down luminosity of PSR B0154+61 suggest that emission from initial cooling can still be present and for

thermal processes to dominate over nonthermal magnetospheric emission or emission from a pulsar wind nebula. From the dispersion measure[1] (DM) measured at radio wavelengths and a model of the free electron distribution in the Galaxy, the pulsar lies at a relatively close distance of ≈1.7 kpc (Cordes & Lazio, 2002), increasing the chance of detecting thermal emission from the NS surface. In this chapter, we show the analysis of an *XMM–Newton* observation of the pulsar and compare our results to those expected from magnetars and cooling neutron stars.

3.2 Observation and Data Analysis

PSR B0154+61 was observed with *XMM–Newton* on 2003 March 6. The European Photon Imaging Camera (EPIC) instruments MOS and PN were operated in full-window and small-window modes, respectively. In this case, the full FOV is available for the MOS instrument, while for the PN a region of $4'\times4'$ is used which results in faster readout of the data. These settings provide a temporal resolution of 1.4 s for MOS and 6 ms for PN. Light curves from source-free regions in these detectors were examined and no significant background changes or flares were found. The resulting exposure time for the two MOS detectors was 31 ks. For PN, only 70% of the live time was used in the small-window mode, resulting in an exposure time of 22 ks.

Individual images for a soft (0.3–2.0 keV) and a hard (2.0–10 keV) X-ray band were first obtained using the MOS1 data (see Figure 3.1). The coordinates of the pulsar derived from radio timing are[2] α_{2000}=$01^h57^m49\overset{s}{.}93(0\overset{''}{.}14)$ and δ_{2000}=$-58^\circ32'03\overset{''}{.}75(0\overset{''}{.}17)$,

[1] The ISM (mainly free electrons) disperses radio waves such that higher frequencies arrive at the detector earlier. The time delay between these signals can be used to calculate the "dispersion measure", defined to be the integrated column density of free electrons, n_e, towards a source at a distance d: DM = $\int_0^d n_e dl$. Using a model of the distribution of n_e in the Galaxy (e.g., Cordes & Lazio, 2002) then the distance to the source can be estimated.

[2] The ATNF Pulsar Database, http://www.atnf.csiro.au/research/pulsar/psrcat/.

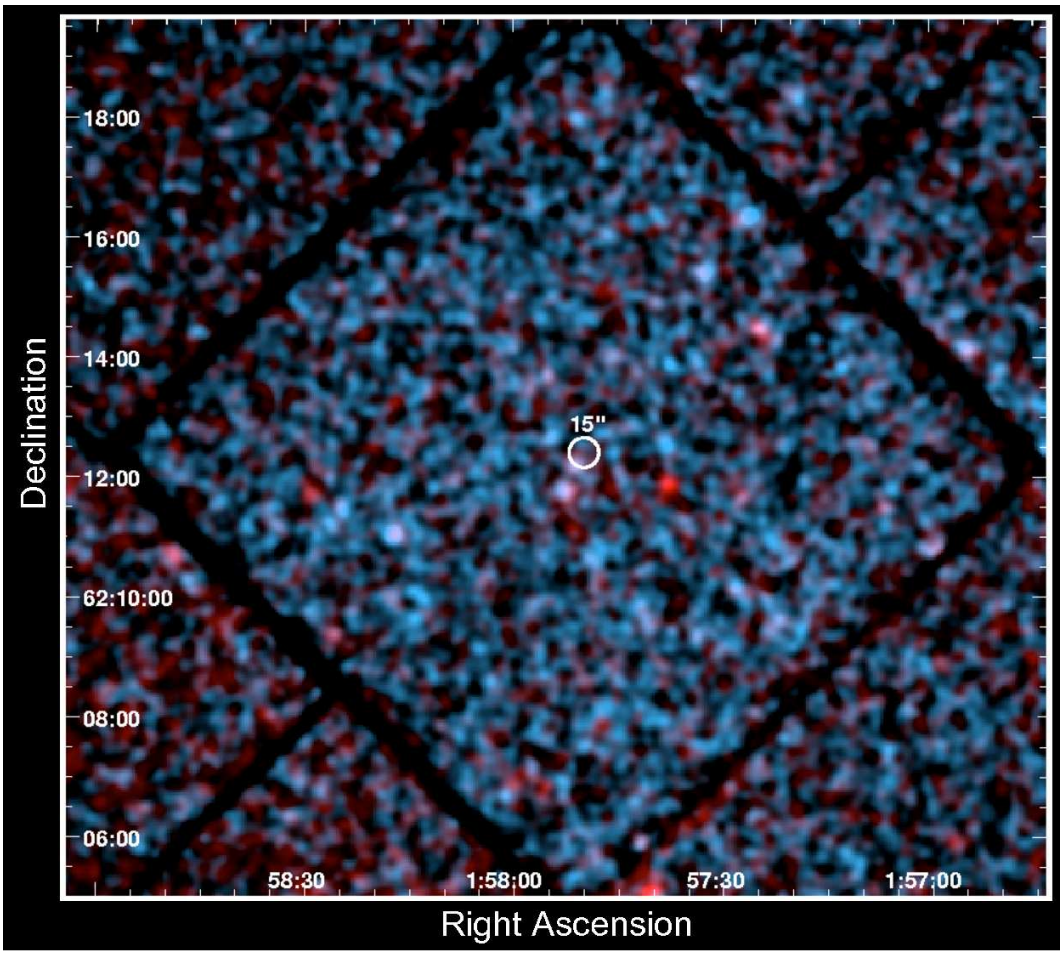

Figure 3.1: *XMM–Newton* MOS1 of the field containing PSR B0154+61. Individual images in the 0.3–2.0 keV (*red*) and 2.0–10 keV (*blue*) were first made with a pixel size of $2\farcs5 \times 2\farcs5$. These images were then smoothed with a Gaussian with $\sigma = 6''$ and later combined. The white circle has a radius of $15''$ and is centered at the radio position of PSR B0154+61.

1σ errors. Following the procedure outlined by the *XMM–Newton* Science Operation Center[3], the SAS source detection algorithms *evselect* and *eboxselect* were applied to the data. As suggested from visual inspection, no X-ray counterpart for PSR B0154+61 was found in the MOS data down to the S/N $\approx 2.5\sigma$ level. The closest source to the radio coordinates is located $\approx 45''$ away. The same result was obtained when analysing the MOS2 and PN data with the above algorithms.

3.3 Results

Although no direct emission was detected from PSR B0154+61, we can derive upper limit estimates on its detection, which can then be used to derive limits on its emission properties (such as temperature and luminosity if we assume that thermal emission would be present). To increase our sensitivity, the following results are derived using the combined MOS1 and MOS2 counts. The simulated spectral models were folded through the response matrices of the MOS1 detector, with identical results obtained if using MOS2. Because of the combined counts, the limits derived using the PN detector are just slightly lower.

In order to calculate an upper limit on the MOS count rate, we compare the counts collected from an aperture of radius $15''$ centered on the radio coordinates of the pulsar with those of a concentric annulus with radii $15''$–$20''$. Following the method described by Pivovaroff et al. (2000)[4], a detection at the S/N $> 3\sigma$ level requires an upper limit in the 0.5–10.0 keV band of $\lesssim 1.3\times10^{-3}$ counts s^{-1}. We can then use this upper limit on the count rate to estimate an upper limit on the star's surface temperature and

[3] http://xmm.vilspa.esa.es/external/xmm_sw_cal/sas_frame.shtml

[4] Here, we define $S/N = S/\sqrt{S - b(1+\beta)}$, where the background-subtracted counts are given by $S = N_s - b$, the background counts are $b = \beta N_b$, the original source and background counts are N_s and N_b, respectively, while $\beta = A_s/A_b$ is the ratio of the effective exposure areas of the source (A_s) to the background (A_b) regions.

luminosity. In turn, these values can be compared to those observed for other objects, such as AXPs, and the values predicted from NS cooling models.

A simple estimate for the temperature and luminosity at the pulsar's surface can be made by assuming a blackbody spectrum modified by interstellar absorption. The model bbodyrad, available with XSPEC v11.1.0, was then used (see also §1.8). The model depends on the surface temperature kT (in keV) and emission measure of the source. Here, the emission measure is given by R_{km}^2/D_{10}^2, where R_{km} is the NS's radius (in units of km) and D_{10} is the distance (in units of 10 kpc). In our simulations, we use the canonical value for the NS radius of 10 km and, as a first try, a distance of 1.7 kpc as suggested by the pulsar's DM. Holding these parameters fixed for each run (as well as the insterstellar absorption, see below) allows us to fit for the neutron star temperature needed to reproduce the upper limit on the count rate.

Furthermore, an estimate for the amount of interstellar absorption (N_H) in the direction of the pulsar is needed[5]. A first approximation can be made by assuming 10 neutral hydrogen atoms for each free electron (Seward & Wang, 1988, from an average density of 0.3 atoms cm^{-3}), giving a value of $N_H = 1{\times}10^{21}$ cm^{-2}. Perhaps a more reliable estimate is possible by using a set of reference interstellar medium column densities close to the pulsar's location in the Galaxy. Such reference data are available through the Extreme Ultraviolet Explorer (EUVE) data analysis tools[6]. For the ten sources closest to the pulsar in space that are listed, at distances from the Earth of 1.1–2.3 kpc, the reference data find an average absorption of $N_H{\approx}2{\times}10^{21}$ cm^{-2}, with

[5] X-rays from distant sources will be absorbed by atoms in the ISM due to photoelectric absorbtion. The measured flux is reduced, resulting in a measured value $F = F_0 e^{-\sigma_Z(E)\int n_Z dl}$, where F_0 is the intrinsic flux, $\sigma_Z(E)$ is the cross section of the absorbing element Z as a function of the photon X-ray energy E, and n_Z is the number density of the absorbing element. In the case of interstellar absorption due to hydrogen, the hydrogen column density is given by $N_H = \int_0^d n_H dl$.

[6] http://archive.stsci.edu/euve/ism/ismform.html

a range of (0.7–3.0)$\times 10^{21}$ cm^{-2}. In addition, the total Galactic column density[7] in the direction of the pulsar is 9.5×10^{21} cm^{-2}. The EUVE estimates are thus reasonable given the pulsar's close distance, they also agree with our first approximation and are therefore used in the following calculations.

At the DM distance of 1.7 kpc and assuming an average absorption of $N_H = 2\times 10^{21}$ cm^{-2}, the upper count rate limit estimation results in an effective blackbody surface temperature of $T^{\infty}_{bb,eff} \lesssim 63$ eV and unabsorbed X-ray luminosity in the 0.3–10.0 keV band of $L_X \lesssim 0.6\times 10^{32}\ D^2_{1.7}$ ergs s^{-1}, where $D_{1.7}$ is the distance in units of 1.7 kpc. Taking the full range of N_H values from above into account, we get $T^{\infty}_{bb,eff} \lesssim$ 55–67 eV and $L_X \lesssim$ (0.2–0.8)$\times 10^{32} D^2_{1.7}$ ergs s^{-1}. Figure 3.2 shows a plot of these values; the shaded regions represent the temperature predictions from NS cooling models (see below). In addition, allowing for a conservative error in the DM distance of 30%, the upper limits at the highest estimated N_H value are $\lesssim 73$ eV and $\lesssim 1.4\times 10^{32} D^2_{2.2}$ ergs s^{-1} for the temperature and unabsorbed 0.3–10.0 keV luminosity, respectively ($D_{2.2}$ is the distance in units of 2.2 kpc). It is also worth noting that individual pulsar distances measured from other techniques can vary significantly from the DM distance (sometimes by a factor of $\sim$3, e.g., Brisken et al., 2003). Such a high discrepancy in the distance to PSR B0154+61 would greatly affect our results. An independent determination of the distance (using, e.g., parallax) would therefore improve our understanding of this object.

3.4 Discussion

3.4.1 Implications for Cooling Models

The above temperature estimates can also be compared to those predicted from NS cooling models. However, the effects of an atmosphere and high magnetic field must first be taken into account.

[7] http://heasarc.gsfc.nasa.gov/cgi-bin/Tools/w3nh/w3nh.pl

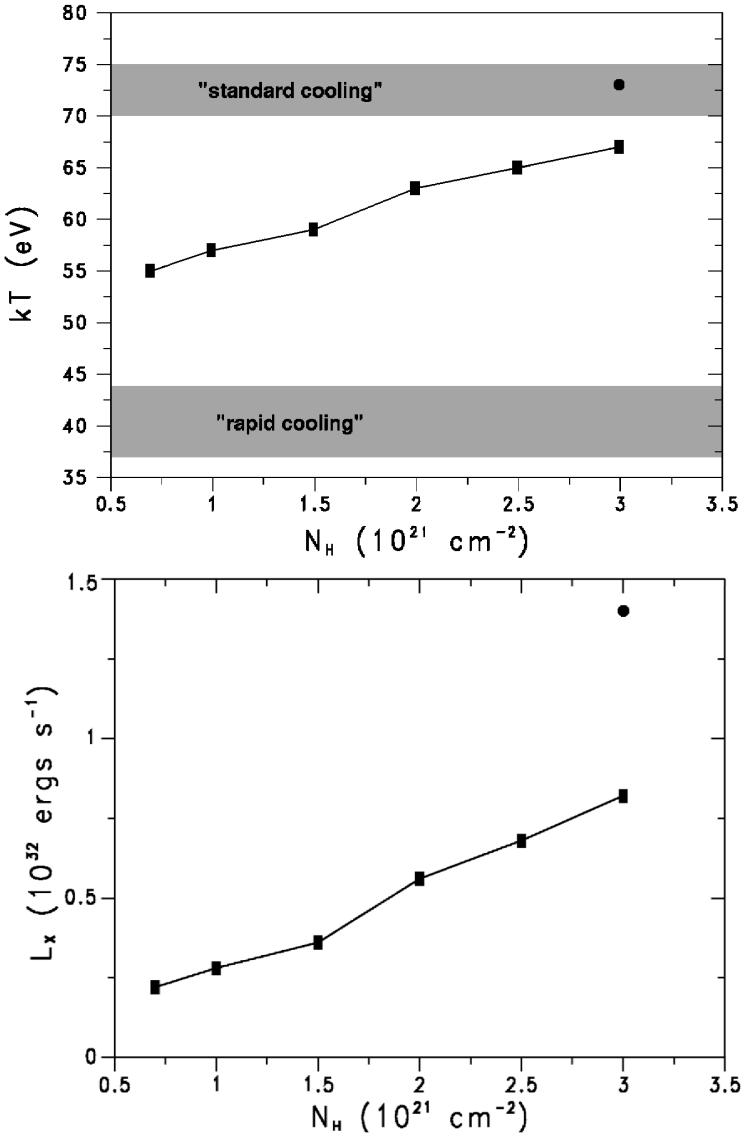

Figure 3.2: Upper limits derived for the blackbody surface temperature (*top*) and unabsorbed 0.3–10.0 keV luminosity (*bottom*) of PSR B0154+61 with *XMM–Newton*. The squares represent limits derived assuming the DM distance of 1.7 kpc, and the circle represents the upper limit at a distance of 2.2 kpc (see §3.3). The predicted temperature ranges from "standard" and "rapid" cooling models are also shown (without the effects of superfluidity, see Page 1998).

The spectrum from a NS atmosphere can be very different from a blackbody. A light-element atmosphere (such as H or He) will have an apparently harder X-ray spectrum than a blackbody at the same effective temperature (see §1.4.3). Therefore, these atmospheres have temperatures T_{atm} significantly lower than that measured using a blackbody T_{bb}, with ratios usually on the order of $T_{bb}/T_{atm} \approx 1.5$–3 (e.g., McGowan et al., 2003; Pavlov et al., 2002). However, in order to provide the same bolometric flux, a light-element atmosphere gives a larger size for the emitting region, or conversely, a distance that is too small. On the other hand, heavy-element atmospheres (such as Fe) have overall high-opacity trends that produce spectra much closer to a blackbody than light-element atmospheres, and in some cases with $T_{bb}/T_{atm} \lesssim 1$ (see, e.g., Rajagopal et al., 1997; van Adelsberg & Lai, 2006). In addition, magnetized atmosphere models with either light or heavy elements have shown that a high magnetic field ($B \gtrsim 10^{13}$ G) will increase opacities and produce emergent spectra closer to a blackbody. In this case, light-element atmospheres still produce a further deviation from a blackbody than heavy-element atmospheres.

Therefore, our derived upper limit values for the surface temperature of PSR B0154+61 would decrease in the presence of the light-element atmosphere on the NS. For a ratio of $T_{bb}/T_{atm} \approx 1.5$ (on the low end of the observed and predicted values, including magnetized atmospheres), our highest surface temperature estimate of $T_{bb} \lesssim 73$ eV would imply $T_{atm} \lesssim 49$ eV. However, the presence of a heavy-element atmosphere would agree with our original value.

For a characteristic age of τ_c=197 kyr as derived for PSR B0154+61[8], standard cooling models predict a NS surface temperature of $T_{std} \approx$ 70–75 eV, while rapid cooling models predict $T_{rapid} \approx$ 37–44 eV (not including the effects of superfluidity for standard cooling; see Figure 3.2). Unfortunately, at the above age the pulsar is located close to the transition stage between the neutrino and the photon cooling eras (see §3.1), where predictions are very sensitive to the specific model parameters. Consequently, different results are produced from various models accounting for the atmospheric composition and magnetic field of the star.

If a light-element atmosphere is indeed present, our temperature upper limit would be lowered to $T_{atm} \lesssim 49$ eV, favouring the presence of faster cooling processes such as superfluidity and direct Urca. However, a heavy-element atmosphere would imply an upper limit of $T_{atm} \lesssim 73$ eV, in closer agreement with the values predicted from standard cooling models. At present, light-element atmospheres are somewhat favoured over heavy-element atmospheres from high-resolution X-ray spectra of numerous NSs (see Pavlov et al., 2002, for a review). In this case, the presence of additional cooling mechanisms would be favored. However, given the large range of allowed parameter space for these models it is difficult to make a definite conclusion regarding initial cooling emission.

[8] This age is probably not an overestimate as a birth spin period $P_0 \ll P$ is likely for this long-period pulsar. However, an underestimate of τ_c by a factor of >10 would imply a braking index n<1.2 (comparable to that estimated for the Vela pulsar, Lyne et al., 1996) which cannot be ruled out and would have major implications for the evolution of the pulsar population as a whole. Observationally, PSR B1951+32 and PSR 1811−1925 have been proposed to have true ages lower than their spin-down age by a factor of a few and a factor of ∼10, respectively (Migliazzo et al., 2002; Kaspi et al., 2001), while PSR B1757−24 is proposed to be older by a factor of a few (Blazek et al., 2006). An uncertainty by a fact of a few in the case of PSR B0154+61 is therefore possible and in the case that it was older it would greatly reduce the predicted temperatures from cooling models.

Table 3.1: Comparison of High-Magnetic Field Radio Pulsars with Persistent AXPs

Name	P (sec)	τ_c (kyr)	B (10^{13} G)	$\dot{E}$ (ergs s^{-1})	L_X (ergs s^{-1})
AXPs[a]:					
CXOU 010043.1–721134	8	6.8	39	1.4×10^{33}	4×10^{34}
4U 0142+61	8.69	70	13	1.2×10^{33}	7×10^{34}
1E 1048.1–5937	6.45	$\approx$3.8	$\approx$42	$\approx40\times10^{33}$	3×10^{34}
RXS 1708–4009	11.0	9	47	5.7×10^{33}	2×10^{35}
1E 1841–045	11.8	4.5	71	9.9×10^{33}	1.1×10^{35}
1E 2259+586	6.98	230	5.9	0.55×10^{33}	4×10^{34}
HBRPs[b]:					
J1847–0130	6.7	83	9.4	1.7×10^{32}	$<$ (3–8)$\times10^{33}$
J1814–1744	4.0	85	5.5	4.7×10^{32}	$< 4.3\times10^{33}$
B0154+61	2.35	197	2.1	5.7×10^{32}	$< 1.4\times10^{32}$

[a] Luminosities are persistent values in the absence of bursts. Values are unabsorbed and in the 2–10 keV range.
[b] Luminosities are unabsorbed and in the 0.5–10 keV range (except for PSR J1814–1744, which is the 2–10 keV range).

3.4.2 Implications for Magnetar Models

PSR B0154+61 is one of a few pulsars which exhibit spin characteristics similar to those of SGRs and AXPs. However, given our luminosity upper limits, its X-ray emission is apparently very different from these objects.

As discussed in §3.1, emission from high-magnetic field sources such as AXPs/SGRs has been explained by the magnetar model. Here, their X-ray and γ-ray luminosities are attributed to the decay of their ultrastrong magnetic field. The properties for these objects can be well explained using this model, which also allows for an evolutionary link to be made between the two classes of objects. However, an important challenge is to understand the difference between the emission characteristics of magnetars and radio pulsars with similarly high (estimated) magnetic field (sometimes referred to as 'high magnetic field radio pulsars', HBRPs).

In this effort, several HBRPs have now been observed at X-ray wavelengths (e.g., Pivovaroff et al., 2000; McLaughlin et al., 2003). Table 3.1 compares the properties of a few of these pulsars with those of persistent AXPs (Woods & Thompson, 2006;

Kaspi, 2007) and illustrates that the high-energy emission mechanisms of these objects must be greatly different. These radio pulsars have dipole magnetic fields in the range $B{\sim}10^{13}$–10^{14} G. This is a regime which, if magnetar-like behavior depends exclusively on the inferred value of the magnetic field, should yield similar X-ray luminosities for these objects, contrary to what is observed.

In the following chapter we will present results from X-ray observations of another HBRP, PSR J1119−6127, and we will discuss in detail the discrepancies between the emission characteristics of these radio pulsars and magnetars. We will also discuss some of the current ideas proposed to explain these discrepancies.

3.5 Summary

We have derived upper limits for the allowed temperature and luminosity of the HBRP PSR B0154+61 using *XMM–Newton*. These values are consistent with the predictions of standard cooling models given the large range of parameter space allowed in these models and our results. However, in the case that a light-element atmosphere is present, the derived limits for the temperature would argue for the presence of enhanced cooling processes, such as superfluidity or direct Urca. Despite its high magnetic field, the emission from PSR B0154+61 is well below the persistent emission observed from AXPs. In the following chapter we discuss this issue in more detail.

Chapter 4

The Young, High Magnetic Field Radio Pulsar PSR J1119−6127

This chapter shows the results obtained from an *XMM–Newton* observation of the radio pulsar PSR J1119−6127, which has an inferred age of 1,700 yr and surface dipole magnetic field strength of 4.1×10^{13} G. We report the discovery of thermal emission that is pulsed, with an unusually large pulsed fraction, that makes PSR J1119−6127 the radio pulsar with smallest characteristic age from which thermal X-ray emission has been detected. This discovery allows us compare the observed characteristics with models of neutron star surface emission. Although unusual, these characteristics are not exactly magnetar-like and we also discuss the properties of HBRPs compared to those of magnetars.

This work was originally published in the following articles:

– *Gonzalez, M. E.*, Kaspi, V. M., Camilo, F., Gaensler, B. M., & Pivovaroff, M. J., *Unusual Pulsed X-Ray Emission from the Young, High Magnetic Field Pulsar PSR J1119−6127*, Astrophysical Journal Letters, 630, 489−494, 2005, and

– *Gonzalez, M. E.*, Kaspi, V. M., Camilo, F., Gaensler, B. M., & Pivovaroff, M. J., *PSR J1119−6127 and the X-ray emission from high magnetic field radio pulsars*, Astrophysics and Space Science, 308, 89−94, 2007

4.1 Introduction

The most commonly studied neutron stars (NSs) are radio pulsars, generally thought to be powered by the loss of rotational kinetic energy due to magnetic braking. As discussed in Chapter 1, the thermal X-rays observed from some pulsars are thought to be emitted at the surface and to originate from initial cooling or from polar caps reheated by magnetospheric processes (see, e.g., Kaspi et al., 2006, for a review). At low X-ray energies, this thermal emission shows broad pulses of low amplitude. In contrast, highly modulated non-thermal X-rays showing narrow pulses are thought to arise from synchrotron emission in the magnetosphere (e.g., Cheng & Zhang, 1999; Becker & Aschenbach, 2002). Thus, X-ray studies of radio pulsars are an excellent diagnostic of the physics governing NS emission.

Many radio pulsars with estimated dipole magnetic fields in the range $\sim 10^{13-14}$ G have now been discovered, showing that radio emission can be produced in neutron stars with fields above the quantum critical field $B^e_{qed} = 4.4\times10^{13}$ G. The distribution of some of these pulsars in the $P - \dot{P}$ diagram is illustrated in Figure 4.1. As the inferred magnetic field strengths of radio pulsars and magnetars are now found to overlap, the underlying physical reasons for the differences in their emission properties remains a puzzle. To date, no radio pulsar has been observed to exhibit magnetar-like emission at high energies, posing an interesting challenge to current emission theories.

PSR J1119−6127 was discovered in the Parkes Multibeam Pulsar Survey (Camilo et al., 2000). It has a spin period $P = 0.408$ s $\equiv 1/\nu$ and period derivative $\dot{P} = 4.1\times10^{-12}$. The measured braking index for the pulsar of $n = 2.91\pm0.05$ ($\dot{\nu} \propto -\nu^n$) implies an upper limit for the age of 1,700 yr, making it one of the youngest pulsars known. The pulsar has a spin-down luminosity of $\dot{E} = 2.3\times10^{36}$ erg s^{-1} and an inferred surface dipole magnetic field strength of $B = 4.1\times10^{13}$ G. This value of B is among the highest known in the radio pulsar population. PSR J1119−6127 powers a small ($3''\times6''$) X-ray pulsar wind nebula (PWN, Gil & Sendyk, 2003) and lies close to the centre of the $15'$-diameter supernova remnant (SNR) G292.2–0.5 (Crawford et al., 2001; Pivovaroff et al., 2001). HI absorption measurements imply a kinematic distance for the remnant of 8.4±0.4 kpc (Caswell et al., 2004), in agreement with estimates

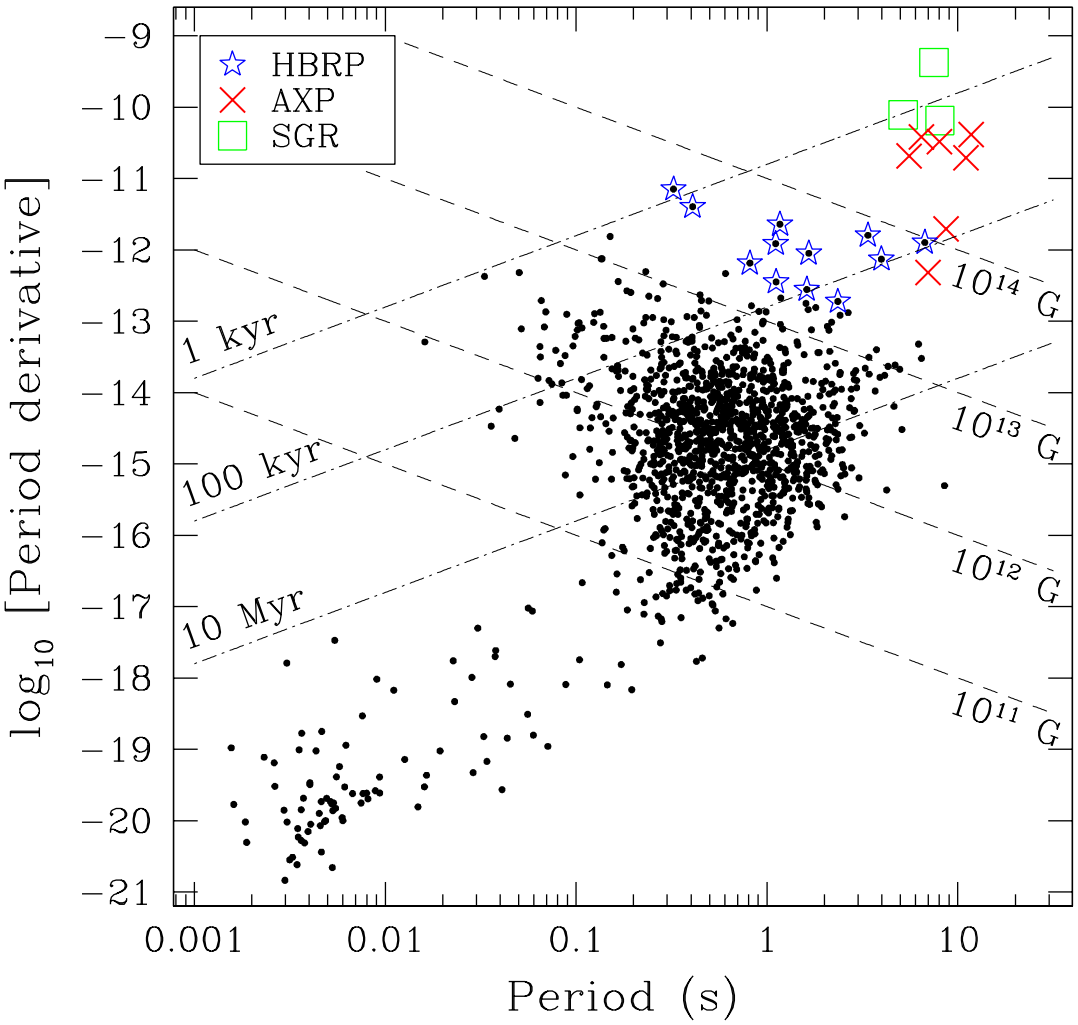

Figure 4.1: $P - \dot{P}$ diagram showing high magnetic field radio pulsars (HBRPs) with estimated magnetic fields $>2\times10^{13}$ G as a reference. Magnetars are also showns as labeled.

made from its location in the Carina spiral arm (Camilo et al., 2000). Unfortunately, no estimates for the age of this remnant are available.

4.2 Observation and Imaging Analysis

SNR G292.2–0.5 and PSR J1119−6127 were observed with *XMM–Newton* on 2003 June 26. The European Photon Imaging Camera (EPIC) instruments MOS and PN were operated in full-window and large-window mode, respectively. The resulting temporal resolution was 2.6 s for MOS and 48 ms for PN. The last 5 ks of the PN observation were rejected due to high radiation. The resulting exposure time was 48 ks for MOS1/MOS2 and 43 ks for PN.

Figure 4.2 shows the combined MOS image of the system in the 0.3–1.5 keV (*red*), 1.5–3.0 keV (*green*) and 3.0–10.0 keV (*blue*) bands. Individual MOS1/MOS2 images were first binned into pixels of $2\farcs5\times2\farcs5$ and other point sources in the field were excluded. These images were then added and adaptively smoothed with a Gaussian with σ=5″–15″ to obtain signal-to-noise ratios higher than 3σ. Background images and exposure maps at each energy band were similarly obtained and used to correct the final images. The detailed spatial distribution in the 3.0–10.0 keV (*blue*) image should be examined with caution as this energy band suffered from a high degree of stray-light contamination on *XMM–Newton*'s mirrors from a nearby high-energy source.

Here we focus on the bright source at the centre of Figure 4.2, which has coordinates $\alpha_{2000}=11^h19^m14\farcs65$ and $\delta_{2000}=-61°27'50\farcs2$ (4″ error). This position coincides with the *Chandra* and radio coordinates of PSR J1119−6127. The spatial resolution of *XMM–Newton* (half-power diameter of 15″) does not allow for the arc-second scale PWN discovered with *Chandra* to be resolved. The image reveals for the first time the detailed morphology of the SNR at X-ray energies. The large east-west asymmetry in the remnant at low energies has been attributed to the presence of a molecular cloud on the east side of the field (Pivovaroff et al., 2001).

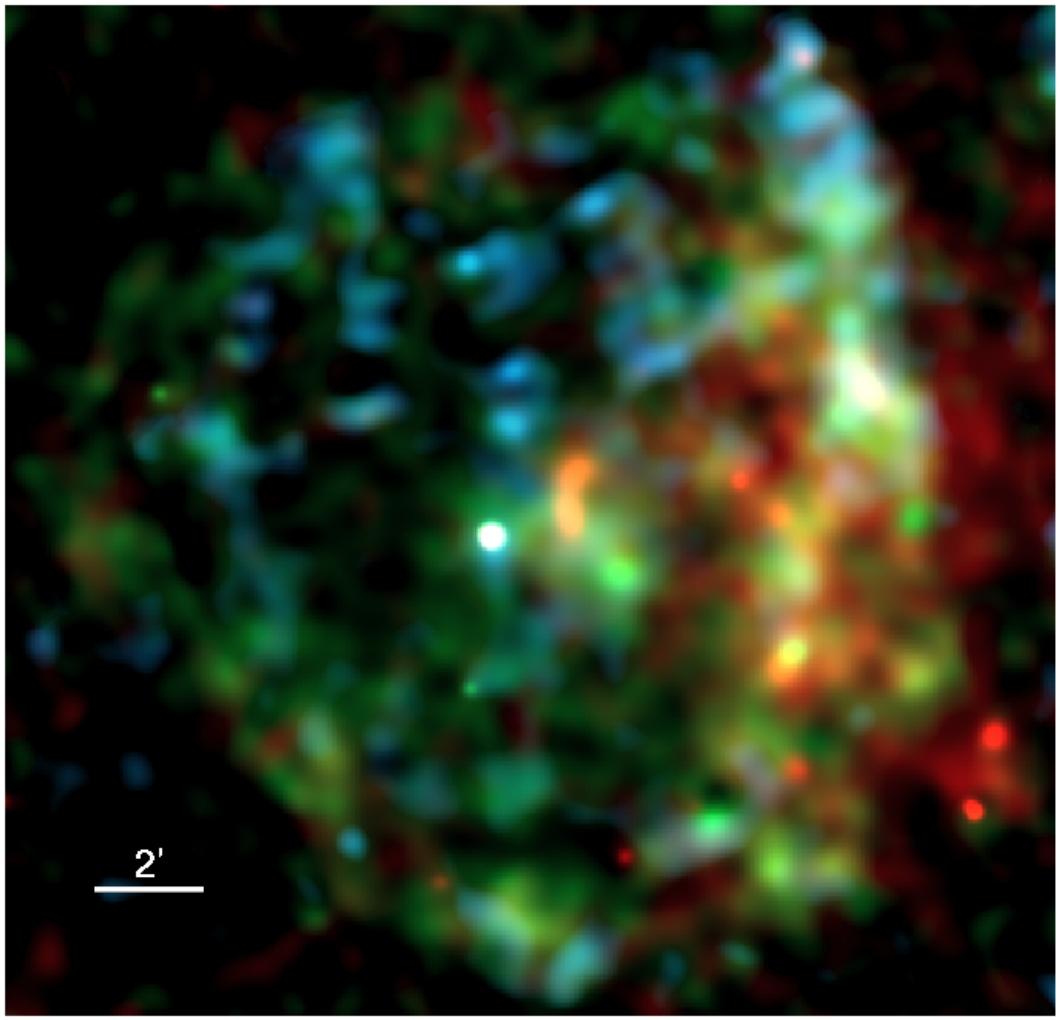

Figure 4.2: Combined MOS image of SNR G292.2–0.5 and PSR J1119−6127 in the 0.3–1.5 keV (*red*), 1.5–3.0 keV (*green*) and 3.0–10.0 keV (*blue*) bands. Individual MOS1/MOS2 images at each energy range were added and adaptively smoothed with a Gaussian with σ=5″–15″ to obtain signal-to-noise ratios higher than 3σ.

4.3 Timing Analysis

The PN data were used to search for pulsations from PSR J1119−6127. Examining the raw event list as in Woods et al. (2004a) revealed an instrumental timing anomaly that resulted in time tags being shifted forward by 1 s for events detected after the anomaly took place. We corrected for this by subtracting 1 s from the original time stamps and from the auxiliary PN file (*AUX.FIT) containing the clock information for the observation. The corrected data set was then converted to the solar system barycenter.

A circular region of 25″ radius was used to extract the pulsar events. The data were divided into different energy ranges: 0.5–10.0 keV (620±30 counts), 0.5–2.0 keV (340±25 counts) and 2.0–10.0 keV (275±22 counts)[1] . From an updated radio ephemeris obtained from regular monitoring at the Parkes radio telescope, the predicted barycentric radio period for the middle of our observation (MJD 52816.54) was 2.44972914 Hz. The Z_n^2 test (Buccheri et al., 1983) with harmonics $n = \{1,2,4,8\}$ was used to search for pulsations. The most significant signal was detected in the 0.5–2.0 keV range with $Z_2^2 = 52.8$ (6.6σ significance) at a frequency of 2.449726(6) Hz (1σ errors). This frequency is in agreement with the radio prediction for PSR J1119−6127. In the 2.0–10.0 keV range, no signal was found with a significance $>2.8\sigma$. In the 0.5–10.0 keV range, the above signal was detected with a 5.2σ significance.

Figure 4.3 shows the resulting pulse profiles at 0.5–2.0 keV (top) and 2.0–10.0 keV (bottom). The background was estimated from a nearby region away from bright SNR knots. The horizontal dashed lines represent our estimates for the contribution from the pulsar's surroundings (see §4.5.1). The resulting pulsed fraction [PF $\equiv (F_{max}–F_{min})/(F_{max}+F_{min})$, called 'peak-to-peak'] is labeled in Figure 4.3 (1σ statistical errors). Estimating the pulse fraction by summing the number of counts above the DC level and dividing by the total number of counts (also called the 'area' pulsed

[1] Background-subtracted counts using background regions away from the source and minimal contamination from the supernova remnant.

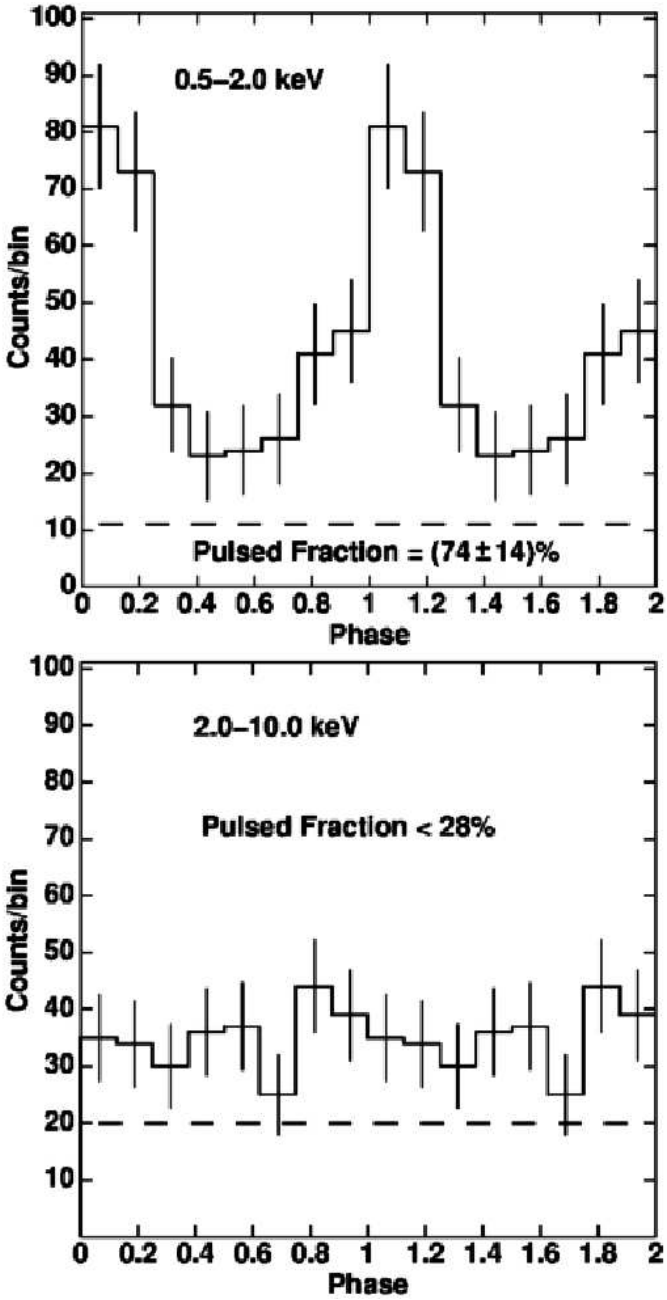

Figure 4.3: X-ray pulse profiles of PSR J1119−6127 in the 0.5–2.0 keV (*top*) and 2.0–10.0 keV (*bottom*) ranges. Errors bars are 1σ and two cycles are shown. The peak of the radio pulse is at phase 0. The dashed lines represent our estimates for the contribution from the surrounding PWN and supernova remnant (see §4.5.1).

fraction, see §5.3.2 for details) produces a value of 64±13%. In the 2.0–10.0 keV range, we derive an upper limit for the pulsed fraction of 28% (at the 99% confidence level). For this, we used the maximum power obtained from a Fourier analysis of the data for a small range of frequencies centred on the radio prediction (within our errors) and assumed a worst-case sinusoidal profile. An upper limit for the pulse amplitude can then be derived by calculating an upper limit on the power that could still be present above the observed maximum at a specific level of confidence. For a detailed description of this method we refer to Vaughan et al. (1994), and e.g., Ransom et al. (2002).

The pulse profile in the 0.5–2.0 keV range shows a single, narrow pulse with a high peak-to-peak PF = (74±14)%. We then modeled the profile with a 1-D gaussian using *Sherpa* (v.3.2.0). The best-fit value for the full-width at half maximum was $0.26^{+0.08}_{-0.06}P$ (1σ errors) with χ^2(dof) = 2.1(4). A sinusoidal model resulted in χ^2(dof) = 8.9(5). Due to the limited statistics available, the gaussian fit is preferred only at the 97.7% level (according to the F-test). Additional X-ray observations at higher resolution are needed to further constrain the pulse shape.

Correlating the times of arrival for the radio pulse at 1.4 GHz with the X-ray pulse, we find that the radio peak arrives 26 ms before the centre of the X-ray peak (with ≈3 ms uncertainty). This corresponds to phase 0 in the pulse profiles of Figure 4.3 and suggests that the radio peak is in phase with the X-ray peak, or possibly just slightly ahead, given the low temporal resolution of the *XMM–Newton* observation (phase bin width of 51 ms). In addition, although it is unlikely that the EPIC-PN timing anomaly present during the observation affected the absolute timing (*XMM–Newton* HelpDesk, private communication), we regard this result with caution until it can be confirmed with additional observations.

4.4 Spectral Analysis

The EPIC data were used to perform a spectral analysis of PSR J1119−6127. Circular regions with radii of 20″ and 25″ were used for MOS and PN, encompassing

≈75% and ≈78% of the source photons, respectively. The derived fluxes have been corrected accordingly. Background regions were chosen from nearby areas away from bright SNR knots. The spectra were fit in the 0.5–10.0 keV range using XSPEC (v.11.3.0) with a minimum of 20 counts per bin from a total of 240±19, 210±18, and 620±30 background-subtracted counts in MOS1, MOS2 and PN, respectively.

4.4.1 Phase-Averaged Spectroscopy

One-component models were first fit to the phase-averaged MOS and PN data. A power-law model provided a better fit than a thermal blackbody model (BB), giving $\chi^2(\mathrm{dof}) = 113(68)$ and $\chi^2(\mathrm{dof}) = 180(68)$, respectively. However, it was evident from the fit residuals and the improvement in χ^2 that two-component models were needed in order to describe the low and high energy portions of the spectra. The derived fits from two-component models are summarized in Table 4.1 and Figure 4.4 (top) shows the best-fit BB+PL model using the PN spectrum. In these fits, a non-thermal power-law component with photon index $\Gamma \sim 1.5$ described the high-energy emission in the spectra well. In turn, various models were used to describe the low-energy emission. A magnetized hydrogen atmosphere model (NSA; Zavlin et al., 1996) required a small distance of $\lesssim 2$ kpc to account for the observed emission (or conversely an implausibly large emitting radius of 27^{+4}_{-2} km at 8.4 kpc, 1σ range). Such a small distance can be ruled out from HI absorption measurements (Caswell et al., 2004). Currently available (non-magnetic) atmosphere models of higher metallicity (e.g., solar abundances, pure iron; Gänsicke et al., 2002) were also used and found to produce poor fits to the observed emission. At a fixed distance of 8.4 kpc, the derived temperatures were ≈1.9 MK [χ^2(dof)=85(67)] and <1.2 MK [χ^2(dof)=114(67)] for solar and pure iron compositions, respectively. However, when the distance was allowed to vary, the models converged to unrealistic values (e.g., <200 pc for temperatures <1.4 MK) with no improvement on the resulting χ^2.

Table 4.1: Fits to the *XMM–Newton* phase-averaged spectrum of PSR J1119−6127

Parameter	PL+PL ($\pm1\sigma$)	BB+PL ($\pm1\sigma$)	NSA[a]+PL ($\pm1\sigma$)
N_H (10^{22} cm^{-2})	$2.3^{+0.4}_{-0.3}$	$1.6^{+0.4}_{-0.3}$	$1.9^{+0.5}_{-0.3}$
χ^2(dof)	79(66)	78(66)	78(66)
	Soft component characteristics		
Γ or T^∞	6.5±0.9	$2.4^{+0.3}_{-0.2}$ MK	0.9±0.2 MK
R^∞ (km)	...	$3.4^{+1.8}_{-0.3}$	12 (fixed)
d (kpc)	8.4 (fixed)	8.4 (fixed)	$1.6^{+0.2}_{-0.9}$
${f_{abs}}^b$ (10^{-14})	$2.1^{+2.3}_{-0.9}$	$1.5^{+1.8}_{-0.2}$	$1.7^{+7.0}_{-0.4}$
${f_{unabs}}^b$ (10^{-13})	63^{+57}_{-32}	$2.4^{+3.0}_{-0.5}$	$7.2^{+31}_{-1.6}$
${L_X}^b$ (10^{33})	53^{+50}_{-27}	$2.0^{+2.5}_{-0.4}$	$0.22^{+0.88}_{-0.05}$
	Hard component characteristics		
Γ	$1.3^{+0.5}_{-0.2}$	$1.5^{+0.3}_{-0.2}$	$1.5^{+0.2}_{-0.3}$
${f_{abs}}^b$ (10^{-14})	$7.1^{+10}_{-1.5}$	$7.4^{+3.6}_{-1.0}$	$7.3^{+4.7}_{-2.7}$
${f_{unabs}}^b$ (10^{-13})	$1.0^{+1.6}_{-0.2}$	$1.1^{+0.6}_{-0.2}$	$1.1^{+0.8}_{-0.3}$
${L_X}^b$ (10^{33})	$0.8^{+1.3}_{-0.2}$	$0.9^{+0.5}_{-0.1}$	0.04±0.02

[a] The atmospheric model was computed with B=10^{13} G and pure hydrogen composition. The local values for the temperature, T, and radius, R = 10 km, of the star have been redshifted to infinity according to the formulae T^∞=T(1–$2GM/Rc^2$)$^{1/2}$ and R^∞=R(1–$2GM/Rc^2$)$^{-1/2}$, with M = 1.4 $M_\odot$.

[b] The 0.5–10.0 keV absorbed and unabsorbed fluxes, f_{abs} and f_{unabs}, have units of ergs s^{-1} cm^{-2}. The 0.5–10.0 keV X-ray luminosity, L_X, at the distance d, is in units of ergs s^{-1}.

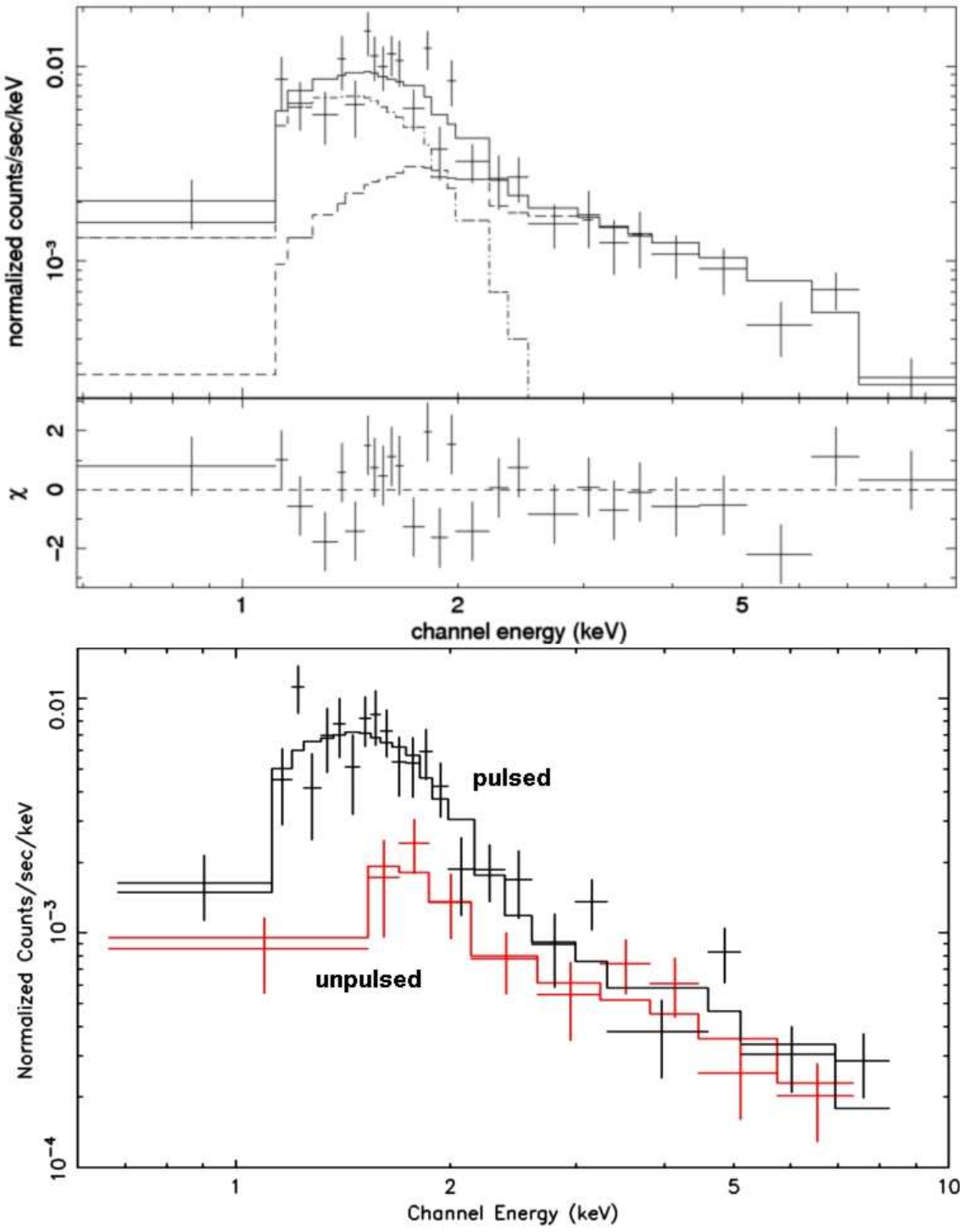

Figure 4.4: *Top*: Phase-averaged PN spectra showing individual spectral components (blackbody dominating at small energies). *Bottom*: PN spectra obtained for the pulsed (*black*, phases 0.7–1.3) and unpulsed (*red*, 0.3–0.7) regions of the pulse profile with their respective best-fit blackbody plus power-law model (solid curves).

4.4.2 Phase-Resolved Spectroscopy

We also extracted PN spectra from the "pulsed" and "unpulsed" regions of the pulse profile, at phases 0.7–1.3 (430±28 counts) and 0.3–0.7 (200±20 counts), respectively. These spectra are shown in Figure 4.4 (bottom) and were well fit by two-component models that agree with those derived for the phase-averaged spectra. For example, a blackbody plus power-law model yielded $T^{\infty} = 2.8 \pm 0.4$ MK and $\Gamma = 1.4^{+0.5}_{-0.2}$ (1σ errors). The main difference between the pulsed and unpulsed spectra was found to be the relative contributions of the model components. The pulsed spectrum is dominated by the soft component below 2 keV, where it contributes ≈85% (≈90%) of the absorbed (unabsorbed) flux. In turn, the unpulsed spectrum is dominated by the hard, power-law component even below 2 keV, where it contributes ≈65% (≈55%) of the absorbed (unabsorbed) flux. For both pulsed and unpulsed spectra, the power-law component contributes >90% of the flux above 2 keV (either absorbed or unabsorbed).

4.5 Discussion

4.5.1 Emission Characteristics

The *XMM–Newton* observation of PSR J1119−6127 allowed us to detect, for the first time, X-ray pulsations from this HBRP. The pulsations are only detected in the 0.5–2.0 keV range with a single, narrow peak and a very high pulsed fraction of (74±14)%.

The emission detected within the *XMM–Newton* extraction regions is a combination of pulsar, PWN and diffuse SNR emission (see Fig. 4.2). In addition, the derived spectra from these regions are well fit by two-component models. We then argue that the hard spectral component detected arises primarily from the pulsar's surroundings and not from the NS itself. Using a high-resolution archival *Chandra* observation of the field (see Gil & Sendyk, 2003), we estimate that the PWN plus SNR emission within a 25″ radius, excluding the pulsar, is well described by a power-law model with $\Gamma = 1.8^{+0.8}_{-0.6}$ and unabsorbed flux in the 0.5–10.0 keV range of $0.9^{+0.6}_{-0.5} \times 10^{-13}$

erg s^{-1} cm^{-2} (1σ errors). These values are in good agreement with the hard, power-law component shown in Table 4.1. Although a contribution from the pulsar to this hard emission cannot be ruled out, it would not affect our results on the pulsar's soft emission.

The soft component detected with *XMM–Newton* must then arise from PSR J1119−6127, as is further supported by the pulsed emission having a distinctly soft spectrum (see §4.4.2). Such emission is unlikely to have a non-thermal origin. Non-thermal X-rays from radio pulsars have photon indices in the range $0.5<\Gamma<2.7$ (e.g., Gotthelf, 2003). Synchrotron emission models due to accelerated particles in the magnetosphere predict $\Gamma \lesssim 2$ (e.g., Cheng & Zhang, 1999; Rudak & Dyks, 1999). The soft component of the pulsed emission from PSR J1119−6127, if interpreted as non-thermal, has a steeper spectrum ($\Gamma=6.5\pm0.9$) than those observed or predicted and would imply an acceleration mechanism that cannot be achieved with current models.

The derived blackbody temperature for PSR J1119−6127 of $T_{bb}^{\infty} = 2.4^{+0.3}_{-0.2}$ MK is among the highest seen for radio pulsars. Although it is similar to those found in a few other pulsars, none of them exhibits a higher temperature at statistically significant levels (e.g, PSR J0218+4232 has a characteristic age of $\tau_c = P/2\dot{P} = 5.1\times10^8$ yr and a blackbody temperature of $T_{bb}^{\infty} = 2.9\pm0.4$ MK; Webb et al., 2004). In addition, PSR J1119−6127 is now the youngest radio pulsar from which thermal emission has been detected, the next youngest being Vela ($\tau_c = 11$ kyr) with a blackbody temperature $T_{bb}^{\infty} = 1.47\pm0.06$ MK (Pavlov et al., 2001b). For comparison, the young Crab pulsar ($\tau_c = 1.3$ kyr) and PSR J0205+6449 ($\tau_c = 5.4$ kyr, in the SNR 3C 58) have upper limits on the possible blackbody emission from their entire surface of $T_{bb}^{\infty}<1.97$ MK (Weisskopf et al., 2004) and $T_{bb}^{\infty}<1.02$ MK (Slane et al., 2004), respectively, at the 3σ confidence level.

The observed pulsed fraction for the thermal emission in PSR J1119−6127 is also higher than those of other radio pulsars. Sources for which the thermal emission arises from the entire surface or from localized regions show pulsed fractions at low energies of <42% (e.g., Pavlov et al., 2001b; Pavlov et al., 2002; Becker & Aschenbach, 2002). The narrow peak in the pulse profile also appears to differ from the broad

pulsations seen in thermal emission from radio pulsars at low energies. Although a multi-component pulse profile (e.g., sine curve plus a narrow peak) in the 0.5–2.0 keV range cannot be ruled out for PSR J1119−6127 and requires additional observations, we expect any pulse components to show a soft spectrum consistent with the 3σ values in Table 4.1 and the narrow component to exhibit a high PF $> 50\%$.

4.5.2 Thermal Emission Mechanisms

We first consider the observed characteristics in light of conventional models for NS emission. Thermal emission from polar-cap reheating, due to return currents from the "outer gap" (Cheng & Zhang, 1999) or from close to the polar cap (Harding & Muslimov, 2001b), is expected to have an X-ray luminosity of $\lesssim 10^{-5}\dot{E}$ in young sources. This is at least 2 orders of magnitude below our value for the luminosity of $0.9^{+1.1}_{-0.2}\times10^{-3}\dot{E}$ (see Table 4.1, BB+PL model). In addition, although polar-cap reheating has been proposed to explain similar characteristics to those of PSR J1119−6127 in some older pulsars ($\tau_c \gtrsim 1$ Myr, e.g., Becker & Aschenbach, 2002), such emission implies much smaller emitting areas (radius < 1 km, see e.g., Webb et al., 2004).

Thermal emission may also arise from the entire surface of the NS due to initial cooling. While the observed blackbody luminosity is in line with predictions from cooling models, the observed blackbody temperature is somewhat higher than predicted ($\lesssim$1.8 MK, e.g., Yakovlev et al., 2004) and the blackbody radius of $R^{\infty}_{bb} = 3.4^{+4.3}_{-0.9}\ d_{8.4}$ km (3σ errors) is smaller than allowed from NS equations of state ($R^{\infty}\gtrsim$12 km, Lattimer & Prakash, 2000). The surface temperature can be made more consistent with those expected from initial cooling if a hydrogen atmosphere model is used (see Table 4.1, and e.g., Pavlov et al., 2002). However, it has been proposed that hydrogen cannot be maintained long-term ($\sim$yrs) in atmospheres of NSs having magnetic fields as high as that of PSR J1119−6127 due to diffusive nuclear burning, with only heavier elements surviving long-term (most likely iron, Chang et al., 2004). In turn, various mechanisms have been proposed to maintain or replenish hydrogen

atmospheres on the surface of high magnetic field neutron stars (e.g., Ho et al., 2007). Regardless of this, atmospheric models result in high χ^2 values and/or problematic estimates for the distance/emitting area (see §4.4).

If the thermal emission originates from the entire surface due to initial cooling, the pulse profile and pulsed fraction in particular are problematic, as low amplitude, broad, sinusoidal profiles are expected (e.g., Becker & Aschenbach, 2002; Pavlov et al., 2002). On the other hand, recent work on surface emission from highly magnetized neutron stars has explored the effects of a high magnetic field, as heat conductivity is expected to be suppressed perpendicular to the field lines and will be larger along the lines instead (Geppert et al., 2006; Pérez-Azorín et al., 2006). This will produce a highly anisotropic temperature distribution on the surface of the star (especially if a strong toroidal field is present), with small, hot regions at the magnetic poles. Highly modulated thermal emission with high temperatures will then be produced. These results have been applied to model the observed emission from RXJ 0720.4–3125, a highly magnetized neutron star, with apparent success (Perez-Azorin et al., 2006). Pulsed fractions as high as ∼30% in the case of isotropic blackbody emission have been reported (Geppert et al., 2006). Therefore, it remains to be shown whether the same models can be applied to reproduce the observed emission characteristics in PSR J1119−6127. In this case, PSR J1119−6127 would be the first radio pulsar to show the effects of a high magnetic field on its X-ray emission.

We also point out the thermal emission with high temperature (0.46±0.04 keV) and high pulsed fraction (∼80%) that was found for PSR J1852+0040 (Halpern et al., 2007). Although a detailed timing solution has not been reported, initial estimates suggest a characteristic age of $\tau_c > 8$ Myr and low magnetic field of $B < 1.5\times10^{11}$ G. In this case, accretion onto a polar cap is likely to produce the observed emission rather than magnetic field effects.

4.5.3 High Magnetic Field Radio Pulsars

Many radio pulsars having inferred magnetic fields in the range 10^{13-14} G have now been discovered. A sample of these pulsars with associated X-ray observations is shown in Table 4.2. Most of these sources have proved to be very faint in X-rays. Only two pulsars, PSRs J1846–0258 and B1509–58, are bright non-thermal sources and power bright PWNe. As expected, and in agreement with normal radio pulsars, they are young and very energetic ($\tau_c < 2{,}000$ yrs and $\dot{E} > 10^{36}$ ergs s^{-1}).

On the other hand, the older and less energetic pulsars in Table 4.2 have not been detected in X-rays ($\tau_c > 10{,}000$ yrs and $\dot{E} < 10^{33}$ ergs s^{-1}). This includes PSR J1847–0130, the radio pulsar with highest inferred magnetic field discovered to date (0.9×10^{14} G). These pulsars show no enhancement of high-energy emission despite having inferred magnetic fields in the magnetar range. One intermediate case is that of PSR J1718–3718, which does have a faint X-ray counterpart seen with *Chandra*. However, the detailed characteristics of this emission (e.g., thermal vs. non-thermal) could not be constrained with the data.

PSR J1119−6127 is then an interesting and puzzling source. Despite being young and energetic, it does not power a bright PWN and we have found its emission to be dominated by a thermal component. This is in direct contrast to the sources mentioned above, particularly PSR J1846–0258 with which PSR J1119−6127 shares almost identical spin characteristics and even similar surroundings in their respective SNRs (Helfand et al., 2003; Gonzalez & Safi-Harb, 2005). It is therefore unclear what the physical reasons are behind their vastly different X-ray emission. In addition, while it is possible that the characteristics observed in PSR J1119−6127 may be due to heat conductivity effects on a highly magnetized atmosphere, the emission is not magnetar-like.

4.5.4 Implications for Magnetar Theories

The fact that, to date, no HBRP has shown definite signs of magnetar-like emission despite the overlapping range of estimated fields poses a key question to our

Table 4.2: Available X-ray Properties of High-Magnetic Field Radio Pulsars

PSR	J1847–0130	J1718–3718	J1814–1744	J1846–0258	B0154+61	B1509–58
P (sec)	6.7	3.4	4	0.32	2.35	0.15
B (10^{13} G)	9.4	7.4	5.5	4.8	2.1	1.5
τ_c (kyr)	83	34	85	0.72	197	1.7
$\dot{E}$ (ergs s^{-1})	1.7×10^{32}	1.5×10^{33}	4.7×10^{32}	8×10^{36}	5.7×10^{32}	1.8×10^{37}
D (kpc)	$\sim$8	4–5	$\sim$10	$\sim$19	$\sim$1.7	$\sim$5
L_X[a] (ergs s^{-1})	$<5\times10^{33}$	$\sim10^{30}$	$<6\times10^{35}$	6.4×10^{34}	$<1.4\times10^{32}$	2.4×10^{34}
T or Γ	–	$T\sim$1.6 MK	–	$\Gamma\approx$1.4	–	$\Gamma\approx$1.4
Ref.	McLaughlin et al. (2003)	Kaspi & McLaughlin (2005)	Pivovaroff et al. (2000)	Helfand et al. (2003)	Gonzalez et al. (2004)	Gaensler et al. (2002)

[a] Unabsorbed luminosities in the 0.5–10 keV range (except for PSR J1814–1744, which is in the 2–10 keV range).

understanding of all of these sources. Many scenarios and theories has been proposed that deal with this issue. Observationally, Kaspi & McLaughlin (2005) pointed out that the luminosity of PSR J1718–3718, and other HBRPs, is comparable to those seen in some AXPs in quiescence (e.g., XTE 1810–197 Gotthelf & Halpern, 2007). In this case, the detection of magnetar-like bursts from these radio pulsars would then confirm the expected effect of their high magnetic fields[2]. It is also possible that the discrepancies between these populations represent the prime examples of the inadequacy of the magnetic dipole formula to estimate the true fields of neutron stars to within a factor of a few.

Pons et al. (2007) have proposed that the thermal emission observed from all neutron stars with large magnetic fields has a contribution from magnetic field decay (even in the absence of magnetic-driven bursts). They estimate that for stars with fields $\gtrsim 10^{13}$ G the thermal evolution will be largely determined by the evolution of the magnetic field. However, in the youngest objects (such as PSR J1119−6127) it is not possible to differentiate between cooling and field decay contributions to the observed thermal emission.

Pons & Geppert (2007) have modeled the dissipation of magnetic fields inside neutron stars and suggested an evolutionary connection between magnetars and old, thermally-emitting isolated neutron stars (such as RX J0720.4–3125 and RX J1308.6+2127, which have inferred magnetic fields of $\approx$few$\times 10^{13}$ G, ages of a few Myrs and spin-down luminosities of $\approx 10^{30}$ ergs s^{-1}; Kaplan & van Kerkwijk, 2005; Kaplan & van Kerkwijk, 2005). For example, the X-ray emission from RX J0720.4–3125 has a luminosity of $\approx 10^{32}$ ergs s^{-1} and blackbody temperature of $\approx$0.082 keV, larger than predicted by cooling models and arguing for an additional source of heating with magnetic field decay being an attractive possibility (Pons & Geppert, 2007). Interestingly, these sources have inferred properties similar to those of PSR B0154+61, which

[2] However, we note that transient magnetars have only been seen to have detectable radio emission after bursts, when their X-ray emission is higher than in quiescence.

we have showed not to have enhanced X-ray emission down to a similar temperature and luminosity (see Chapter 3).

Bhattacharya & Soni (2007) have also suggested an evolutionary connection between HBRPs and magnetars. They argue that a strongly magnetized core is created when the NS is born that is at first screened by the conducting exterior. As the exterior relaxes with time this eventually leads to the onset of magnetic activity. In this case, young, HBRPs (such as PSR J1119−6127) will then transition to a magnetar phase with time. Bhattacharya & Soni (2007) also predict an evolutionary connection from AXP-like to SGR-like behavior, the latter being the final stage before the star suddenly turns off its active phase once all the screening currents are dissipated and the field reaches a steady state.

In turn, Geppert & Rheinhardt (2006) have suggested that both magnetars and HBRPs have the same formation mechanism as follows: neutron stars with high initial fields ($\gtrsim 10^{15}$ G, produced by any possible mechanism) can either keep such high fields or evolve into conventional radio pulsars with fields of 10^{12-13} G. The authors propose that stars with initial periods of $P_0 \gtrsim 6$ ms and/or magnetic inclination angles of $\alpha \gtrsim 45^\circ$ (the angle between the magnetic and spin axes) will transfer their magnetic energy into magnetic and kinetic energy of small-scale fields, which are then dissipated. On the other hand, stars with high initial fields, small initial periods ($P_0 \lesssim 6$ ms) and small magnetic inclination angles ($\alpha \lesssim 45^\circ$, will keep their high fields and appear as magnetars or HBRPs. Geppert & Rheinhardt (2006) cite a value of $\alpha = 19^\circ$ for PSR J1119−6127 (from Harding et al., 2003; Harding, 2006), while recent radio observations of XTE 1810–197 list values of $\alpha = 4^\circ$, 6° , 44° , 70° (Camilo et al., 2007b; Kramer et al., 2007).

Recently, Lai et al. (2007, in preparation) have argued that the formation of a condensed phase on the surface of neutron stars with large magnetic fields and (relatively) small temperatures can be responsible for the presence of radio emission in HBRPs. In this case, the high cohesive energy of a condensed phase (the energy required to pull an atom out of the bulk matter) is large enough so that the surface does not efficiently supply charges to the magnetosphere. In this case, the electric

field is not screened, a polar gap is created and particle acceleration can occur. On the other hand, the large temperatures and high magnetic fields of magnetars do not form condensed surfaces. Here, the large amount of vapour on the surface supplies sufficience charges to screen the accelerating field and stops the production of radio emission.

4.6 Summary

The *XMM–Newton* observation of PSR J1119−6127 shown here allowed for the discovery of highly pulsed thermal emission from this young HBRP. The detailed characteristics of this emission place important constrains on current models of the emission from the surfaces of neutron stars. In addition, the fact that no clear magnetar-like characteristics has been found for this and other HBRPs has important consequences for our understanding of NS evolution and emission processes as a whole.

In the next chapter we turn our attention to the emission characteristics of a well-established magnetar, the AXP 4U 0142+61.

Chapter 5

Long-term changes in the X-ray emission of the AXP 4U 0142+61

This chapter presents the results from observations of the AXP 4U 0142+61 taken between 2000–2007 using *XMM–Newton*, *Chandra* and *Swift*. The data show that an evolution of almost all emission characteristics is present throughout this time, from pulse profile changes to total observed flux. These changes are present at a low level (<50%) and only became evident thanks to the high quality of the data available. These observations allowed us to test predictions made by the magnetar model for the behavior of these sources: the largest changes are observed to be correlated with the recent burst activity of the source in 2006–2007, as predicted by these models, and appear to be mainly magnetospheric in nature. However, the details of the changes observed throughout the 7 years of observations suggest that multiple emission mechanisms are likely present in this source.

These results have been submitted for publication as: *Gonzalez, M. E.*, Dib, R., Kaspi, V. M., Woods, P. M., Tam, C. R., & Gavriil, F. P., *Long-term changes in the X-ray emission from the Anomalous X-ray Pulsar 4U 0142+61*, Astrophysical Journal, submitted, 2007 (http://arxiv.org/abs/0708.2756)

5.1 Introduction

Recent observations of neutron stars have uncovered the wide variety of observational manifestations they appear to have, from rotation-powered pulsars and isolated thermally cooling objects to the magnetars (see Kaspi et al., 2006, for a review). Magnetars exhibit long spin periods of several seconds, have persistent X-ray luminosities of $\sim 10^{34-36}$ ergs s^{-1} and have estimated surface dipolar magnetic fields of $0.6-7\times10^{14}$ G. Optical and infrared (IR) counterparts have been found for many of these objects (e.g., Hulleman et al., 2001; Israel et al., 2003). Despite their soft spectrum at low X-ray energies, they have also been shown to produce copious amounts of hard X-ray emission above up to 300 keV (e.g., Molkov et al., 2004; Kuiper et al., 2006).

Magnetars are thought to be neutron stars whose X-ray emission is powered by the decay of an ultra-high magnetic field (see §1.7). The sudden bursts of high-energy emission seen from some of these sources are believed to be powered by the rearrangement of their magnetic field, while the nature of the optical/IR emission in this model is currently under study (Beloborodov & Thompson, 2007). On the other hand, the active fallback disk model argues that the persistent emission at low X-ray energies arises from accretion onto the neutron star, while the optical/IR emission is thought to originate from the disk itself (e.g., Chatterjee et al., 2000; Alpar, 2001). If only a passive (i.e. non-accreting) disk is present, it could be responsible for part of the emission at optical/IR wavelengths (Wang et al., 2006). However, a magnetar origin for the high-energy bursts is still needed in all disk models, as well as a magnetospheric origin for any pulsed emission at optical/IR wavelengths. The large variety of unusual physical phenomena that high magnetic fields can power makes magnetars interesting objects to study.

4U 0142+61 is the brightest of all known AXPs. It has a period $P = 8.7$ s, period derivative $\dot{P} = 0.2\times10^{-11}$, inferred surface dipolar magnetic field strength of $B = 1.3\times10^{14}$ G, and has been detected from the mid-IR to hard X-rays (Israel et al., 1994; Gavriil & Kaspi, 2002; den Hartog et al., 2007). In the mid-IR, Wang et al. (2006) have found evidence for a passive disk. The optical emission was found to be pulsed with a peak-to-peak pulsed fraction of ≈29% (Kern & Martin, 2002; Dhillon

et al., 2005). Durant & van Kerkwijk (2006a) have derived a distance to the source of 3.8±0.4 kpc using extinction estimates from high-resolution X-ray spectroscopy compared to those of nearby stars in the field. In addition, 4U 0142+61 has a soft X-ray spectrum that has been fitted traditionally with a blackbody plus power-law model with temperature $kT \approx 0.4$ keV (≈ 4.6 MK) and photon index $\Gamma \approx 3.3$ (e.g., Juett et al. 2002; Patel et al. 2003). However, the extrapolation of this soft X-ray model to the optical/IR overpredicts the observed emission if associated with the power-law component, while it underpredicts this emission if it is associated with the blackbody component.

A long-term monitoring campaign for 4U 0142+61 has been carried out with the *Rossi X-ray Timing Explorer* (*RXTE*) for the past 10 yrs. Using these data, Dib et al. (2007) reported a slow evolution of the pulse profile between 2000 and 2006, as well as a slow increase in the pulsed flux between 2002 and 2006. These changes may be associated with a possible glitch, or another event, that may have occurred between 1998–2000. Given the low amplitude of the reported variations, the main goal of this work was to confirm their presence with a different instrument. In addition, the source appears to have entered an active phase showing three X-ray bursts in 2006 April–June and 2007 February (Kaspi et al., 2006; Dib et al., 2006; Gavriil et al., 2007a,b) which were followed up by various telescopes. The last observed burst is the longest and among the most energetic seen from AXPs to date (Gavriil et al., 2007b).

Constraining the long-term evolution of the emission from 4U 0142+61 is important for quantifying all AXP variability phenomena, in the hope of discovering correlations that can be checked against models, or uncovering phenomena common to all AXPs. Here we present results from observations of this source performed with *XMM–Newton*, *Chandra* and *Swift*, extending from 2000–2007. Indeed, long-term trends in the spectral and pulse characteristics are found, confirming the *RXTE* results, as well as changes coincident with the recent phase of burst activity. Observations in the near-IR after two of these bursts are also presented. We find that the overall evolution characteristics support a magnetar origin, while the detailed changes suggest that multiple emission mechanisms are likely present. The combined effect of

these mechanisms is yet to be explored in current modeling of these sources.

5.2 X-ray Observations

5.2.1 *XMM–Newton*

4U 0142+61 was observed seven times with *XMM–Newton* between 2002 and early 2007. The details of the observations are summarized in Table 5.1. We concentrated on data from the EPIC PN instrument as it provided the best combination of longest time baseline and highest number of counts, in order to study the long-term evolution of the source with high precision. Observations taken in "timing" mode are performed in such a way that the central 64×200 pixels at the focal plane are collapsed into a one-dimensional row to be readout at high speed.

All *XMM–Newton* observations were reduced and analyzed with the latest calibration files available as of 2007 March. Periods of high particle background were excluded in the analysis and standard reduction techniques applied. The PN observations performed in the imaging small-window mode had a time resolution of 6 ms, while the ones in timing mode had a resolution of 0.03 ms. For the imaging observations, a circle of 40″ radius was used to extract the source counts. For the data in timing mode, the source events were extracted from a region 20 pixels wide around the source position. Background regions were chosen from parts of the same chip away from the source. The total number of background-subtracted counts detected for each observation are shown in Table 5.1. While the *XMM–Newton* count rates in each observation are ≈45 cts s^{-1}, the fast read-out modes in which the instruments

Table 5.1: X-ray observations of 4U 0142+61

Date	MJD	CCD Mode	Effective Exp. Time	Counts[a]
XMM–Newton:				
13/02/2002	52318.3	Small-Window	2.9 ks	1.29×10^5
24/01/2003	52663.9	Small-Window	3.8 ks	1.62×10^5
01/03/2004	53065.5	Timing	29.4 ks	1.47×10^6
24/07/2004	53211.3	Timing	21.2 ks	1.07×10^6
28/07/2006	53944.8	Small-Window	3.7 ks	1.71×10^5
13/01/2007	54113.8	Small-Window	4.4 ks	1.95×10^5
10/02/2007	54141.1	Timing	8.6 ks	4.24×10^5
Chandra:				
21/05/2000	51685.8	Continuous Clocking	5.9 ks	1.23×10^5
29/05/2006	53915.4	Continuous Clocking	18.6 ks	3.86×10^5
10/02/2007	54141.3	Continuous Clocking	20.1 ks	3.99×10^5
Swift:				
13/02/2005	53414.8	Windowed-Timing	6.6 ks	2.8×10^4
10/02/2007	54141.2	Windowed-Timing	3.5 ks	1.6×10^4

[a] Net counts in the 0.5–10 keV range. Uncertainties smaller than last digit shown.

were operated prevented pileup[1] problems.

5.2.2 *Chandra*

4U 0142+61 has been observed three times with *Chandra* at sufficiently high time resolution to allow useful timing studies (see Table 5.1). The ACIS Continuous Clocking mode (CC, operated in a similar principle as the PN's timing mode) allows for 2.9 ms resolution at the expense of one dimension of spatial resolution. The effects of pileup are negligible in this mode. The data were reduced using standard techniques[2]. Source events were extracted from a region 4 pixels wide ($\approx 2''$) around the peak of the emission, with background regions taken far from the source.

5.2.3 *Swift*

4U 0142+61 has been observed numerous times with *Swift*. For the purpose of our work, we chose the X-ray Telescope (XRT) observations with the highest number of counts and sufficiently high time resolution to allow for a study of the timing properties of the pulsar (see Table 5.1). The data were reduced applying standard screening criteria. Source counts were extracted in regions 60 pixels ($\approx 2.4'$) wide around the peak of the emission, with background regions taken far from the source. We only considered events with grade 0 (i.e., events detected within a single pixel) to improve spectral resolution and used the latest redistribution matrices.

[1] Pileup arises when the count rate from the source is large enough that multiple photons can be detected in single, or adjacent, pixels before they are read out. In such a case, these multiple photons are detected as a single, higher-energy photon significantly changing the derived spectrum for the source. For the PN camera, the fast read-out modes prevent pileup issues for count rates up to $\approx$100 cts s^{-1}.

[2] http://cxc.harvard.edu/ciao/threads/aciscctoa/ and
http://wwwastro.msfc.nasa.gov/xray/ACIS/cctime

5.3 X-ray Pulse Results

5.3.1 Pulse Profiles

The *XMM–Newton*, *Chandra*, and *Swift* data were used to study the long-term evolution of the X-ray pulse profile. The data were transformed to the solar system barycenter and folded at the predicted periods for each observation using ephemerides derived from Dib et al. (2007). The data were divided into different energy ranges: 0.5–10, 0.5–2 and 2–10 keV. Sample background-subtracted, normalized pulse profiles for these bands are shown in Figure 5.1. Prior to 2006, an evolution of the pulse profile in the 2–10 keV band is clearly visible and confirms the results obtained using *RXTE* by Dib et al. (2007). In addition, the sensitivity to lower energies allows us to further constrain the evolution and conclude that it is also present in the 0.5–2 keV band.

More specifically, before 2006 we find that the relative height of the two peaks increased with time, while the depth of the dip between them became less pronounced. This caused the profiles to become more sinusoidal, as can be seen from a Fourier analysis, in which the ratio of the power in the first harmonic to the total power increased while this same ratio for the second harmonic stays fairly constant. Figure 5.2 shows these ratios for the profiles in the 2–10 keV range obtained from both *XMM–Newton* and *RXTE* (see Dib et al., 2007, for details). The ratio of power in the higher harmonics thus decreased during this time. Given that *RXTE* profiles before the bursts were derived by averaging many observations to increase the signal-to-noise ratio, the fact that a similar evolution is seen in the individual *XMM–Newton* observations confirms the long-term nature of the observed changes. The *Chandra* and *Swift* profiles (not shown in Fig. 5.2) show similar results. After the bursts were detected in 2006, the profiles fluctuate more (with more power going to higher harmonics around the time of the bursts, see also Gavriil et al., 2007b) and the overall evolution towards more sinusoidal profiles seems to have ceased.

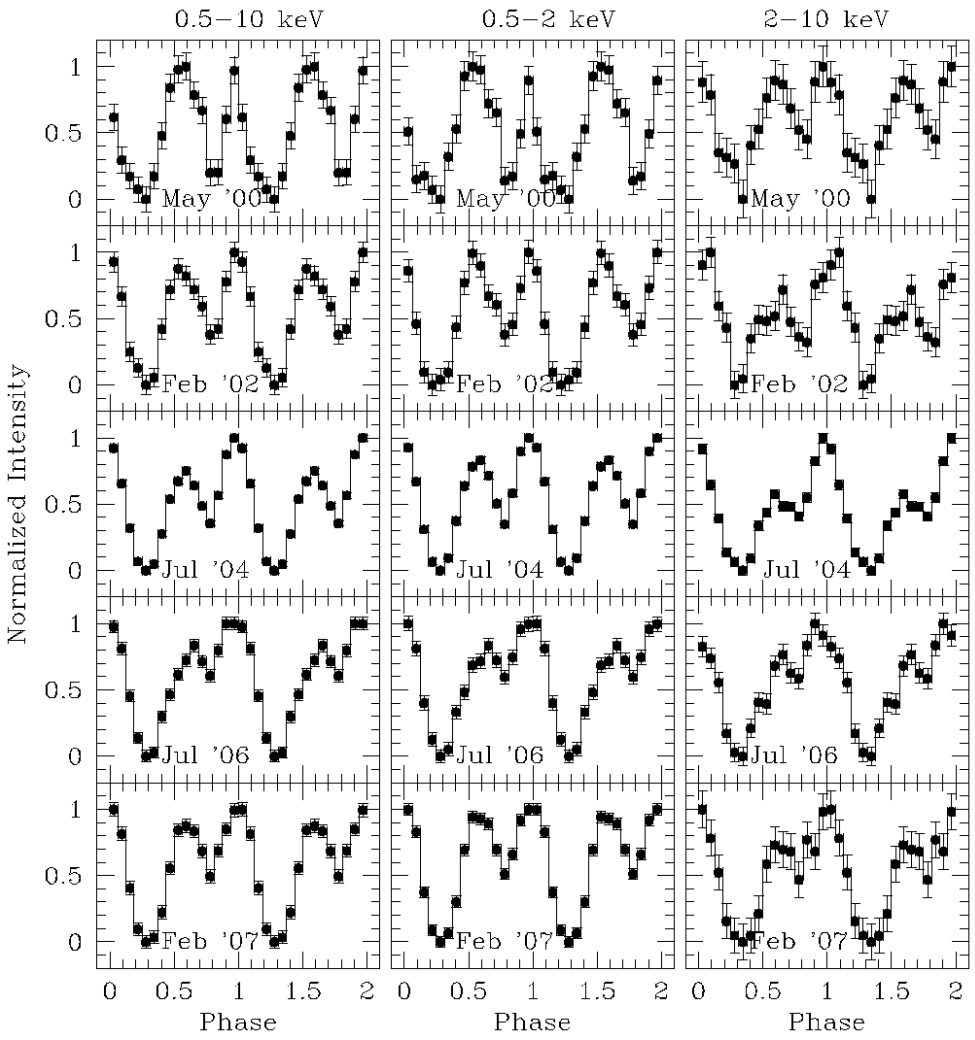

Figure 5.1: Sample pulse profiles for 4U 0142+61 in the 0.5–10 keV (*left*), 0.5–2 keV (*centre*) and 2–10 keV (*right*) ranges. The profiles have been normalized to have minimum and maximum values between 0 and 1. The top profiles (2000 May) were obtained with *Chandra*, and the rest with *XMM–Newton*. The two bottom profiles were taken after the burst activity was first detected.

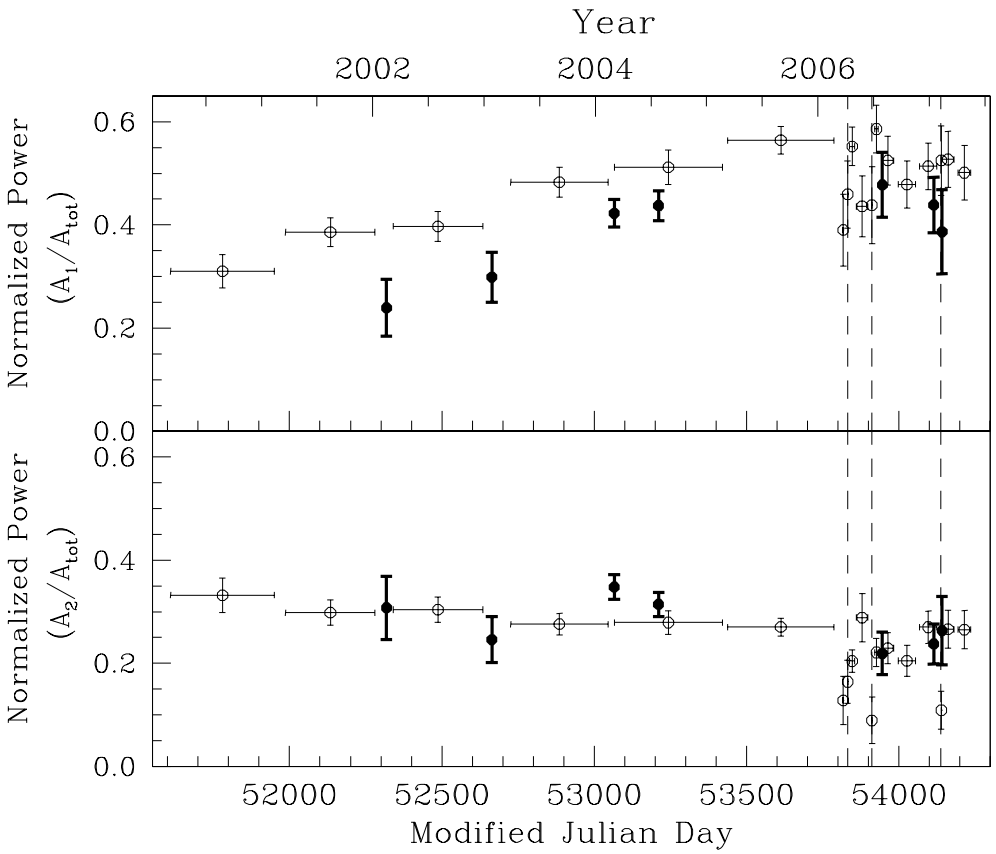

Figure 5.2: Fourier amplitudes of the pulse profiles using *XMM–Newton* (bold, solid points) and *RXTE* (simple points) in the 2–10 keV band. The pre-burst *RXTE* points are taken from Dib et al. (2007). The dashed lines indicate the three burst epochs. *Top*: Ratio of the Fourier amplitude of the fundamental to that of the power in all Fourier amplitudes. *Bottom*: Ratio of the Fourier amplitude of the second harmonic to that of the power in all Fourier amplitudes.

5.3.2 Pulsed Fractions

The fact that the pulse profile evolves with time makes it difficult to determine the pulsed fractions (and thus pulsed fluxes) of the source accurately. A few different methods are commonly used in the literature to calculate these values; each has advantages and caveats (see Archibald et al. 2007, in preparation). Here we compare the results obtained from two of these methods: the root-mean-square (RMS) and area methods.

We calculate the RMS pulsed fraction using:

$$PF_{rms} = \frac{\sqrt{2\sum_{k=1}^{n}((a_k{}^2 + b_k{}^2) - (\sigma_{a_k}{}^2 + \sigma_{b_k}{}^2))}}{a_0} \tag{5.1}$$

where a_k is the k^{th} even Fourier component defined as $a_k = \frac{1}{N}\sum_{i=1}^{N} p_i \cos(2\pi ki/N)$, $\sigma_{a_k}{}^2$ is the uncertainty of a_k, b_k is the odd k^{th} Fourier component defined as $b_k = \frac{1}{N}\sum_{i=1}^{N} p_i \sin(2\pi ki/N)$, $\sigma_{b_k}{}^2$ is the uncertainty of b_k, i refers to the phase bin, N is the total number of phase bins, p_i is the count rate in the i^{th} phase bin of the pulse profile, and n is the maximum number of Fourier harmonics to be taken into account (we have used 5 harmonics for 4U 0142+61, see also Dib et al., 2007). On the other hand, the area pulsed fraction is obtained using:

$$\frac{a_0 - \frac{p_{min}}{N}}{a_0} \tag{5.2}$$

where $a_0 = \frac{1}{N}\sum_{i=1}^{N} p_i$ and p_{min} is the average count rate in the off-pulse phase bins of the profile, determined by cross-correlating with a high signal-to-noise template, and calculated in the Fourier domain after truncating the Fourier series to 5 harmonics.

While least sensitive to noise, the RMS method returns a pulsed flux number that is affected by pulse profile changes. On the other hand, while the area method is more physically meaningful, problems in locating the true minimum and its error because of noise and binning tend to bias these values upward. Various recommendations have been made in order to derive a better estimate for the pulsed fractions for each of these methods (Archibald et al. 2007, in preparation) which we have applied here. The resulting values for all the observations of 4U 0142+61 listed in Table 5.1 are shown

in Figure 5.3. We note that the *Chandra* values appear to be consistently lower than those found using *XMM–Newton* and *Swift* and could reflect the calibration uncertainties present in these data (see below).

A significant change in the pulsed fraction over time is seen for both methods. Overall, the pulsed fraction has increased with time, reaching an apparent maximum in the observations taken after the 2006 burst activity from the source. For example, using the values from the RMS (area) method, the pulsed fraction measured with *XMM–Newton* between 2002 and 2006 has increased by 40±8% (58±12%), 28±9% (57±15%) and 35±14% (63±22%) in the 0.5–10, 0.5–2 and 2–10 keV bands, respectively. The pulsed fraction also increased significantly in the pre-burst observations (2002–2004) and between the observations taken before and after the bursts were first detected (2004–2006): in the 0.5–10 keV range, the RMS (area) increase was 23±6% (27±7%) and 14±4% (25±7%) during these time periods, respectively.

In addition, we find evidence for an increase in pulsed fraction with energy in the two longest *XMM–Newton* observations. These observations provide similar values for the pulsed fraction and in the 0.5–1, 1–6 and 6–10 keV ranges we find average RMS values of 5.1±0.3%, 6.1±0.2% and 14±2%, respectively. However, when using the area method we find values of 7.9±0.6%, 9.7±0.4% and 18±5% at 0.5–1, 1–6 and 6–10 keV, respectively. Given that the pulse profile changes significantly with energy and the area method gives less significant changes, we view this suggestive increase in pulsed fraction with energy with caution.

5.4 X-ray Spectral Results

The spectra were binned to contain a minimum of 50 counts per spectral channel and oversampling the energy resolution by a factor of 3. For the *XMM–Newton* PN data, due to the large number of counts collected from these observations, the statistical errors are very small and a systematic error of 2% was added to each spectrum (consistent with current calibration uncertainties in the PN, Kirsch et al. 2004). The phase-averaged PN spectrum for each observation was fitted in the 0.6–10 keV range

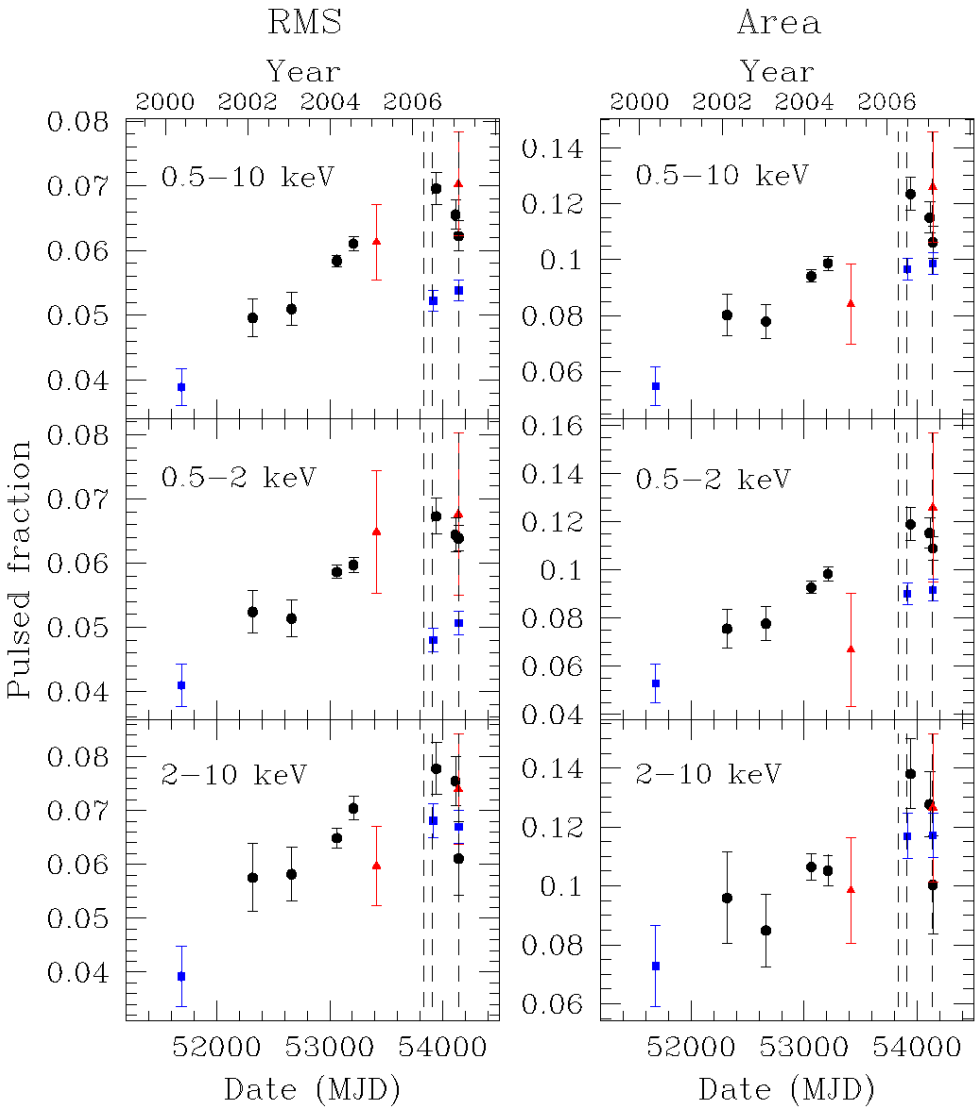

Figure 5.3: RMS (*left*) and area (*right*) pulsed fractions in the 0.5–10 keV (*top*), 0.5–2 keV (*center*) and 2–10 keV (*bottom*) ranges. Values shown correspond to those measured with *XMM–Newton* (black circles), *Chandra* (blue squares) and *Swift* (red triangles). The dashed lines indicate the three burst epochs.

using the XSPEC package v.11.3.0. Unfortunately, we cannot make use of the *Chandra* observations taken in CC mode to study the spectral characteristics of 4U 0142+61. While the *XMM–Newton* observations confirm that spectral changes are present in the source at the 10% level (as will be shown below), the CC data show variations at levels higher than this, which cannot be corrected for at present due to calibration uncertainties[3] . The lower signal-to-noise *Swift* XRT data do not contribute to constraining the evolution of the spectrum, other than to suggest that changes are present. Therefore, the *XMM–Newton* PN was used as the prime instrument to study the long term spectral evolution of 4U 0142+61. The *XMM–Newton* PN spectra were fitted simultaneously assuming a common value for the column density N_H, which was then held constant at its best-fit value. As previously reported, single-component models do not describe the emission well and we tried various multi-component models, as listed in Table 5.2 and shown in Figure 5.4. Rea et al. (2007a,b) have used various models to fit the emission from 4U 0142+61 in the 1–250 keV range. Güver et al. (2007) have also used a spectral model based on a variant of the magnetar model to fit the *XMM–Newton* data from 4U 0142+61. Our fits below are as statistically acceptable as those presented by these authors. In addition, although the main focus of this chapter is to report on the long-term evolution of the emission, we point out that the specific values for temperature, emitting area, unabsorbed flux etc. depend heavily on the model that is used to describe this emission. This dependence can be seen by comparing the parameter values shown in Table 5.2 and the unabsorbed fluxes shown in Figures 5.5 and 5.6. We will therefore concentrate on flux changes that are seen to be model-independent.

[3] See CXC Helpdesk ticket #9114

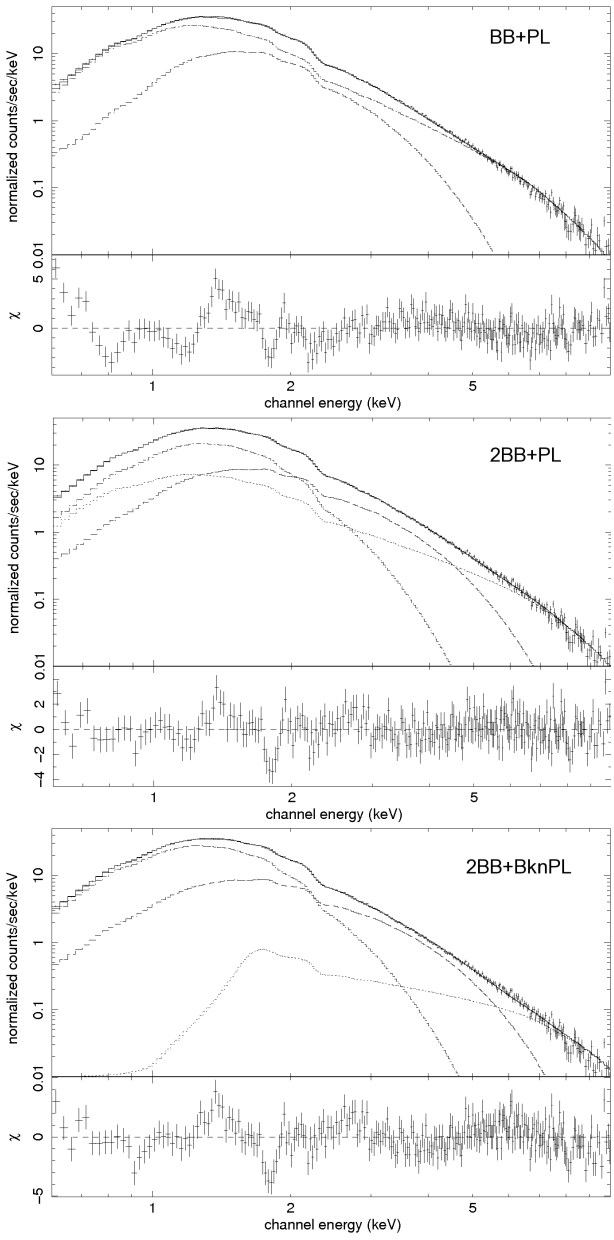

Figure 5.4: Best-fit spectral models and residuals obtained for the representative 2004 March *XMM–Newton* observation of 4U 0142+61. The models shown are BB+PL (*top*), 2BB+PL (*middle*) and 2BB+BknPL (*bottom*). See Table 5.2 for fit values and §5.4.1 for details. The individual components for each model are also shown.

5.4.1 Phase-averaged Spectrum

The traditional blackbody plus power-law model used for AXPs (BB+PL) gives results consistent with those previously reported for the source (e.g., Juett et al. 2002, Patel et al. 2003). However, the derived null probability is close to zero and many features are evident in the residuals (see Fig. 5.4). In addition, the derived value for the column density of interstellar absorption for this model is inconsistent with that estimated by Durant & van Kirkwijk (2006) based on the analysis of the high-resolution RGS spectra available from the longer *XMM–Newton* observations listed in Table 5.1 ($N_H = (6.4\pm0.7)\times10^{21}$ cm^{-2}).

A two-blackbody model does not fit the observed spectrum well. Instead, a two-blackbody plus power-law model (2BB+PL) produces the best statistical fit to the data from our sample of models. In addition, according to the magnetar model, thermal emission from the surface is expected to be scattered in the magnetosphere to produce high-energy emission only *above* the thermal peak (Thompson et al., 2002; Fernández & Thompson, 2007). To simulate this behavior, we have also fit a blackbody plus broken power-law model to the data, where the "break" energy is set to be the peak of the blackbody model. In addition, the power-law component is manually set to contribute negligible emission below this peak while having a freely-varying photon index above the peak. In this case, we find that a single blackbody model cannot reproduce the spectral shape at low energies. Adding another blackbody model significantly improves the fit (2BB+BknPL). Plots of these models to the spectrum for the 2004 March observation are shown in Figure 5.4 as an example[4] .

A summary of the range of values for all the observations obtained from these fits is shown in Table 5.2. The high quality data used here expand on what has already been pointed out by other authors: in addition to the dubious physical nature of the

[4] Due to the high statistics, the data show residuals at ≈1.8 keV that coincide with a Silicon edge in the PN effective area calibration (http://xmm.vilspa.esa.es/docs/documents/CAL-TN-0018.pdf)

Table 5.2: Summary of spectral fits to the *XMM–Newton* spectra (see §5.4 for details)

Parameter[a]	Range of values[b]
Blackbody+Power-law (BB+PL):	
N_H	$9.8(2)\times10^{21}$ cm^{-2}
kT	0.391(9)–0.44(1) keV
R (km)	5.7(7)–7.3(8) km
Γ	3.69(7)–3.771(8)
χ^2(dof)	2856(1840)
2 Blackbodies+Power-law (2BB+PL):	
N_H	$7.0(2)\times10^{21}$ cm^{-2}
kT_{cool}	0.295(9)–0.31(1) keV
R_{cool}	14(2)–16(2) km
kT_{hot}	0.53(1)–0.57(2) keV
R_{hot}	2.9(9)–3.8(6) km
Γ	2.76(9)–2.95(8)
χ^2(dof)	1993(1826)
2 Blackbodies+Broken Power-law (2BB+BknPL):	
N_H	$6.0(1)\times10^{21}$ cm^{-2}
kT_{cool}	0.27(1)–0.32(1) keV
R_{cool}	15(1.6)–19(2.5) km
kT_{hot}	0.52(3)–0.61(2) keV
R_{hot}	2.5(3)–4.4(9) km
Γ	1.42(5)–1.73(4)
χ^2(dof)	2563(1826)

[a] kT and R represent the observed blackbody temperature and radius, respectively. The temperature in MK is given by 11.6 kT_{keV} where kT_{keV} is the temperature in units of 1 keV. Γ is the power-law photon index.

[b] Errors quoted in parenthesis are 1σ confidence level. Radii calculated using a distance of 3.8±0.4 kpc. Ranges given are for the smallest and largest values of the individual parameters obtained throughout the observing campaign.

standard blackbody plus power-law model used to fit AXP spectra, the data suggest that statistically speaking, it does not reproduce the observed spectra well, at least for 4U 0142+61. While we cannot claim that the models presented here are better physical representations of the observed emission than those presented by, e.g., Güver et al. (2007), they describe the observed spectral shape better than a BB+PL and produce reasonable spectral parameters. While the range of temperature and emission area values are consistent with emission from the surface of a neutron star, our fits suggest that a single-temperature blackbody is not sufficient to describe the observed thermal emission. A number of physical interpretations can be responsible for this, such as the presence of back-flowing currents from the magnetosphere heating up the polar caps (e.g., Thompson et al., 2002), deviations from a blackbody spectrum produced by the presence of an atmosphere (e.g., Güver et al., 2007), or large temperature gradients on the surface due to anisotropic heat transport in the presence of a large magnetic field (e.g., Geppert et al., 2006).

Independent of the model used to fit the data, we find significant changes in the spectral characteristics of 4U 0142+61 during the span of the observations. Figure 5.5 shows the absorbed and unabsorbed fluxes, as well as the hardness of the spectrum, derived using the BB+PL fit. The hardness is calculated using $(H - S)/(H + S)$, where S is the flux in the 0.5–2 keV range and H is the flux in the 2–10 keV range. The values for the unabsorbed flux as given by the 2BB+PL and 2BB+BknPL fit are shown in Figure 5.6. Overall, before the recent burst activity, the total flux was fairly constant, with a possible decrease in flux being present and accompanied by an overall softening. After the 2006 burst activity, this trend reversed and we find that the 0.5–10 keV flux increased by (10±3)%. The increase in flux is also energy dependent, with the 0.5–2 and 2–10 keV ranges showing increases of (7±3)% and (15±3)%, respectively. In addition, the spectra for the two observations carried out close to burst epochs show evidence of hardening, while the one in between shows a softer spectrum. These results are independent of the spectral model used to fit the data.

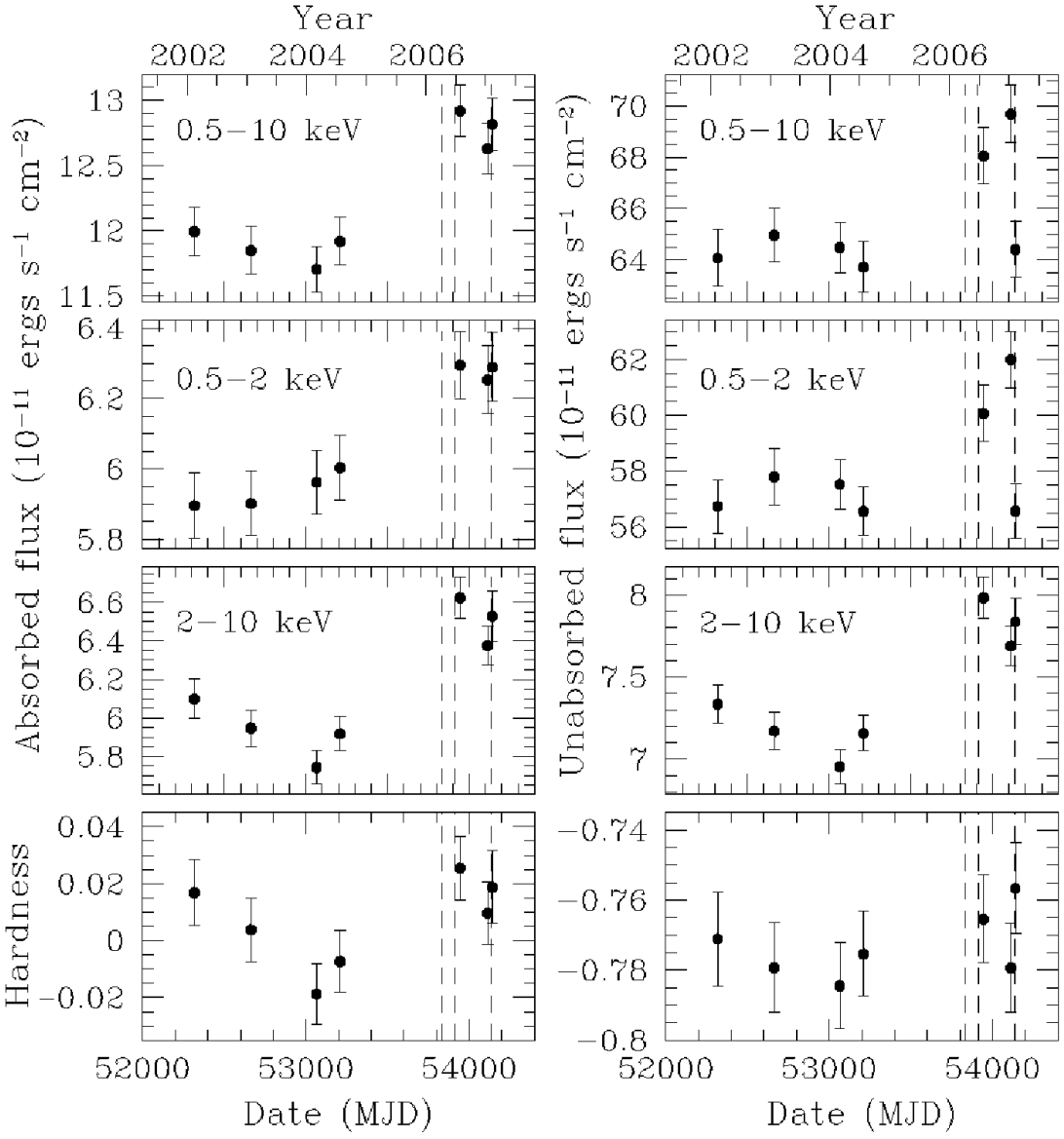

Figure 5.5: Phase-averaged fluxes and hardness ratios derived for the BB+PL model. Absorbed (*left*) and unabsorbed (*right*) values are shown. The hardness is defined as $(H - S)/(H + S)$, where S is the flux in the 0.5–2 keV range and H is the flux in the 2–10 keV range. The dashed lines indicate the three burst epochs. The increase in flux after the onset of burst activity and changes in the hardness throughout the observations are clearly visible.

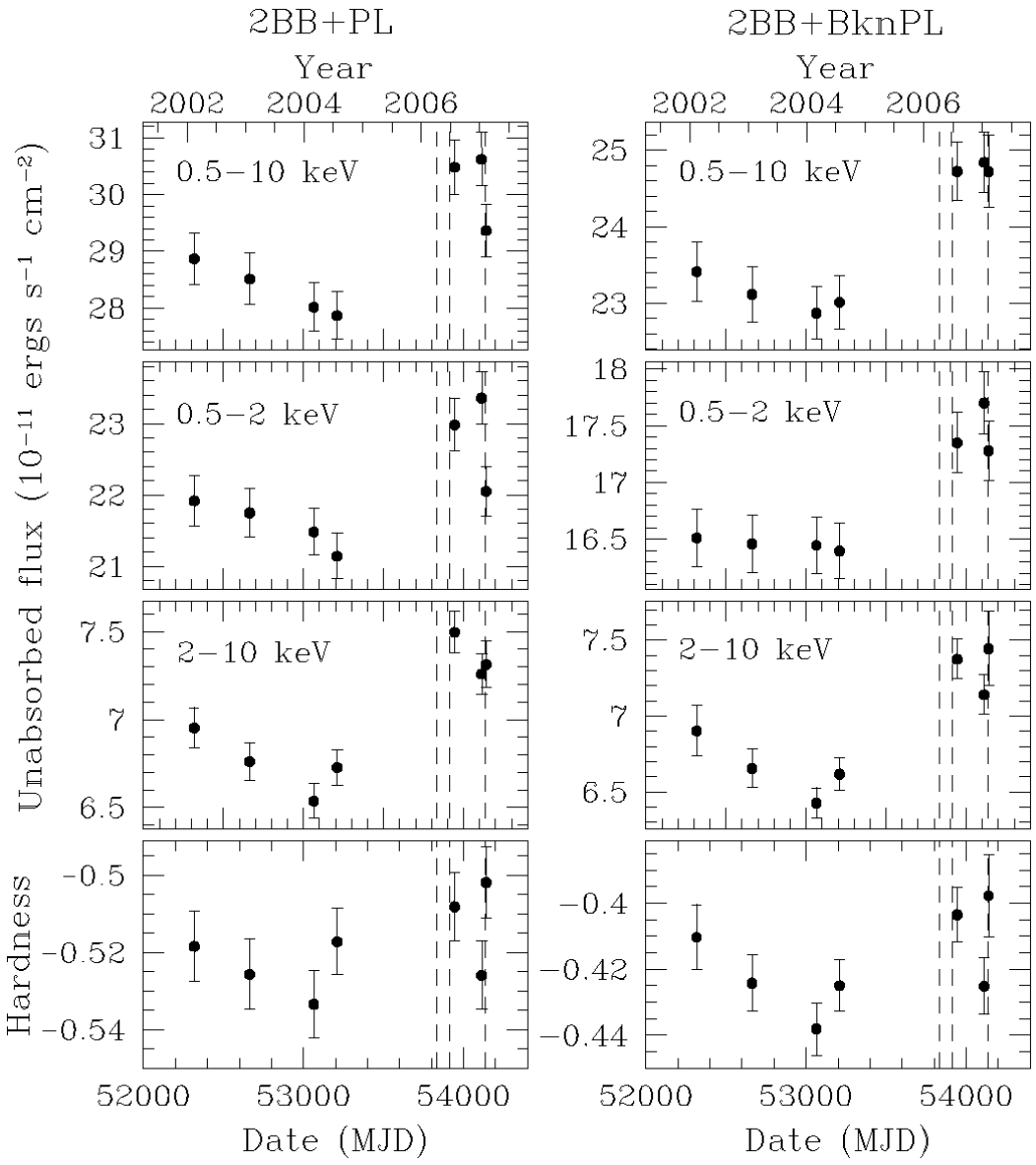

Figure 5.6: Phase-averaged unabsorbed fluxes and hardness ratios derived for the 2BB+PL (*left*) and 2BB+BknPL (*right*) model. The dashed lines indicate the three burst epochs.

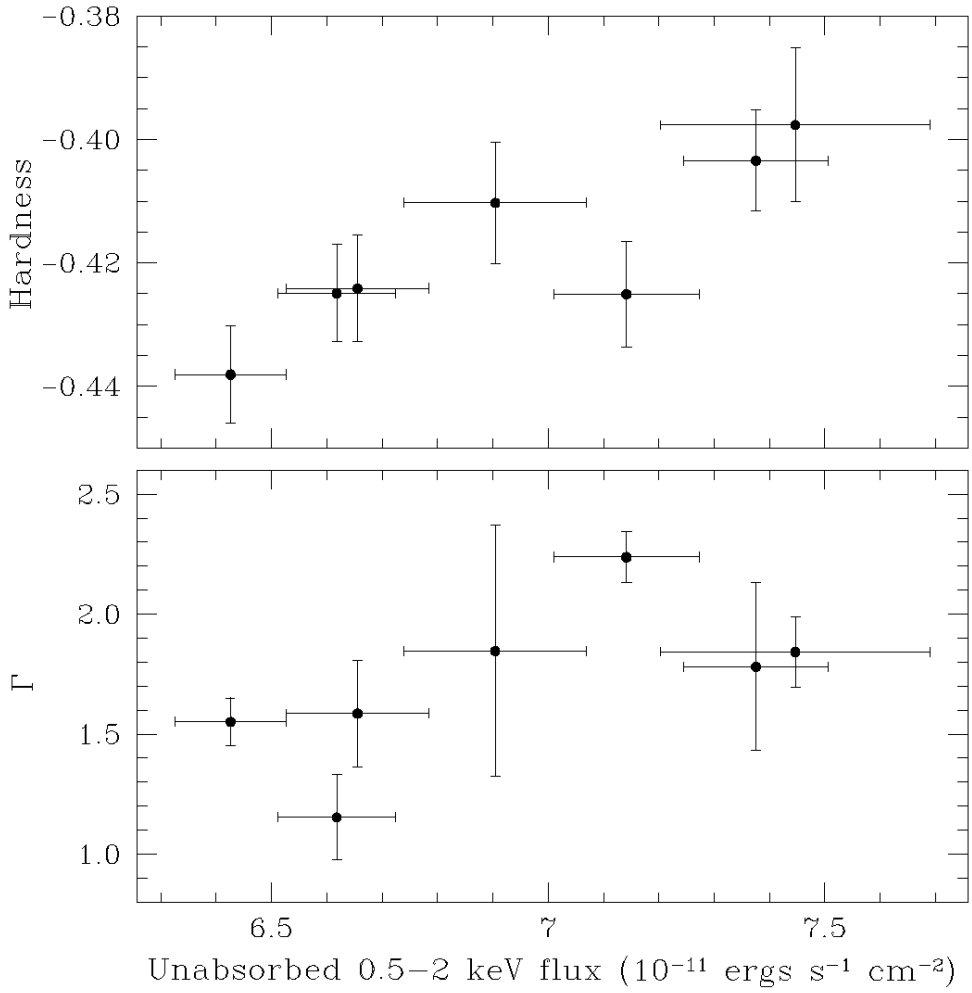

Figure 5.7: *Top*: Hardness versus flux from the *XMM–Newton* observations as given by the 2BB+BknPL model. *Bottom*: Power-law index Γ versus flux for the same observations. The unabsorbed flux in the 2–10 keV range was used.

The reported fluxes include a 2% error due to calibration uncertainties, which greatly dominates over statistical certainties, due to the large number of counts detected. We also find that the observed flux variability is mainly caused by changes in the observed PN count rate of the source and not uncertainties in the calibration of the instrumental response. An almost identical long-term behaviour in the count rate and flux is measured with MOS1 (operated in timing mode in all but the last observation), albeit with large cross-calibration offsets with respect to the PN instrument and a smaller number of counts. The MOS2 chips were operated in three different modes during 6 of these observations (it was turned off on 2002 February), with two imaging observations also showing an increase in the flux. Thus, we argue that the observed spectral changes are intrinsic to 4U 0142+61 and not dominated by calibration uncertainties.

We also find that while the hardness of the spectrum can be determined by flux changes at different energy ranges, it is not necessarily reflected by model parameters such as temperature and photon index (which are also very dependent on the model used to fit the spectrum). This is shown in Figure 5.7 using the values derived from the 2BB+BknPL model (as it is the most magnetar-inspired of the models used), where we find that the hardness versus flux data (top) deviate from a constant at the 2.7σ level while the photon index (bottom) is consistent with being constant. Similar results are obtained for the other models in Table 5.2 and the blackbody temperatures where, if anything, their values are slightly lower for observations taken after 2006 when the flux was higher and the spectrum was harder. However, no significant changes over time or with flux are seen here. On the other hand, the hardness changes are also present with higher significant (3.5σ) when looking at the count rates detected from the source at different energy ranges, supporting the results obtained through spectral analysis.

5.4.2 Pulsed Flux

We also studied the changes in pulsed flux during the observations, the values of which can be compared to those derived from the *RXTE* observations presented by Dib et al. (2007). We have estimated the pulsed flux for each observation by taking the phase-averaged flux calculated above and multiplying it by the pulsed fraction derived in §5.3.2 using the area method. The pulsed flux for each observation derived from the 2BB+BknPL model is shown in Figure 5.8 (using the absorbed flux, as strictly speaking only an "absorbed pulsed fraction" can be measured). Similarly, in Figure 5.9 we plot the absorbed pulsed flux in the 2–10 keV range derived from *RXTE* observations. Figure 5.9 is an updated version of that found in Dib et al. (2007) and is extended to include the most recent observations of 4U 0142+61. The flux in counts and energy are both shown, as the former allows for higher time resolution (the observations where bursts were seen are denoted with stars), while the latter combines multiple observations and allows for direct comparison with the lower panel of Figure 5.8 (see Dib et al., 2007; Gavriil et al., 2007b, for details). As can be seen from both Figures, the same long-term trend is present in both data sets, albeit *XMM–Newton* has larger uncertainties at 2–10 keV due to its lower sensitivity in this energy range and the smaller number of observations available. The apparent offset between the *RXTE* and *XMM–Newton* fluxes at 2–10 keV is likely caused by cross-calibration uncertainties.

5.5 Infrared Observations

Two Director's Discretionary Time (DDT) observations of 4U 0142+61 were obtained with the Gemini North Telescope, on 2006 June 30 and 2007 February 13. Both observations were taken 5–6 days after an X-ray burst (Dib et al., 2006; Gavriil et al., 2007a). K_S-band images were made with the Near-Infrared Imager (NIRI), an ALADDIN InSb 1024×1024 pixel detector array which, with the f/6 camera, provided a 119.9×119.9 arcsec^2 field of view and plate scale of $0\farcs117$ per pixel. The standard reduction procedures were performed using the Gemini package (v1.6) for

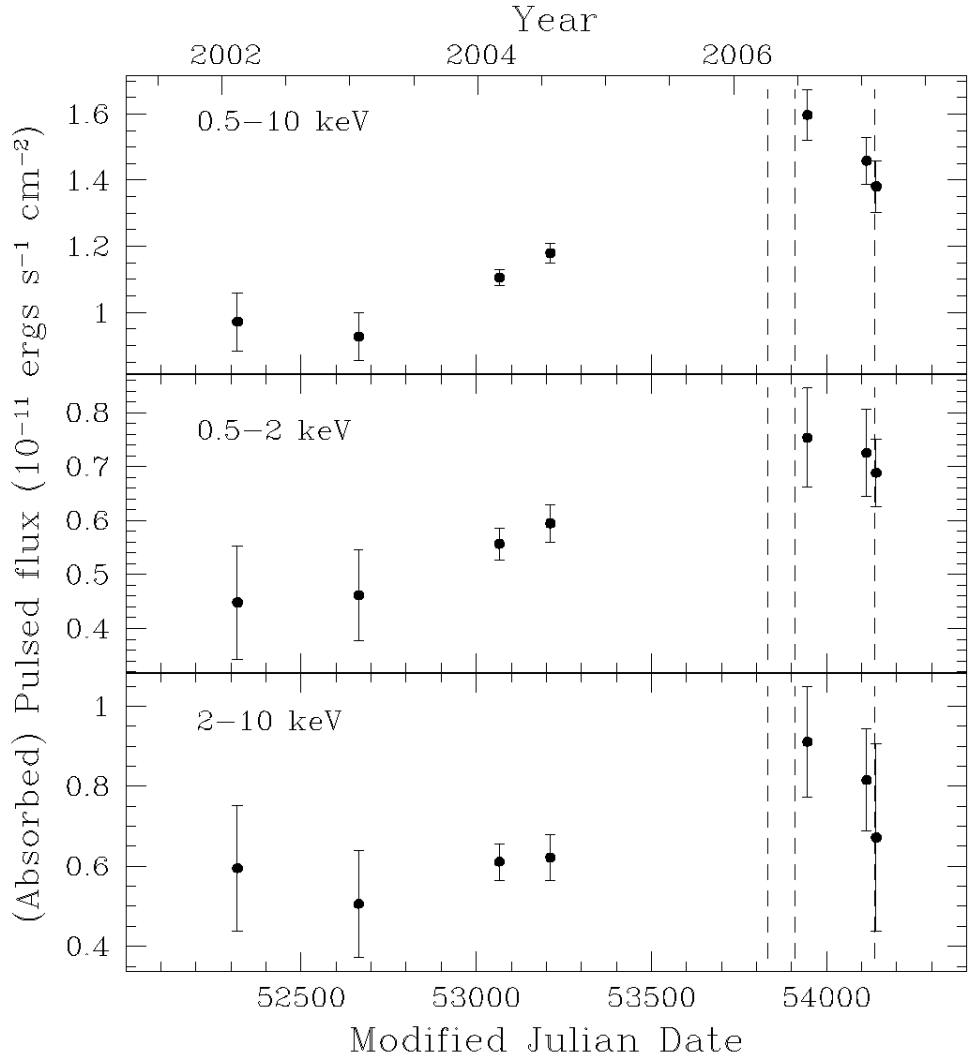

Figure 5.8: Pulsed fluxes for 4U 0142+61 obtained from the absorbed fluxes for the 2BB+BknPL model and the pulsed fraction derived using the area method. The dashed lines indicate the three burst epochs.

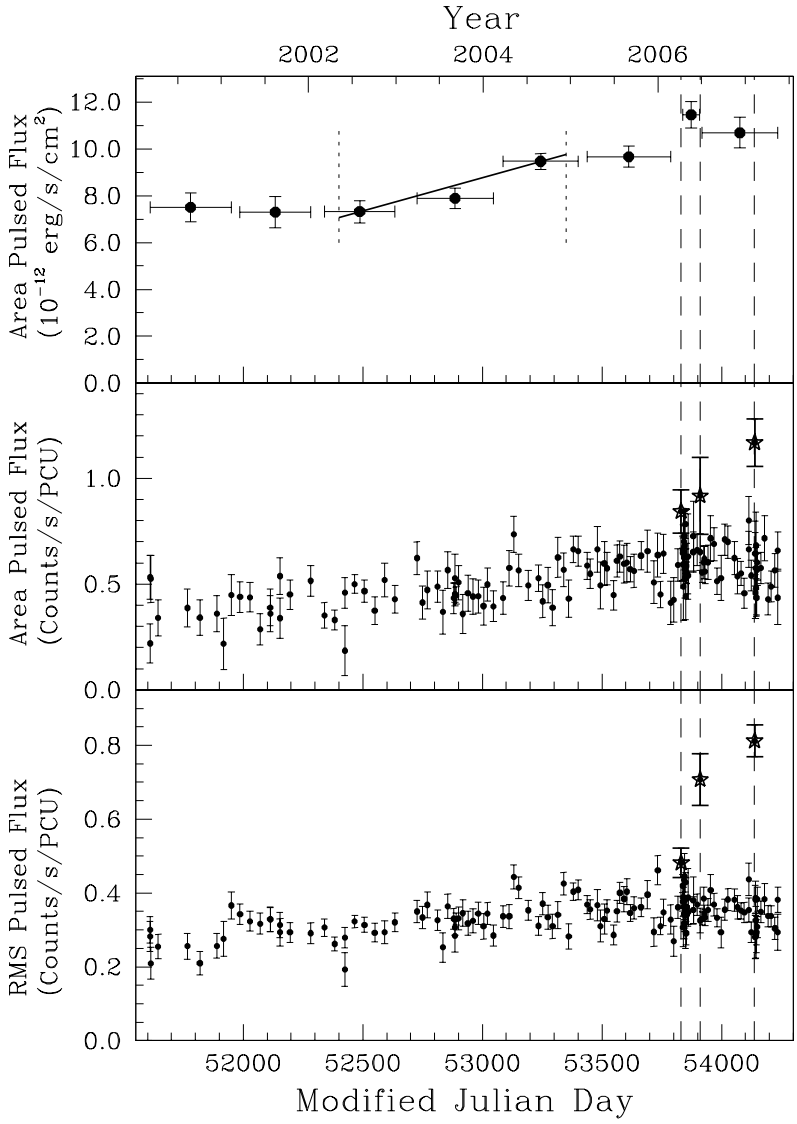

Figure 5.9: Pulsed fluxes for 4U 0142+61 in the 2–10 keV range obtained using *RXTE*. Fluxes in counts derived using the area (*centre*) and RMS (*bottom*) methods are shown for individual observations (those where bursts were seen are denoted with stars and dashed lines). Fluxes in energy (*top*) are absorbed and were obtained by combining multiple observations and fitting the resulting spectra using XSPEC. The sloped line (bounded by the two short dashed lines) shows the ≈29% pulsed flux increase reported in Dib et al. (2007).

IRAF (v2.12.2). Each frame was a 2×30 s integration; 17 dithered frames in 2006 June and 20 in 2007 February, were averaged to make one combined image for each observation.

The point source 4U 0142+61 was clearly identified in both Gemini observations. We used DAOPHOT in IRAF for point spread function (PSF) photometry; the FWHM of the PSF was approximately 0.″5 on 2006 June 30 and 0.″6 on 2007 February 13. Using the results of Hulleman et al. (2004), we calibrated our photometry relatively by measuring the K_S-band magnitude offsets of 10 nearby field stars and applying that offset to the 4U 0142+61 counterpart, incorporating the offset scatter into the final uncertainties. The final calibrated magnitudes are $K_S = 19.70 \pm 0.05$ and $K_S = 19.86 \pm 0.05$ mag in 2006 June and 2007 February, respectively. The uncertainties are DAOPHOT-determined and include the calibration uncertainties.

Observations of 4U 0142+61 before the bursts have encompassed a large magnitude range, from $K = 19.68 \pm 0.05$ to $K' = 20.78 \pm 0.08$ mag (Hulleman et al., 2004; Durant & van Kerkwijk, 2006c), consistent with the above values measured after the bursts. Therefore, we find no evidence to suggest that the AXP had brightened significantly in the near-IR several days after the X-ray bursts.

5.6 Discussion

We have found that the X-ray emission from 4U 0142+61 changed significantly from 2000–2007. Before the 2006 burst activity, the pulse profile became more sinusoidal and the pulsed fraction (and pulsed flux) increased. Our results agree with those of Dib et al. (2007) reported in the 2–10 keV range using *RXTE* data and we find that these changes are also present in the 0.5–2 keV band. During this time, the total flux was approximately constant with time (although a slight decrease is suggested depending on the spectral model used). The emission also showed an overall softening independent of the assumed spectral model (see Figures 5.5 and 5.6). After 2006, the total flux in the 0.5–10 keV range increased by ≈10% while the spectrum hardened for those observations close to the detected bursts (the spectrum softened in between

these observations). The flux increase after the bursts is also energy-dependent, with higher energies showing a larger increase. During this time, the pulse profile evolution towards more sinusoidal shapes stopped and the pulsed fraction was higher than before. We also find that in general, changes in flux and hardness of the spectrum appear to be correlated, with observations having a higher flux also showing a harder spectrum. This correlation appears to hold at least for the small range of flux phase-space that is covered by the current observations. In addition, the softening of the spectrum before 2006 agrees with the results presented by Dib et al. (2007) and the spectral hardening for observations close to detected bursts (in addition to a softening in between) agrees with the behavior observed by Gavriil et al. (2007b). Our pre-burst absorbed fluxes also agree with those of Rea et al. (2007a) reported using a BB+PL model.

5.6.1 AXP Variability

Anomalous X-ray pulsars exhibit a wide range of behavior in their variability, from sudden energetic bursts to long-term changes. The AXP 1E 1048–5937 was shown to have large, long-term flares of its pulsed flux (one of them lasting about a year, Gavriil & Kaspi, 2004) and variations by a factor of $\gtrsim$2 to its phase-averaged flux (Tiengo et al., 2005). This source has recently become active again, causing prolonged changes to its observed emission and showing a correlation between hardness and flux as seen here for 4U 0142+61 (Tam et al., 2007). Changes in the phase-averaged flux of 1RXS J170849.0–400910 of $\approx$60% on a timescale of years have also been reported (Campana et al., 2007) with a reported correlation between hardness and flux as well (albeit using various telescopes and instruments). 1RXS J170849.0–400910 was shown to have pulse profile changes possibly associated with glitches and low-level pulsed flux variations at various epochs, while 1E 1841–045 was shown to have possible long-term pulse profile changes and glitches with no obvious radiative changes (Dib et al., 2007). On the other hand, a large outburst accompanied by long-term changes in almost all

emission characteristics was seen in 1E 2259+586 that also shows a hardness–intensity correlation[5] (Kaspi et al. 2003; Woods et al. 2004; Zhu et al., in preparation).

The very low-level, long-term spectral changes seen here for 4U 0142+61 have not been observed thus far in other sources and were detected thanks to the high quality of the available data. The fact that the largest changes are suggested to be accompanied by bursting activity point to a common magnetar origin (see below). The overall changes in pulse and spectral properties of 4U 0142+61 support the view of magnetars as very active sources with a wide range of variability characteristics. We now discuss the observed changes in light of the commonly cited models for AXP emission: the magnetar and disk models.

5.6.2 The Magnetar Model

In the magnetar model, thermal X-ray emission from the surface provides seed photons which are resonantly Compton-scattered (RCS) to higher energies by the enhanced currents in a twisted magnetosphere (Thompson et al., 2002; Lyutikov & Gavriil, 2006; Fernández & Thompson, 2007). It is also expected that additional thermal emission will be produced by return currents from the magnetosphere that heat the surface. In turn, bursts of emission are explained as sudden, small-scale reconfigurations of the surface following a crustal yield due to a magnetospheric twist. Large outbursts are explained as global reconfigurations and/or reconnections of the magnetic field after a large twist. Long-term variability, assuming constant underlying thermal emission, is viewed as increases (or decreases) in the twisting of the

[5] We note that a BB+PL model fit to the observed emission from these sources results in large temperatures and steep power-law indices. As such, the power-law component may in fact dominate the observed emission below 1–2 keV, as shown in Figure 5.4 for 4U 0142+61. Therefore, the hardness–intensity correlations that are measured in terms of the value of the power-law index may be, counterintuitively, dominated by the evolution of the low-energy emission from these sources.

magnetosphere by currents from the stressed crust. The optical depth to scattering increases as the twist angle of the magnetosphere increases and in this case we expect a hardening of the spectrum to accompany an increase of the emitted flux. This scenario has been used to explain the hardness–intensity correlation observed in magnetars. The fact that the predicted correlation between flux and hardness is seen for 4U 0142+61 (with the brighter observations having a harder spectra) and that the largest changes are observed to coincide with a period of increased burst activity support this interpretation.

Özel & Güver (2007) have proposed that the hardness–intensity correlation observed in the afterglow emission from magnetars arises mainly from the cooling crust of the star and less so from changes in the magnetospheric currents. For example, most of the burst emission (arising from a large twist in the magnetosphere) can be deposited deep in the crust[6], heating it, and its subsequent cooling dominates the spectral evolution of the star. In this case, the observed temperature and total flux would have a direct correlation and could explain the hardness–intensity correlation.

However, this does not seem to be the case for 4U 0142+61. While the latest burst observed from it was the longest and among the most energetic detected from AXPs thus far (Gavriil et al., 2007a,b), all observations taken after the burst show a rapid return to the previous state without additional changes. This suggests that long-term recovery regions (e.g., the inner crust) have not been significantly affected, or that they were slightly affected and recovered very quickly. In either case, the bulk of the long-term changes observed after the bursts would be mainly magnetospheric in origin. This is supported by the fact that the main spectral changes appear to be dominated by the emission above 2 keV and that the evolution towards simpler, more sinusoidal profiles (generally associated with thermal emission from the surface) appears to have ceased.

[6] Güver et al. (2007) estimate a heating depth of ≈2.5 m for the outburst seen from the transient AXP XTE J1810–197.

We also note that the long-term evolution of the pulsed fraction in 4U 0142+61 does not show a simple correlation with the total flux. This is different from what is observed other sources, such as 1E 2259+586 and 1E 1048.1–5937, where larger phase-averaged fluxes correspond to lower pulsed fractions (Woods et al., 2004b; Tiengo et al., 2005; Tam et al., 2007). The behaviour of these AXPs could be accounted for, at least in principle, as a growing hot spot on the surface. In the transient AXP XTE J1810–197, as the source slowly fades after a large (undetected) burst around the end of 2002, the pulsed fraction and flux both decrease with time. This behavior may be interpreted as a fading hot spot against the background of a large-area cool blackbody (Gotthelf & Halpern, 2007). However, in the case of 4U 0142+61 we see a continuous increase in the pulsed fraction independent of the total flux, suggesting that different mechanisms contribute to this emission with varying strengths over time. The twisted magnetosphere model generally predicts that pulsed fractions should correlate positively with twist angles (Fernández & Thompson, 2007), and this mechanism could be responsible for the bulk of the increase during the observed bursting period. However, the continuous increase before the bursts is still hard to understand.

We thus find that the emission from 4U 0142+61 shows distinct characteristics from those of other AXPs, and while it generally agrees with magnetar models, the complicated evolution of the emission characteristics requires more detailed modeling than is presently available.

The hard X-ray emission observed in AXPs has also been proposed to arise from the twisted magnetosphere, which is thought to act as an accelerator and create a hot corona close to the surface of the star (Thompson & Beloborodov, 2005; Beloborodov & Thompson, 2007). In this case, we would expect the changes seen here (mainly those associated with the onset of bursts) to have corresponding changes at hard X-rays. den Hartog et al. (2007) report no variability within measurement errors for various observations carried out before 2006 and, due to the large uncertainties, it is not possible to measure changes at the $\approx$10% level. No measurements after the recent burst activity are reported and establishing/constraining any associated variability would be of interest.

The origin of the optical and IR emission in the magnetar model is not well understood, with the proposed mechanisms not studied in detail, thus having uncertain correlation with the X-ray flux (see Thompson & Beloborodov, 2005). We find no significant change in the near-IR flux after the bursts that could be correlated with the overall increase in the X-ray flux during this time. However, given the large variability seen from 4U 0142+61 in the optical/IR and the subtle nature of the changes in X-rays, we cannot test for a possible correlation between the emission at these wavelengths.

5.6.3 The Disk Models

The discovery of mid-IR emission from a possible disk around 4U 0142+61 has prompted debate as to whether it is a passive (Wang et al., 2006) or an active disk (Ertan et al., 2007a). In the case of a passive disk the magnetar mechanism is still needed to explain the X-ray emission from the star, while an active disk accretes onto a star with a dipole field of $\sim 10^{12-13}$ G (a magnetar field in the quadrupole or higher components in then needed to explain the bursting behavior; Ertan et al., 2007b,a). The (unpulsed) optical/IR/UV emission results from the disk as it radiates through viscous energy dissipation and by irradiation from the star. Most of the disk radiation, which peaks in the IR, comes from the outer regions.

The fact that the main spectral changes are seen to correlate with increased burst activity (associated with a magnetar nature) argue against a disk origin. Although an increased X-ray flux from the star can affect the irradiation emission from the putative disk around 4U 0142+61, these X-ray changes might or might not be accompanied by changes at longer wavelengths depending on the reprocessing efficiency of the disk. As the X-ray flux is still observed to be higher in the last observation, changes in the optical/IR might be present. However, the large range of previously reported IR fluxes does not allow for intrinsic changes in the emission of several percent, as observed in the X-ray range, to be readily identified.

5.7 Summary

We found that long-term changes are present in the X-ray emission from the AXP 4U 0142+61, including evolution of the pulse profile, increase in pulsed fraction (and thus pulsed flux), as well as changes in the hardness and in the total flux. As predicted by the magnetar model, the largest changes in flux and hardness of the spectrum are observed to coincide with the increased burst activity from the source during 2006–2007. The characteristics of the observed changes in the emission during this time suggest that they are mainly magnetospheric in origin. However, changes are seen before the burst activity that suggest that multiple emission mechanisms are likely to be present in this (and maybe other) magnetar.

Chapter 6

X-ray Observations of the Vela-like Pulsar PSR B1046−58

In this chapter we present results from *Chandra* and *XMM–Newton* observations of the radio pulsar PSR B1046−58. The high spatial resolution of the *Chandra* data allowed for the discovery of an asymmetric, arc-second scale PWN surrounding this young, energetic pulsar. The overall size and energetics of the system are very similar to those of the Vela pulsar and its nebula. We discuss the origin of the PWN in PSR B1046−58 in the case that it arises from emission downstream of the wind termination shock in a static nebula or from emission confined due to a high space velocity for the pulsar. These results demonstrate the need for high-resolution, high-sensitivity observations in order study the wide range of structures associated with rotation-powered pulsars.

The results presented here were first published in the refereed article: *Gonzalez, M. E.*, Kaspi, V. M., Gaensler, B. M., & Pivovaroff, M. J., *Chandra and XMM-Newton Observations of the Vela-like Pulsar PSR B1046−58*, Astrophysical Journal, 652, 569−575, 2006

6.1 Introduction

X-ray observations of rotation-powered pulsars represent a powerful tool to study the energetics and emission mechanisms of these objects. A large fraction of the available rotational energy is thought to be carried away in a relativistic wind of particles. When this wind is confined by the surrounding medium it decelerates and a synchrotron-emitting nebula forms, called a pulsar wind nebula (PWN, see §1.6). Measurements of the morphology and spectrum of these nebulae help us to understand the physical mechanisms involved in the conversion of rotational kinetic energy into high-energy outflows, a common feature from pulsars to extragalactic black holes. The overall PWN characteristics provide insights into the particle content and energy spectrum of the outflowing pulsar wind, the large-scale magnetic fields in the nebula, and the characteristics of the surrounding medium. The small-scale structures of the nebula provide details about the acceleration sites, instabilities in the magnetic field, and the interaction between the wind and its surroundings. In addition, for young, energetic pulsars it is expected that nonthermal emission from particles accelerated within the magnetosphere and thermal emission from the surface of the star are also present. Albeit it can be hard to disentangle the emission from these processes, pulsars that exhibit all of the above emission processes are excellent testing sites for our current understanding of these objects.

The radio pulsar PSR B1046−58 was discovered during a survey of the Galactic plane by the Parkes telescope (Johnston et al., 1992). It has a period of $P = 124$ ms and period derivative $\dot{P} = 9.6{\times}10^{-14}$ s s^{-1}. These values imply a characteristic age of $\tau_c = P/2\dot{P} = 20.4$ kyr, spin-down luminosity of $\dot{E} = 2.0{\times}10^{36}$ ergs s^{-1} and surface dipole magnetic field strength of $B = 3.5{\times}10^{12}$ G. The dispersion measure of 129 pc cm^{-3} towards the pulsar implies a distance of 2.7 kpc (Cordes & Lazio, 2002).

Figure 6.1 shows the traditional $P - \dot{P}$ diagram for pulsars highlighting those thought to be "Vela-like". These pulsars have similar characteristics to those of the Vela pulsar: they are sufficiently young ($\tau_c \sim 10^{4-5}$ yrs) and energetic ($\dot{E} \sim 10^{36-37}$ ergs s^{-1}) such that they are expected to have emission from all of the above processes (non-thermal emission from the magnetosphere, thermal emission from the surface,

and non-thermal, extended emission from a pulsar-powered nebula). The estimated age and spin-down luminosity of PSR B1046−58 place it within this group of pulsars.

In this chapter we present observations of PSR B1046−58 carried out with the *Chandra* and *XMM–Newton* satellites. The high spatial resolution of the data allowed for the discovery of a faint, arcsecond-scale PWN surrounding the pulsar. In addition, a detailed imaging and spectral analysis of the system suggests that in addition to magnetospheric emission, soft (possibly thermal) emission from the surface is also present. We also examine the characteristics of the nebula in light of current models for the production of PWNe.

6.2 X-ray Observations

PSR B1046−58 was observed with *XMM–Newton* on 2002 August 10. The EPIC MOS and PN instruments were operated in full-frame and small-window modes, respectively. These settings provide a temporal resolution of 2.6 s for MOS and 6 ms for PN. In addition, while the MOS camera had a FOV of $30'$, for the PN camera this value was $4'$ so that a fast readout time could be achieved. The standard screening criteria result in an exposure time for the MOS and PN cameras of 20 ks and 15 ks, respectively.

The *Chandra* observation of PSR B1046−58 was carried out on 2003 August 8-9. The aimpoint of the back-illuminated ACIS-S3 chip was positioned at the radio coordinates of the pulsar. The observation was taken with a temporal resolution of 3.2 s. Excluding times of high background, the effective exposure time for the observation was 36 ks.

The PN instrument offers a higher sensitivity than ACIS-S, but its lower exposure time and reduced field of view limited its use for spectral and temporal analyses of the pulsar emission. In turn, the *Chandra* data were used to perform spectral and high-resolution imaging analyses of PSR B1046−58 and its surroundings, while the

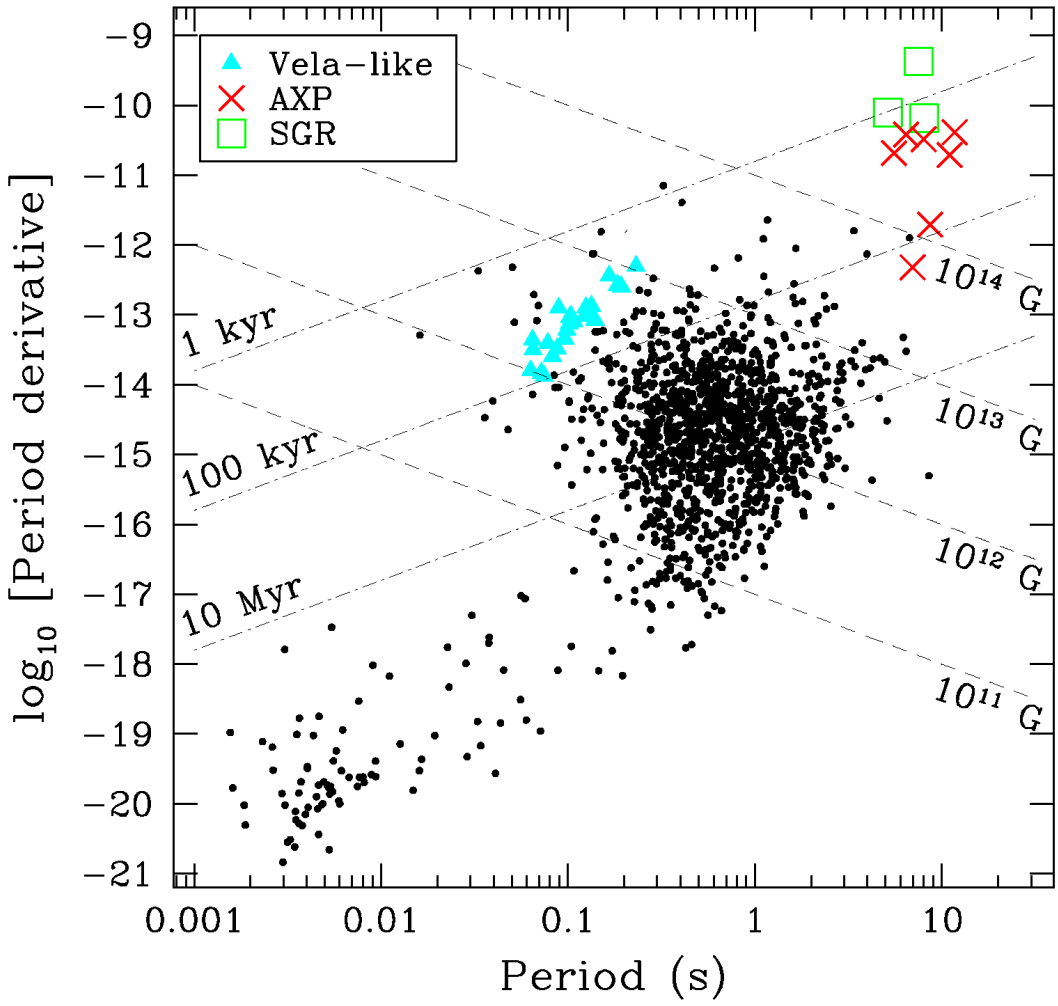

Figure 6.1: $P - \dot{P}$ diagram illustrating the population of radio pulsars thought to have Vela-like properties (blue triangles). Here, these pulsars are defined as having ages of 10^{4-5} yrs and spin-down energies of 10^{36-37} ergs s^{-1}. Radio pulsars are shown as black circles, with magnetars labeled as shown. Figure provided by C. Tam.

MOS observations were used mainly as a consistency check due to their lower sensitivity and lower spatial resolution.

6.3 Imaging Analysis

To search for extended emission surrounding the pulsar, the high-resolution *Chandra* data were used. Figure 6.2 shows the area surrounding the radio position of PSR B1046−58. The image has been smoothed with a Gaussian with σ=0.″5. It reveals for the first time the detailed extended structures surrounding PSR B1046−58, which we designate as its pulsar wind nebula based on its overall characteristics discussed in the next sections. The nebula is elongated and $\approx 6'' \times 11''$ in size, with its major axis oriented in a SE-NW direction. The flattened ellipse in Figure 6.2 marks the radio coordinates of the pulsar at α_{2000}=$10^h48^m12\overset{s}{.}6(4\overset{''}{.}7)$ and δ_{2000}=$-58°32'03\overset{''}{.}75(0\overset{''}{.}02)$, 2σ errors (Stappers et al., 1999). While there is emission immediately surrounding the pulsar position (PWN "head"), there is also clumped emission to the SE (PWN "body") and a bright clump to the NW ("north clump")[1].

The head region of the nebula is consistent with a point source surrounded by extended structures. Figure 6.3 shows the intensity profile of the observed emission along a $10'' \times 35''$ region in a SE-NW direction aligned with the implied axis of symmetry of the nebula. The shaded region represents the 2σ background level obtained from a nearby, source-free region. The dashed line represents *Chandra*'s PSF at an energy of 1.5 keV obtained using the available calibration data. As the head region is also consistent with the radio coordinates of the pulsar, we consider the source embedded in the region to be the X-ray counterpart of the pulsar. Comparing the X-ray position of other sources in the field with their optical counterparts we derive an X-ray position for the pulsar of α_{2000}=$10^h48^m12\overset{s}{.}64$ and δ_{2000}=$-58°32'03\overset{''}{.}6$, with

[1] We note that thanks to the suggestion of Dr. Mallory Roberts and his ever-growing designation of PWNe after (mostly) cute animals, we have unofficially name this nebula the "Puppy".

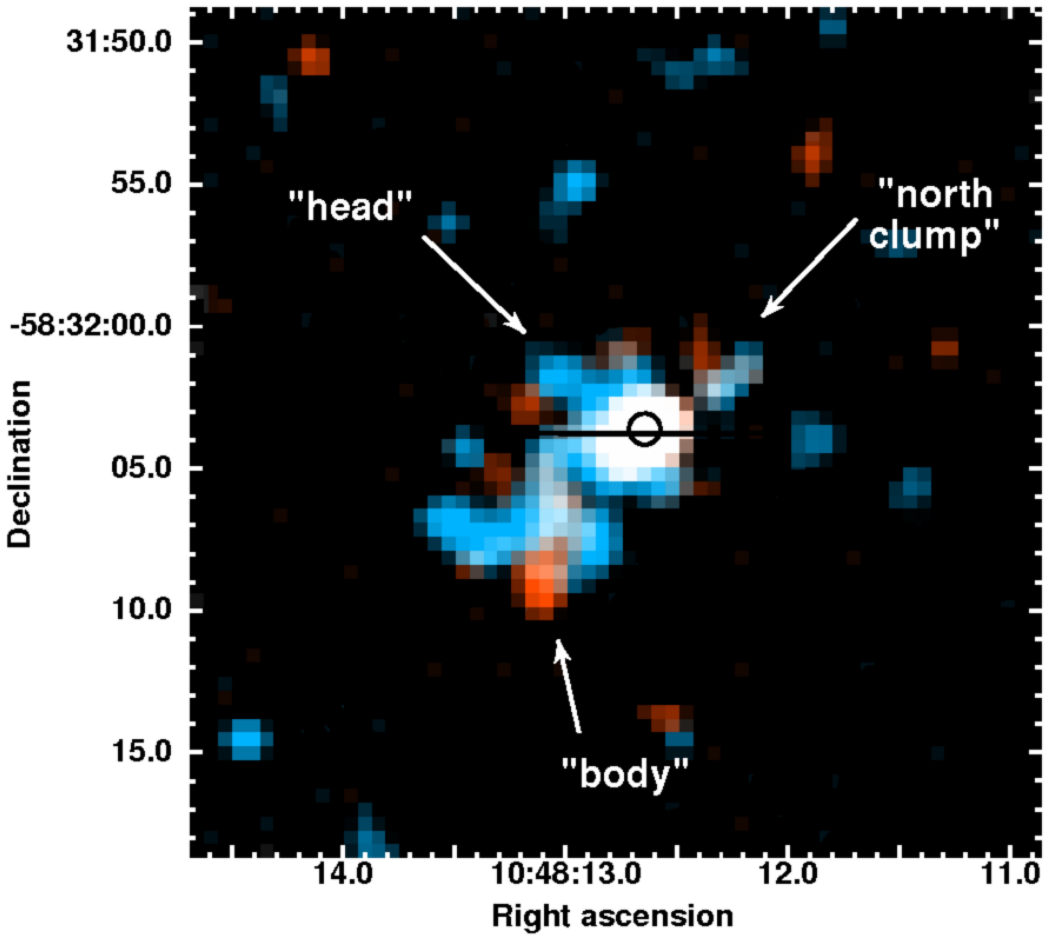

Figure 6.2: Combined *Chandra* image of PSR B1046−58 and its PWN using individual images in the 0.5−2.0 keV (*red*) and 2.0−10.0 keV (*blue*) ranges. Each image was smoothed with a Gaussian with σ=0.″5. The circle (0.″55-radius) and ellipse (4.″7×0.″02 axes) mark the X-ray and radio positions of the pulsar, respectively (see §6.3). The main components discussed in the text are labeled.

an overall rms error of $0\farcs55$. This is coincident within 1σ of the radio position. We then define the "pulsar" emission as that arising in a circle of $1''$ in radius centred on the above X-ray coordinates.

We also find that the extended emission from the PWN dominates at high X-ray energies. Table 6.1 shows the number of background-subtracted counts obtained for various parts of the system in the soft (S) and hard (H) bands, their hardness ratios (HR = S−H / S+H) and their total signal-to-noise ratio (S/N, e.g., Pivovaroff et al., 2000) in the 0.5−10.0 keV range. While emission from the nebula is likely to be present within the $1''$ radius used for the pulsar, we suggest that emission from the neutron star is indeed present (and may dominate) in this region. The above is supported by the fact that this region is the only one that is seen to exhibit a positive HR with high significance, suggesting a contribution of distinctly softer emission than the rest of the nebula.

Table 6.1: Spatial analysis of PSR B1046−58 and its PWN with *Chandra*

Region	0.5−2.0 keV counts (S)	2.0−10.0 keV counts (H)	HR = (S−H)/(S+H)	S/N (0.5−10.0 keV)
Pulsar ($1''$ radius[a])	43 ± 8	24 ± 6	0.27 ± 0.10	8.5σ
PWN, all (- Pulsar)	46 ± 9	70 ± 11	−0.21 ± 0.06	9.1σ
PWN, "head" (- Pulsar)	12 ± 5	31 ± 7	−0.44 ± 0.21	6.1σ
PWN, "body"	22 ± 6	34 ± 7	−0.22 ± 0.10	9.1σ
"North clump"	5 ± 2	5 ± 2	0.00 ± 0.02	2.9σ
Pulsar + PWN	89 ± 11	95 ± 12	−0.03 ± 0.01	12.1σ

[a] See §6.3 for detailed discussion.

Using *ASCA*, Pivovaroff et al. (2000) detected four point sources within $\approx 4'$ of the radio position of the pulsar embedded in possible faint emission. The *Chandra* and *XMM–Newton* observations confirm the presence of these X-ray point sources in the field, in addition to many others resolved by *Chandra* (see Figure 6.4). A soft point source in the *Chandra* data coincident with "Src 2" from Pivovaroff et al. (2000) and has an optical counterpart in the USNO B1.0 catalog (Monet et al., 2003). We find

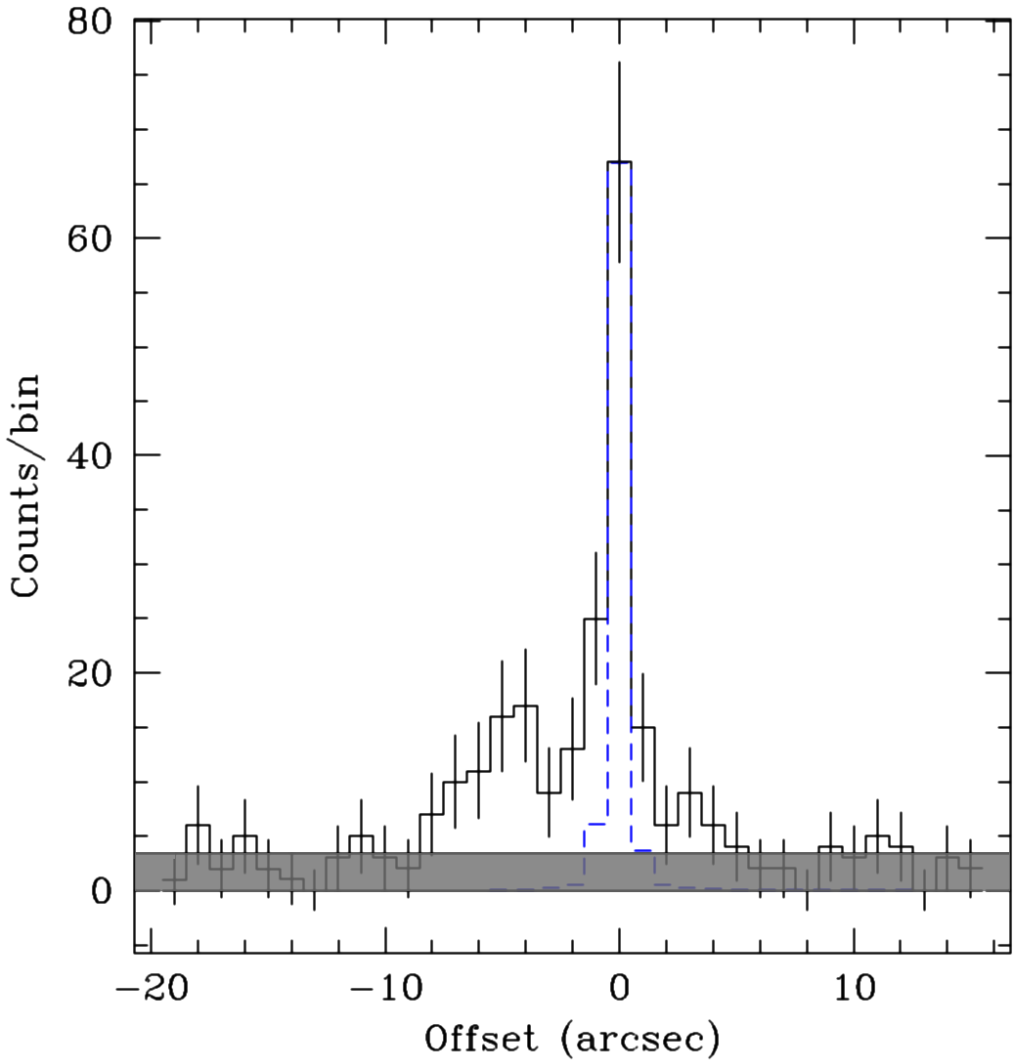

Figure 6.3: *Chandra* axial profile of PSR B1046−58 and its PWN in the 0.5−10.0 keV range in a SE-NW direction (solid line) aligned with the implied axis of symmetry (see Figure 6.2). The origin represents the X-ray position of the pulsar. The extended emission at offsets of $\approx -3''$ to $-8''$ arises from the "body" of the PWN (in the SE direction) while the emission at offsets of $\approx 3''-5''$ arises from the "north clump". We also show the 2σ level of the background (shaded region) along with the PSF of the telescope at 1.5 keV (dashed line).

no counterparts for the hard sources coincident with "Src 3" and "Src 4" in present catalogues (e.g., USNO B1.0; 2MASS, Cutri et al. 2003; RASS, Voges et al. 2001). No additional extended emission was detected that can be attributed to the PWN beyond the above arc-second structures. We conclude that the low angular resolution and broad PSF wings of the telescope significantly affected the *ASCA* observations due to the large number of point sources in the field. We also note that the *ASCA* positions appear to be systematically north of the *Chandra* coordinates, the latter being in agreement with source positions at other wavelengths.

6.4 Spectral Analysis

The data obtained from both *Chandra* and *XMM–Newton* were used to perform a spectral analysis of the emission from PSR B1046−58 and its PWN. For the *Chandra* data, an elliptical region of $12'' \times 18''$ in size was used with a surrounding annulus as background. A total of 184±14 background-subtracted counts were detected in the 0.5−10.0 keV range. The *XMM–Newton* data were extracted from circular regions of $25''$ radii in each detector, encompassing ≈77% of the photons from a point source, with a nearby region used as background. The data from MOS1 and MOS2 were not included in the analysis due to the low number of counts detected in them (background-subtracted counts from nearby source-free regions of 106±17 and 47±17, respectively[2]). The PN detector collected 260±47 background-subtracted counts in the same range. The extracted spectra from *Chandra*'s S3 chip and *XMM–Newton*'s PN detector were fit simultaneously in the 0.5−10.0 keV range using XSPEC (v.11.3.0) and a minimum of 20 counts per bin in each spectrum.

Thermal models for the integrated emission from PSR B1046−58 and its PWN are statistically acceptable ($\chi^2_\nu \approx 1.1$). However, they result in far too high temperatures

[2] It has been found that the MOS1 count rate can be artificially boosted by statistical fluctuations by up to ≈70%, especially for sources with <50 true counts. See §2.1 and §4 in http://xmm.vilspa.esa.es/docs/documents/CAL-TN-0023-2-1.ps

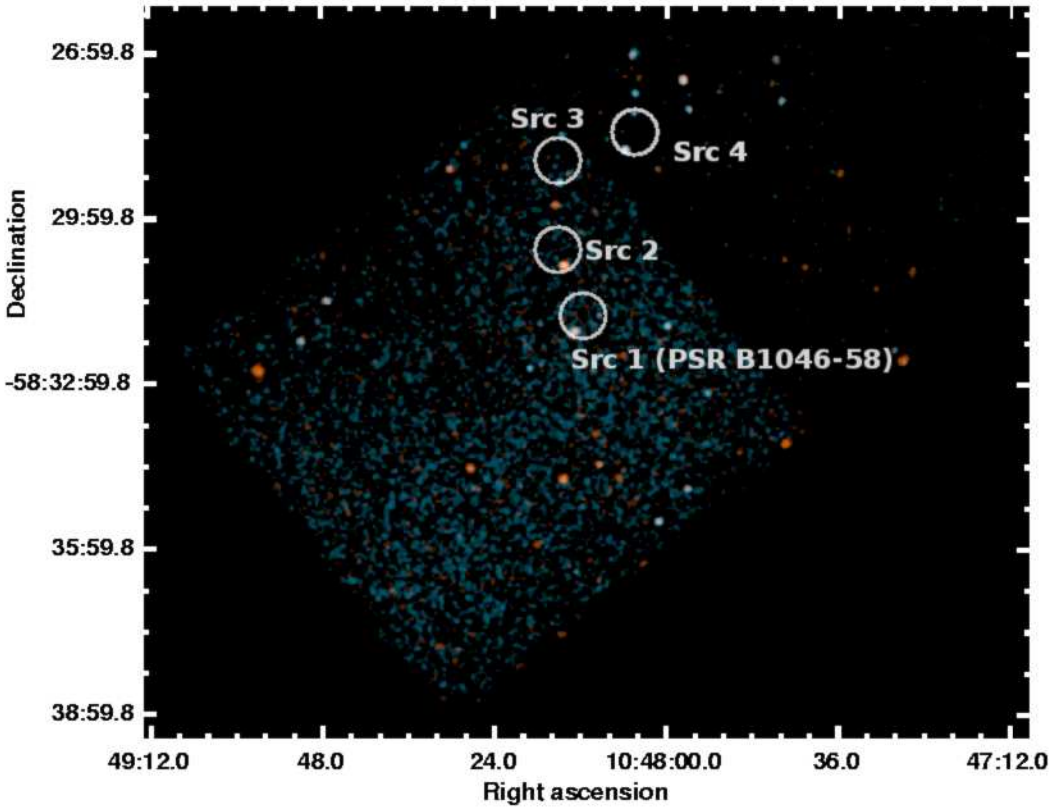

Figure 6.4: *Chandra* image of the field surrounding PSR B1046−58 obtained from the ACIS-S3 chip and part of ACIS-S2. Individual background-subtracted and exposure corrected images in the 0.5−2 keV (*red*) and 2.0-10 keV (*blue*) ranges were used. The images were smoothed with a gaussian with σ=2″. The circles mark the position of the sources detected with *ASCA* and their uncertainties (25″ radius, see Pivovaroff et al., 2000), all of which are coincident with resolved point sources in the present observations. Similar results (although at lower angular resolution) were obtained with the *XMM–Newton* MOS instruments. No extended PWN or supernova remnant emission was detected in the data.

to represent shock-heated thermal plasma (T>8×10^7 K, Raymond-Smith model, Raymond & Smith, 1977) or emission from the surface of the neutron star (T>1×10^7 K, blackbody model). Instead, a non-thermal absorbed power-law model produces an equally acceptable fit (see Table 6.2) with a photon index of $\Gamma=1.7^{+0.4}_{-0.2}$, similar to what is observed for other pulsars and their PWNe (e.g., Gaensler & Slane, 2006). The *Chandra* spectrum with the best-fit power-law model is shown in Figure 6.5. The observed emission is thus consistent with having a predominantly non-thermal origin.

Table 6.2: Power-law fit to combined emission from PSR B1046−58 and its PWN[a]

Parameter	Value ($\pm1\sigma$)
N_H (10^{22} cm^{-2})	$0.9^{+0.4}_{-0.2}$
Γ	$1.7^{+0.4}_{-0.2}$
χ^2(dof)	79(68)
f_{abs}[b] (ergs s^{-1} cm^{-2})	$0.7^{+0.6}_{-0.1}\times10^{-13}$
f_{unabs}[b] (ergs s^{-1} cm^{-2})	$1.0^{+0.7}_{-0.2}\times10^{-13}$
L_X[c](ergs s^{-1})	$0.9^{+0.6}_{-0.2}\times10^{32}$

[a] Simultaneous fit to both *Chandra* and *XMM–Newton* spectra.
[b] Absorbed and unabsorbed X-ray fluxes, f_{abs} and f_{unabs}, in the 0.5−10.0 keV range.
[c] Unabsorbed X-ray luminosity in the 0.5−10.0 keV range for a distance of 2.7 kpc.

We then searched for differences in the spectral characteristics of the different components of the system, as is hinted from our imaging analysis. The high spatial resolution available with *Chandra* was required in this case. The 116±14 counts detected from the PWN alone were fit with a power-law model. Holding the interstellar absorption fixed to the best-fit value from Table 6.2, the resulting photon index was $\Gamma_{PWN} \sim 1.2$. Holding this contribution from the nebula fixed while fitting the overall spectrum, the residual (presumably pulsar-dominated) emission was well described by a power-law model with a photon index of $\Gamma \sim 2.4$. If a blackbody model is fitted to

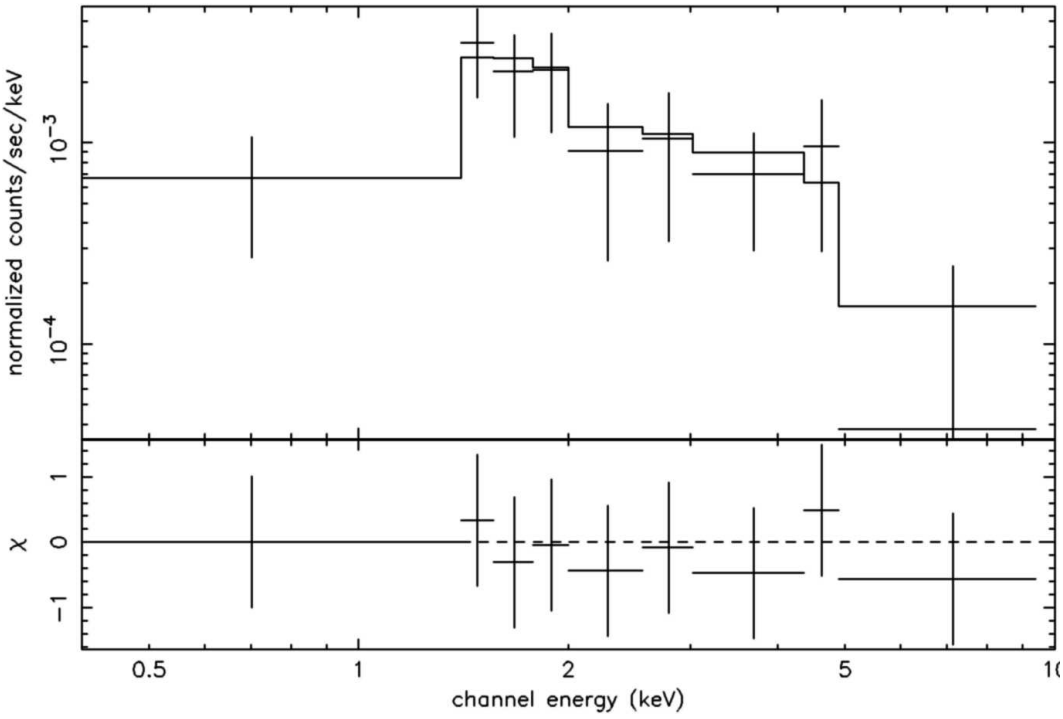

Figure 6.5: *Chandra* spectrum of the combined emission from PSR B1046−58 and its PWN. The data were binned to contain a minimum of 20 counts bin^{-1}. The solid line represents the best-fit power-law model shown in Table 6.2 and the lower panel shows the fit residuals.

this emission the resulting temperature is $\sim 6.1 \times 10^6$ K, too high to represent purely thermal emission from the neutron star but lower than thermal fits to the overall spectrum. Therefore, although the small number of counts did not allow us to constrain the above parameters, emission from the pulsar which is softer than that of the nebula seems to be present.

6.5 Timing Analysis

The data from the *XMM–Newton* EPIC-PN camera were used to search for pulsations from PSR B1046−58. No evidence for an instrumental 1-s jump in the data was found (see, e.g., Woods et al., 2004a). The data set was converted to the solar system barycenter and a circular region of 25″ radius centred at the above *Chandra* coordinates was used to extract the pulsar events. We also examined the data set at different energy ranges using 0.5−10.0 keV, 0.5−2.0 keV and 2.0−10.0 keV bands. Radio observations of the pulsar obtained with the Parkes telescope predict a period for the middle of our observation (MJD 52496.5) of $f = 8.08512306$ Hz ($P = 123.683955$ ms).

The Z_n^2 test (Buccheri et al., 1983) was used to search for a periodic signal by folding the extracted photons over a range of 10 trial frequencies centred on the radio prediction. The number of harmonics used was varied to be $n = 1$, 2, 4, and 8. The most significant signal was found in the 0.5−2.0 keV range at f=8.08517(4) Hz (1σ error) with $Z_2^2 = 8.9$. Although this signal is consistent with the radio period of PSR B1046−58, it has a probability of chance occurrence of 6.3% for a single trial and it is not significant given the number of searches performed. Following Vaughan et al. (1994) and, e.g., Ransom et al. (2002), we can derive an upper limit on the pulsed fraction. Assuming a worse-case sinusoidal modulation, the maximum Fourier power obtained for a small range of frequencies centred on the radio prediction can be used to calculate an upper limit for the pulsed fraction at a specific level of confidence. In this way, we derive an upper limit for the pulsed fraction at the 99% confidence level of 53%, 65% and 61% in the 0.5−10 keV, 0.5−2.0 keV and 2.0−10.0 keV ranges,

respectively.

6.6 Discussion

6.6.1 PSR B1046−58

X-ray emission from young radio pulsars is expected to include contributions from any of the following processes: thermal emission from the entire surface due to initial cooling, non-thermal emission from magnetospheric processes, and possibly thermal emission from localized hot spots reheated by back-flowing magnetospheric currents (see, e.g., Kaspi et al., 2004).

The combined emission from the pulsar and its PWN is best described by a non-thermal power-law model. However, our imaging and spectral analysis suggests that an additional, soft component may be present in the pulsar's emission. The soft emission can be well described by a steep power law with $\Gamma \approx 2.4$, although such an interpretation would contradict the generally observed trend of young pulsars having spectral indices harder than those of their PWNe (e.g., Gotthelf, 2003). The additional soft emission cannot be entirely thermal, as the derived temperature is too high. It could, however, represent a combined spectrum of (hard) non-thermal plus (soft) thermal emission. The number of counts detected does not allow us to fit two-component models to this emission alone. Instead, in the case that this overall soft excess is related to thermal emission from the surface, we can constrain its temperature by fitting a blackbody plus power-law model and finding the maximum temperature that yields an acceptable fit to the total spectrum. We adopt hard limits for the interstellar absorption of $N_H < 2{\times}10^{22}$ cm^{-2} and a blackbody radius observed at infinity of $R^{\infty} > 10$ km (at a distance of 2.7 kpc). The power-law index and normalization were allowed to vary freely and the maximum blackbody temperature that causes deviations from the best-fit model at the 3σ level was found. This results in a surface temperature of $T_{bb}^{\infty} < 1.4{\times}10^6$ K. The predicted temperature in the case of minimal cooling $\sim 1.1{\times}10^6$ K for the pulsar's characteristic age (e.g., Page et al., 2006). It is therefore possible that cooling radiation is present in the emission from

PSR B1046−58.

6.6.2 The PWN

The high spatial resolution available with *Chandra* allowed us to discover the arc-second scale PWN structures surrounding the pulsar. The "head" of the nebula is coincident with the radio position of the pulsar, while diffuse emission is seen predominantly to the SE. The emission from the pulsar and PWN is very faint, with a combined unabsorbed luminosity of only $\approx 1\times10^{32}$ ergs s^{-1} in the 0.5−10.0 keV range. The efficiency with which the pulsar converts its rotational kinetic energy into X-rays is then $\eta_X \equiv L_X/\dot{E} \approx 5\times10^{-5}$, comparable to those found for other Vela-like systems (e.g., Pavlov et al., 2001; Camilo et al., 2004).

Radio observations revealed no emission from the PWN. Constraints on the radio properties depend directly on the underlying assumption for the radio efficiency ($\eta_R = L_R/\dot{E}$; Stappers et al., 1999). Detected nebulae show efficiencies in the range $\eta_R \sim 10^{-4}$−10^{-3}, while upper limits for unseen nebulae imply values of $\eta_R \lesssim 10^{-5}$ (Frail & Scharringhausen, 1997; Gaensler et al., 2000). In the case of an undetected, extended radio nebula surrounding PSR B1046−58 and using a value of $\eta_R = 2\times10^{-4}$, the upper limit on the radio flux and required surface brightness imply a large radius of 8 pc for a circular nebula (Stappers et al., 1999). At a distance of 2.7 kpc this represents a radius of $\approx 10'$. While the X-ray size of PWNe is often found to be up to a few times smaller than the radio size due to smaller synchrotron lifetimes in the X-rays (e.g., Hester et al., 2002), we find no evidence for extended PWN structures on arcminute scales. For radio sizes $\lesssim 30''$, based on the small angular size of the X-ray nebula, the required efficiencies are very low at $\eta_R \lesssim 5\times10^{-7}$.

A static nebula?

The origin of PWNe is commonly attributed to the interaction of a highly relativistic pulsar wind with its surroundings. At a radius r_s from the pulsar, representing the point of pressure balance at which the wind is confined and decelerated, we expect

$\mathsf{P} = \dot{E}/4\pi\Omega r_s^2 c$. Here, P is the surrounding pressure and $\Omega \leq 1$ is the filling factor of the wind. As the head region of the nebula is resolved as an extended structure with *Chandra*, we suggest that its outer radius can represent an upper limit on the location of the wind termination shock, while the body represents the expected emission downstream. The shock radius in this case is $r_s < 2'' = 0.026\ d_{2.7}$ pc, very similar to that found for the Vela pulsar (Helfand et al., 2001) and an order of magnitude smaller than those of much more energetic pulsars such as the Crab and PSR B1509−58 (e.g., Weisskopf et al., 2000; Gaensler et al., 2002). The required pressure in this case is $\mathsf{P} \gtrsim 8.2{\times}10^{-10}\ d_{2.7}^{-2}$ ergs cm^{-3} ($d_{2.7}$ is the distance to the pulsar in units of 2.7 kpc). In the region downstream of the shock we expect equipartition between the particles and magnetic field to be reached, so that $B^2/4\pi = \mathsf{P}$, where B is the mean magnetic field in the nebula. We then estimate a value of $B \gtrsim 100\ d_{2.7}^{-1}\ \mu$G. The corresponding synchrotron lifetime of particles emitting at an energy ϵ_{keV} (in units of keV) is very small, at $t_{\rm synch} \lesssim 40\ d_{2.7}^{3/2}\ \epsilon_{keV}^{-1/2}$ yr. The velocity that is needed for these particles to reach the edge of the nebula within their synchrotron lifetimes is $v \gtrsim 2{,}600\ d_{2.7}^{-1/2}\ \epsilon_{keV}^{1/2}$ km s^{-1} $\gtrsim 0.01\ d_{2.7}^{-1/2}\ \epsilon_{keV}^{1/2}\ c$.

One problem with the above interpretation is that we expect the emission downstream of the shock to be symmetric about the pulsar. A possible explanation for the lack of emission to the NW involves Doppler boosting of the approaching (in this case SE) component. The observed flux ratios on either side of the pulsar require an intrinsic expansion velocity of $v \sin\theta \gtrsim 0.22c$, where θ is the inclination of the nebula to the line of sight. Similar velocities are found in the structures of other PWNe, such as the Crab (Hester et al., 2002). Also, an intrinsically (highly) asymmetric pulsar wind could be responsible for the observed characteristics.

Furthermore, the emission in the body of the nebula could represent mainly a collimated outflow, or jet, along the pulsar spin axis, as observed in other systems such as the Crab and Vela (Weisskopf et al., 2000; Helfand et al., 2001). In this case, we can estimate the minimum magnetic field and energy needed to support the jet against the surrounding pressure using equipartition arguments (e.g., Pacholczyk, 1970; Seward et al., 1984). We assume the jet to be a cylinder with length $l_j = 6.5''$

$= 0.085 d_{2.7}$ pc and radius $r_j = 1.5'' = 0.020 d_{2.7}$ pc, resulting in an emitting volume of $\mathsf{V} \sim 3{\times}10^{51} d_{2.7}^3$ cm^3. From the results shown in Tables 6.1 and 6.2, we infer an unabsorbed jet luminosity in the 0.5−10.0 keV range of $L_j > 2{\times}10^{31}$ ergs s^{-1} (1σ limit). Equipartition arguments ($B \propto L^{2/7}\mathsf{V}^{-2/7}$, $E \propto B^2\mathsf{V}$) then imply a magnetic field in the jet of $B_j > 42\ (1{+}\mu)^{2/7}\ \phi^{-2/7}\ \mu$G and an energy of $E_j > 4.4{\times}10^{41}\ (1{+}\mu)^{4/7}\ \phi^{3/7}$ ergs. Here, μ is the ratio of ion to electron energy and ϕ is the filling factor in the jet. We note that these represent very conservative lower limits on B_j and E_j, as the total emission from the jet can have a significant contribution at lower energies. Using the above limit on B_j, the corresponding synchrotron lifetime for particles emitting at 2 keV is $t_j < 100\ (1{+}\mu)^{-3/7}\ \phi^{3/7}$ yr and implies a velocity in the jet of $v_j > 1{,}000\ (1{+}\mu)^{3/7}\ \phi^{-3/7}$ km s^{-1}.

For the Crab and Vela, the nebular magnetic field has been estimated to be ∼100's μG (e.g., Aharonian et al., 2004; Pavlov et al., 2001a). Similar fields have also been found for the large-scale jet in Vela (Pavlov et al., 2003). These are consistent with our derived fields above, suggesting the presence of similar confining pressures. The size and energetics of the nebula surrounding PSR B1046−58 are similar to those of Vela, as expected if these properties are also related to their similar spin-down energies $\dot{E}$. In contrast, the nebula surrounding PSR B1509−58 (with a smaller age and higher $\dot{E}$, see Gaensler et al., 2002, and Table 4.2) shows much smaller equipartition fields (∼8 μG) and larger size, pointing to a smaller confining pressure.

A fast-moving pulsar?

An alternate argument for an asymmetric nebula involves the confinement of the pulsar wind due to the ram pressure of a fast-moving pulsar (e.g., Gaensler et al., 2004). In this case, the body of the nebula would represent the expected X-ray tail aligned with the bow shock axis in the direction opposite to the pulsar proper motion. The implied position angle in the plane of the sky of the proper motion would be ≈310° (measured east of north). Recent *Chandra* observations of the Geminga pulsar revealed a somewhat similar morphology for its PWN (Pavlov et al., 2005; de Luca et al., 2006) which is likely to arise due the high space velocity of the pulsar.

In the case of a high space velocity, the confining pressure for the nebula is given by $\mathsf{P} = \rho V^2$, where ρ is the ambient density and V is the pulsar's speed. For cosmic abundances and a number density n_0 in the ambient medium we get $\rho = 1.37 n_0 m_H = 2.3{\times}10^{-24}\ n_0$ g cm^{-3}, where n_0 is in units of 1 cm^{-3}. Our above estimate for P results in a velocity of $V \gtrsim 190\ n_0^{-1/2}$ km s^{-1}. Such a velocity would agree with estimates for other bow-shock nebulae (e.g., Chatterjee & Cordes, 2002) and the expected distribution of pulsar velocities at birth (Arzoumanian et al., 1994; Faucher-Giguère & Kaspi, 2006). The proper motion for the pulsar in this case would be $\gtrsim 0\farcs015\ d_{2.7}^{-1}$ yr^{-1} and could be detected by radio interferometry. We note that a bow-shock interpretation for the X-ray morphology would differ from the static PWN interpretation favoured to explain the non-detection of an extended radio nebula (Stappers et al., 1999). A consistent bow-shock interpretation in both radio and X-rays is possible if the undetected radio nebula is unresolved with $r_{s,radio} \lesssim 10''$ and has a low efficiency of $\eta_R \sim 10^{-6}$, which results in estimates from the radio observations of $V \sim 250$ km s^{-1} and $n_0 \sim 0.1$ cm^{-3} (Stappers et al., 1999).

As suggested above, the structures observed in the body of the nebula can represent emission due to particles left behind after the passage of the pulsar for a large enough velocity. For $V > 190$ km s^{-1}, the time taken by the pulsar to travel the observed distance is $< 540\ d_{2.7}^2$ yr. Synchrotron lifetimes matching this limit require magnetic fields of $B \gtrsim 20\ \mu$G at 1 keV. This is consistent with the equipartition field expected to hold in the vicinity of the pulsar given the uncertainties in our estimates above. Even in this interpretation, the emission from the body and the north clump could also contain contributions from high velocity outflows.

As for the nature of the north clump at a radius $\approx 3''$ from the pulsar "ahead" of the bow, it is not expected to arise due to shocked ambient medium. For example, at a velocity $V = 190\ d_{2.7}^{-1}$ km s^{-1} and density $n_0 = 1$ cm^{-3}, the medium is expected to have a temperature $kT \sim 0.07 n_0^{-1}$ keV. The luminosity is expected to be $L_X \sim \Lambda n_0^2 \mathsf{V}'$ ergs s^{-1} $\sim 10^{28} n_0^2 d_{2.7}^3$ egs s^{-1}, where $\Lambda \sim 1.3{\times}10^{-24} n_0^{-1/2}$ ergs cm^3 s^{-1} is the cooling function at $kT \sim 0.07 n_0^{-1}$ keV and $\mathsf{V}' \sim 7{\times}10^{51} d_{2.7}^3$ cm^3 is the volume of the shocked gas within $3''$ of the pulsar (see, e.g., Rybicki & Lightman, 1979; Gaensler et al., 2004).

The implied absorbed flux at Earth is then much smaller than the measured values. Therefore, additional observations are needed to confirm the presence of the north clump and its association to the system.

6.6.3 PSR B1046−58 and 2EG J1049−5827

Although not confirmed, an association between PSR B1046−58 and 2EG J1049−5827 has been proposed in light of, among other things, their positional coincidence, possible γ-ray pulsations, and spectral and energetic properties of the γ-ray pulsar (Fierro, 1995; Pivovaroff et al., 2000; Kaspi et al., 2000). 2EG J1049−5827 was found to have a pulsed γ-ray flux above 400 MeV of $(2.5\pm0.6)\times10^{-10}$ ergs cm^{-2} s^{-1}, implying a γ-ray efficiency of $(9\pm2)\times10^{-3}$ (for 1 sr beaming and distance of 2.7 kpc, Kaspi et al., 2000). Unresolved, unpulsed γ-ray emission at the pulsar position was also found.

An extrapolation of the observed X-ray spectrum for PSR B1046−58 and its PWN (see Table 6.2) to energies >400 MeV predicts a flux of 0.7×10^{-13} ergs cm^{-2} s^{-1}, three orders of magnitude lower than that derived for the EGRET source. This is true for other well-established γ-ray pulsars (e.g., Thompson et al., 1999). Observations at higher X-ray energies (e.g., deep exposures using *RXTE*, *Suzaku*) can help determine whether PSR B1046−58 is indeed a γ-ray pulsar by detecting possible high X-ray energy pulsations and spectral characteristics consistent with those of 2EG J1049−5827.

We note the presence of a particularly hard X-ray source visible in the *Chandra* data, $\approx3\farcm3$ from the pulsar position at coordinates $\alpha_{2000}=10^h48^m05\fs74$ ($\pm0\fs15$) and $\delta_{2000}=-58°28'46''$ ($\pm2\farcs4$). The source is coincident with "Src 4" in Pivovaroff et al. (2000); see also Figure 6.4. A total of 164±15 counts were detected from this source and its spectrum is well described by a non-thermal power-law model with $N_H = (0.7^{+0.4}_{-0.2})\times10^{22}$ cm^{-2}, $\Gamma = 1.1^{+0.3}_{-0.2}$ and unabsorbed flux in the 0.5−10.0 keV band of $(1.2^{+0.5}_{-0.4})\times10^{-13}$ ergs s^{-1} cm^{-2} ($\chi^2 = 0.45$ for 5 d.o.f., 1σ errors). No counterpart for this source was found at other wavelengths and it lies within the 99% confidence error of 2EG J1049−5827. This suggests that the observed γ-ray emission could have

contributions from more than one source. Higher spatial resolution γ-ray observations with future missions may help to address this possibility.

We also find that the emission from the nebula dominates at high X-ray energies (see Table 6.1) over that of the pulsar. This argues for the unpulsed γ-ray emission associated with 2EG J1049−5827 to also arise, at least in part, from the nebula, as proposed for the Vela and Crab pulsars (Nolan et al., 1993; Kanbach et al., 1994; Fierro et al., 1998). We note that current ground-based γ-ray experiments have detected a large number of TeV sources that appear to be coincident with PWNe powered by Vela-like pulsars (see also the Appendix). Future observation with these telescopes (or space-based γ-ray missions such as *GLAST*) will be able to confirm whether PSR B1046−58 and/or its PWN are indeed γ-ray sources.

6.6.4 Non-detection of a Supernova Remnant

We do not detect emission from a supernova remnant (SNR) in the field containing PSR B1046−58. Following Gaensler et al. (2003), we can estimate the flux from a possible unseen remnant by scaling the emission observed from the Vela SNR. The emission from this remnant can be described by a two-component Raymond-Smith plasma with temperatures $kT_1 \approx 0.15$ keV and $kT_2 \approx 1$ keV (Lu & Aschenbach, 2000). The total unabsorbed luminosity in the 0.1–2.4 keV range is $2.2{\times}10^{35}$ ergs s^{-1} and the cooler component has a flux ≈10 times higher than the hot component. Scaling to a distance of 2.7 kpc, the unabsorbed fluxes for each component would be $f_1 = 2.3{\times}10^{-10}$ ergs s^{-1} cm^{-2} and $f_2 = 2.2{\times}10^{-11}$ ergs s^{-1} cm^{-2}, respectively.

The expected ACIS-S[3] count rate predicted by the WebPIMMS tool[4] is <2.6 counts s^{-1} (on-axis) for absorbing columns $>5{\times}10^{21}$ cm^{-2}. Scaling the size of the

[3] The EPIC-MOS data provide less constraining limits for this emission due to their lower sensitivity and higher background levels. The EPIC-PN data had a much smaller exposure time and limited field of view.

[4] http://heasarc.gsfc.nasa.gov/Tools/w3pimms.html

Vela SNR ($\approx 8^\circ$ at 300 pc, Lu & Aschenbach, 2000), we would expect a shell with a radius of $\approx 26'$ at 2.7 kpc. This size is larger than the ACIS-S (and EPIC-MOS) field of view. However, parts of the remnant might be visible in the present data given the uncertainties in the spatial distribution of the remnant and direction of motion of the pulsar. Assuming emission areas for the remnant proportional to having a shell thickness >20% of its radius (as a general estimate for shell-like remnants), the expected surface brightness density is $\lesssim 0.8 \times 10^{-6}$ counts s^{-1} arcsec^{-2}. This is somewhat lower than the ACIS-S background level during the observation, estimated to be $\approx (2-6) \times 10^{-6}$ counts s^{-1} arcsec^{-2} (accounting for vignetting at large off-axis angles).

It is then possible that a remnant with similar properties to that of the Vela remnant might be present and it is undetected by these observations. The lack of radio or X-ray emission from the SNR has also been attributed to an initial fast expansion into a low-density cavity (e.g., Braun et al., 1989). This expansion is followed by a collision with a dense surrounding shell of stellar wind material from the progenitor where the emission fades rapidly and energy is dissipated through radiative shocks.

6.7 Summary

We have discovered that PSR B1046−58 is both an X-ray source and powers a high energy nebula. The emission from the system is faint and consistent with an overall non-thermal origin. However, spatially resolved spectroscopy suggests that soft (possibly thermal) emission from the pulsar is present. The nebula is mostly one-sided and various scenarios for its formation were explored.

Chapter 7

Conclusions and Future Work

7.1 High Magnetic Field Radio Pulsars

The properties of two high magnetic field radio pulsars were studied in this thesis. In the case of PSR B0154+61, no emission was detected in the single *XMM–Newton* observation available for this object. The upper limits for its blackbody temperature and luminosity are consistent with the possibility that it still emits standard cooling radiation below our detection limit. In addition, its non-detection implies that no additional source of heating is present down to our detection limits due to, e.g., a decaying magnetic field as is the case in persistent magnetars (and has been suggested to also be the case for thermally emitting isolated neutron stars of spin characteristics similar to those of PSR B0154+61).

In the case of PSR J1119−6127, we have discovered thermal emission from this source with unusual properties: it has a temperature higher than expected from standard cooling models and is highly pulsed. These properties have important implications for our understanding of the production and emission of thermal radiation from the surface of neutron stars, which can in turn be a valuable tool to infer the internal properties of these objects. In this case, the large pulsations imply that the emission arises from a small fraction of the surface in order to not be broadened due to gravitational light bending and/or beaming of the emission is taking place. The measured temperature can also imply that the radiation is being channelled to polar

regions on the surface due to a high magnetic field, resulting in a higher temperature than expected. It is possible that these properties can be explained as being due to the effects of a large magnetic field on the thermal conductivity of the surface. Future detailed modeling of this effect will address this issue. In addition, PSR J1119−6127 is now the radio pulsar with smallest characteristic age from which thermal emission has been detected and while the temperature is high (possibly from the above mechanisms), the luminosity is consistent with arising from standard cooling mechanisms in the interior.

The fact that no persistent radio pulsar with an inferred magnetic field $>10^{13}$ G has shown firm evidence for enhanced high energy emission due to field decay (or magnetar-like bursts) poses a great challenge to our understanding of the evolution and emission processes in neutron stars. This has led to many ideas and theories being put forward to explain the behaviour of these radio pulsars, including the possibility that they are magnetars in quiescence, that the internal high magnetic field can be screened by outer currents in the first $\sim 10^3$ yrs of the star's life (during which it will exhibit the properties of a normal radio pulsar), and that the presence of condensed matter on the surface can enhance radio emission at high magnetic fields and low temperatures. Future observations and continuing theoretical work hold the key to answer these questions.

On the observational side, an *XMM–Newton* observation of another high magnetic field radio pulsar, PSR B1916+14, is planned for this year. While this pulsar has an inferred magnetic field lower than those of the HBRPs studied here (1.6×10^{13} G), it lies at an estimated distance of 1.9 kpc and in a region of low interstellar absorption, allowing for any enhance thermal emission to be detected. X-ray observations of additional, known sources where the properties have not been properly constrained (e.g., PSR J1718–3718; Kaspi & McLaughlin, 2005) should be carried out with current or future missions. Additional observations of PSR J1119−6127 would also be helpful in further constraining the observed emission characteristics (pulsed fraction, temperature, etc). In addition, searches for new pulsars will likely produce new candidates

that can also be observed.

7.2 Magnetar variability

The detailed study of the long-term evolution of 4U 0142+61 showed that changes in all of its emission characteristics are present. Pulse profile and pulsed fraction changes are interpreted as representing changes in the emission geometry, while spectral changes point to differences in the emission mechanism. In 4U 0142+61, a spectral softening and evolution towards more sinusoidal profiles is seen before bursts were detected from the source in 2006. The period of increased burst activity in 2006–2007 is seen to be accompanied by an increase in total flux of ≈10%, a hardening of the spectrum close to the burst epochs, and an end of the pulse profile evolution towards more sinusoidal shapes.

The above behaviour agrees with the predictions made by the twisted magnetosphere model of these sources, where the magnetosphere acquires an external twist due to (possibly) displaced regions on the surface (where the magnetic field is thought to be anchored) because of the decay and unwinding of the internal magnetic field. An increased twist angle is then thought to result in an increased upscattering of low-energy photons and produce a brighter, harder spectrum. If the angle is large enough it is thought to result in bursts, as observed for 4U 0142+61. The main spectral changes are observed to occur at high energies and no long-term effects are observed associated with specific bursts. It is therefore unlikely that long-term recovery regions, such as the crust, have been significantly affected and the main changes observed after the bursts are probably magnetospheric in nature.

One property that currently cannot be explained with a single model is the continuous increase of the pulsed fraction (and thus pulsed flux) throughout the observations independent of other emission properties. The twisted magnetosphere model generally predicts that larger twist angles will produce larger pulsed fractions and can account for the increase observed after the bursts. However, the increase in pulsed fraction seen before the bursts that is accompanied by more sinusoidal profiles and a

softer spectrum is then hard to explain in this context. This suggests that additional emission mechanisms are likely to be present that contribute to the total observed properties with different strengths over time.

Variability in the spectrum and pulse properties of magnetars is now seen to be a common occurrence. In the case of 4U 0142+61, we see that the high quality data reveal variations of low amplitude. As magnetars have been shown to be very active sources, the changes in their emission provide important information on the physical processes at work and continuous monitoring of their properties is thus important. These sources will continue to be observed with *RXTE* on a regular basis until the satellite stops operations (possibly early 2009). After the last, large burst observed from 4U 0142+61 (February 2007) no other bursts have been detected. The source will be observed two more times with *XMM–Newton* in the coming year and if the bursting activity continues, additional observations will be proposed.

7.3 Vela-like pulsars and their nebulae

The high spatial resolution available with *Chandra* allowed us to discover an arc-second nebula powered by the radio pulsar PSR B1046−58. The overall size and energetics of the X-ray nebula are consistent with those produced by other pulsars with similar spin characteristics. The overall emission from the system is consistent with a non-thermal origin, suggesting that magnetospheric emission from the star and synchrotron emission from the nebula are present. However, that the brightest region of the nebula coincides that the radio position of the pulsar suggests that softer, possibly thermal emission from the surface of the star is present. The upper limit for such emission is consistent with the presence of cooling radiation. The low number of counts allows only for a coarse limit on any X-ray pulsations. The shape of the nebula is highly asymmetric, extending to the south-east of the pulsar position. In the case that the pulsar does not have a high space velocity, the asymmetry can be caused by doppler boosting, an intrinsically asymmetric pulsar wind, or highly

collimated outflows. If the pulsar has a high space velocity, the morphology of the nebula suggests a velocity that is consistent with those observed in other objects.

This source now joins the growing number of young, energetic pulsars powering faint, arc-second scale X-ray nebulae, where a combination of high spatial resolution and high sensitivity are needed to detected them. In addition, the fact that many of these objects are possible γ-ray sources (see also the Appendix) has sparked great interest in their production and emission characteristics. Ground-based experiments such as *HESS* and *VERITAS* are expected to detect more of these objects, and together with space-based observatories such as *GLAST*, they will give the γ-ray sky unprecedented coverage.

7.4 Observational properties of neutron stars

In this thesis we have shown how the observational characteristics of NSs can be used to infer their physical properties. The wide range of behaviours observed here illustrate the large number of physical processes associated with these objects, which in turn provide valuable insights into how matter behaves in these circumstances. In general, the observational effects of three main processes on the observed properties of NSs have been studied: a) the internal cooling mechanisms of young stars, which result in observable thermal emission from the surface; b) the processes associated with a rapidly-rotating magnetic field, resulting in non-thermal emission from the magnetosphere as well as an outflowing wind of relativistic particles; and c) the effects of an extremely large magnetic field on both the interior and exterior properties of NSs. While our general picture of how these processes work seems to be right, we have shown that many questions and details still need to be studied and understood (e.g., the effects of an atmosphere and magnetic field on the emergent radiation, the detailed nature of observed changes in magnetar emission). In addition, as the properties of many objects are studied in detail, the lines separating their (maybe) simplified classifications is becoming less clear (e.g., are HBRPs an independent class of NSs from magnetars? can the old, thermally-emitting neutron stars be thought

of as old magnetars?). Further observational and theoretical work will allow us to develop a unifying picture of the many manifestations of NSs.

Appendix
A *Chandra* observation of the Vela-like pulsar PSR B1823–13

Here we present preliminary results obtained from a *Chandra* observations of the Vela-like pulsar PSR B1823–13. An association between the PWN powered by this pulsar and the very bright TeV source HESS J1825−137 has been previously claimed in light of *XMM–Newton* results of the properties of the nebula at X-ray energies. The goal of this work is to assess the likelihood of this association in light of the high spatial resolution data available with *Chandra*. We find that arguments previously used are harder to sustain using the improved information on the nebula and the issue is far from settled.

A.1 Introduction

Traditionally, the energetics and emission mechanisms of rotation-powered pulsars have been studied primarily at radio and X-ray wavelengths. The stars themselves radiate X-rays in the form of thermal cooling emission from the surface and non-thermal emission from the magnetosphere. Young, energetic pulsars are believed to emit a large fraction of their rotational energy in the form of a relativistic $e^{\pm}$ wind. The confinement of this wind by the surrounding medium results in a synchrotron-emitting pulsar wind nebula (PWN). Very recently, the High Energy Stereoscopic System (HESS) has opened a new window on pulsar wind physics. Thanks to its unprecedented sensitivity to TeV γ-rays, HESS has detected multiple PWNe, demonstrating that TeV emission may be ubiquitous for these systems (de Jager, 2005). This extraordinary emission is believed to arise from the interaction of accelerated particles with ambient photons (e.g., from the cosmic microwave background) via

inverse-Compton scattering. Understanding how these sources accelerate particles to such high energies remains an important topic of neutron star astrophysics.

PSR B1823−13 has a period of 101 ms and period derivative of 7.5×10^{-14} s s^{-1}. The derived spin properties place the source into the Vela-like category, with a characteristic age of 21.4 kyr, dipole magnetic field strength of 2.8×10^{12} G and spin-down luminosity of 2.8×10^{36} ergs s^{-1} (Clifton et al., 1992). The dispersion measure towards the pulsar suggests a distance of 3.9±0.4 kpc (Cordes & Lazio, 2002). Gaensler et al. (2003) presented the results from an *XMM–Newton* observation, which showed that the pulsar powers a PWN. The nebula has a compact component close to the radio position of the pulsar ≈30′ in size, as well as an extended component seen to extend primarily to the south and detected out to a distance of ≈5′ from the pulsar. The observed asymmetry was attributed to a possible interaction between the PWN and the reverse shock of the supernova remnant. A spectral analysis suggested a non-thermal origin for the emission with power-law indices of $\Gamma_{CN} \approx 1.6$ and $\Gamma_{EN} \approx 2.3$, where *CN* and *EN* refer to the compact and extended components of the nebula, respectively.

The HESS experiment detected emission from a very bright and extended TeV source, HESS J1825−137, located 12′ south of the pulsar position. This source has a size of ≈50′ and a power-law index of $\Gamma_{TeV} \approx 2.4$ (Aharonian et al., 2005). An association with PSR B1823−13 and its X-ray PWN was proposed in light of the longer lifetime of ICS-emitting electrons (resulting in a larger TeV size) and the similar power-law indices of the extended nebular components (Aharonian et al., 2005; de Jager & et al., 2005). In addition, a steepening of the power-law index of $\Gamma_{TeV} \approx 1.8 - 2.5$ with increasing distance in the direction of the pulsar was found for HESS J1825−137 (the first time this has been measured for a TeV source), strengthening the argument for an association with PSR B1823−13 (Aharonian et al., 2006).

Here we summarize the results obtained from a *Chandra* observation of the system, which reveals the true inner structure of the nebula and allows for a more accurate estimate of the spectral parameters of the pulsar and PWN independent of each other. The revised properties of the system pose additional challenges to the association between the X-ray nebula and HESS J1825−137 and to our understanding of how the

TeV emission can be produced.

A.2 Observation and Data Analysis

PSR B1823−13 was observed with *Chandra* on 2002 October. The radio position of the pulsar fell on the back-illuminated ACIS-S3 chip. The detector was operated in full-frame mode, which results in a time resolution of 3.2 s and does not allow us to search for possible X-ray pulsations from PSR B1823−13. The data were reduced using standard techniques and eliminating times of high background resulted in an effective exposure time of 30 ks.

A.2.1 Imaging Analysis

The pulsar and extended regions of the PWN fell on the S3 and S2 chips of the ACIS instrument. Figure A.1 shows the exposure-corrected *Chandra* field of the system. A number of unrelated point sources are visible that were included in the *XMM–Newton* region of the PWN as they were unresolved. In addition, the *Chandra* counterpart of the compact nebula found with *XMM–Newton* is seen to be smaller than estimated. This is mainly due to the fact that an unrelated point source is present in the field $\approx 15''$ from the radio position of the pulsar and the larger PSF of *XMM–Newton* was not able to separate the emission from both sources.

The structures immediately surrounding the radio position are $\approx 8'' \times 4''$ in size and we derive an overall size for the compact PWN component of $\approx 30'' \times 15''$. The brightest region of emission is coincident with the radio coordinates of the pulsar. In addition, the inner $\approx 8'' \times 4''$ region appears to be asymmetric about the pulsar with the south-western side being longer and brighter (at the $\approx 2\sigma$ level) with a similar asymmetry being evident in the fainter emission further out (see Figure A.1, right). Extended emission can be seen in the field, but it also appears to be concentrated to the south-west rather than symmetrically south of the pulsar. Faint PWN regions $\approx 4'$ south of the pulsar fell on the S2 chip.

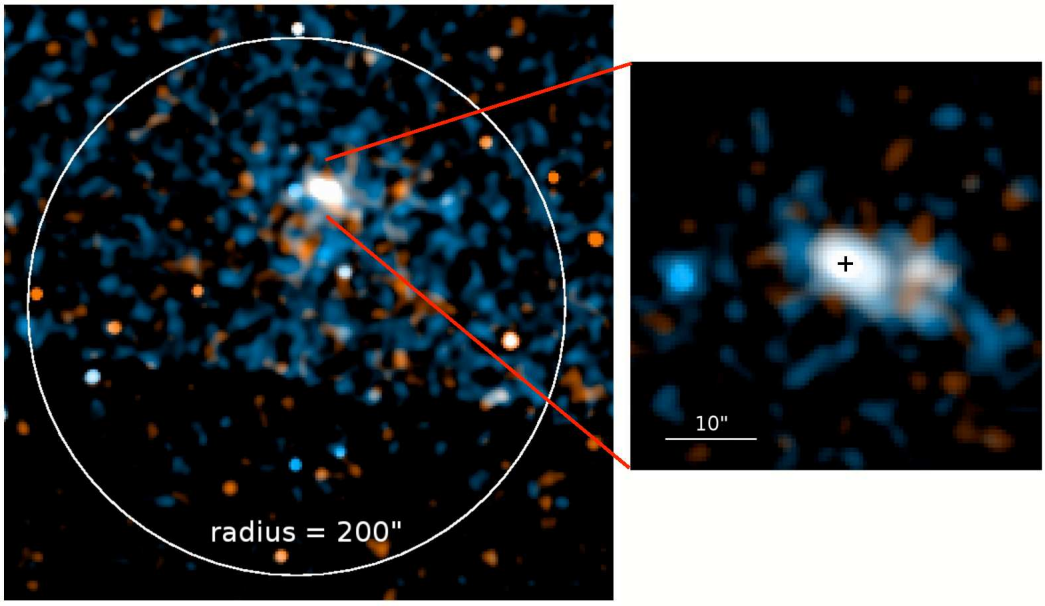

Figure A.1: *Left*: *Chandra* image of the field containing PSR B1823–13 smoothed with a gaussian with $\sigma = 4''$. The white circle ($200''$ radius) shows the size and position of the extended features detected with *XMM–Newton*. *Right*: Central $45''$ of the PWN smoothed with a gaussian with $\sigma = 1''$. The plus sign marks the radio position of the pulsar. The images are colour coded with 0.5–2.0 keV energies in red and 2.0–10.0 keV in blue.

A.2.2 Spectral Analysis

We extracted a spectrum from the "core" of the nebula (coincident with the radio position of the pulsar) and the extended components at various radii. For the core region the spectrum was grouped to have a minimum of 15 cts bin^{-1}, for all others a minimum of 20 cts bin^{-1} was used. A power-law model provided a good fit to all the regions with the available data. Table A.1 shows the number of counts collected and the resulting spectral parameters (errors shown are the 68% confidence range). The fits were performed simultaneously and the value of the interstellar absorption, N_H, was held constant at the best-fit value for the combined fits. The total unabsorbed X-ray luminosity of the system in the 0.5–10 keV range is $\approx 2\times10^{33}$ ergs s^{-1}, with $\approx$30% of this emission arising from the inner $\approx 30''$ of the nebula.

Table A.1: *Chandra* power-law fits to the emission from PSR B1823−13 and its PWN

Region	0.5–10 keV counts	Γ^a	f^b (ergs s^{-1} cm^{-2})
Core ($1''$ radius)	124±11	1.5±0.1	0.74×10^{-13}
Compact ($16''\times7''$ radius − core)	365±20	1.06±0.07	2.7×10^{-13}
Extended1 ($1.5'$ radius − compact)	1170±80	1.55±0.15	6.2×10^{-13}
Extended2 ($1'\times4'$, S2 chip)	351±70	$1.8^{+0.3}_{-0.2}$	2.6×10^{-13}

[a] Interstellar absorption frozen to the best fit value of $N_H = 7\times10^{21}$ cm^{-2}.
[b] Unabsorbed X-ray flux in the 0.5–10.0 keV range.

A.3 Discussion

A.3.1 Revised Properties

The AO-3 Chandra observation of PSR B1823−13 partially agrees with previous XMM results: the PWN shows a compact region close to the pulsar position and an asymmetric extended component. However, the improved resolution revealed that some of the extended PWN emission has been resolved into unrelated point sources, the compact region is a factor of $\approx$4 smaller than estimated, the extended component

appears to be confined to the south-west of the pulsar, and significant spectral variations within the PWN appear to be present with photon indices lower than previously estimated.

Based on the *XMM–Newton* size of the compact PWN and assuming a static case, the estimated nebular magnetic field was ≈10 μG. In the static case, the revised size for the compact nebula as seen with *Chandra* (assuming it can be used as an upper limit for the location of the wind termination shock, $R_s \approx 4''$) implies a revised value for the nebular magnetic field of $B_n = \sqrt{\dot{E}/R_s^2 c} \approx 40$ μG.

The spectral steepening seen in the X-ray nebula supports the interpretation of energy losses of the accelerated electrons due to synchrotron cooling. However, the derived photon indices are lower than was estimated from *XMM–Newton*, implying a harder spectrum. Although the *Chandra* data favour a lower N_H than found with *XMM–Newton*, fixing its value to agree with that one (N_H=1×10^{22} cm^{-2}) produces indices in the PWN of 1.3±0.1 to $2.0^{+0.4}_{-0.3}$ (1σ errors). These values are still lower than those estimated before, probably due to contamination from the pulsar itself and unrelated point sources.

The core of the PWN shows a steeper spectrum than its immediate surroundings. This region could have considerable emission from the pulsar itself, suggesting that additional soft emission might be present in its spectrum, not unreasonable given its small characteristic age and the possibility of having thermal emission from initial cooling. Fitting the core emission with a blackbody plus power-law model gives temperatures of $kT \approx 0.1$–0.2 keV, small emitting radius observed at infinity of $R^{\infty} < 2$ km (at a distance of 4 kpc), and photon index of $\Gamma \approx 1.2$. While these values are not well constrained due to the small number of counts available, the implied temperature is close to those predicted by standard cooling models for the pulsar's characteristic age. However, the small radius might suggest that atmospheric models are needed to fit the data (which, in the case of low-elements, results in a larger radius and lower temperature) or that the emission arises from a localized hot spot (possibly heated by the back-flow of accelerated particles in the magnetosphere striking the surface).

A.3.2 Implications for HESS J1825−137

One of the original arguments used to support the association between PSR B1823−13 and HESS J1825−137 was the fact that for a nebular magnetic field of $B_n \approx 10$ μG, the different synchrotron and ICS lifetimes of the accelerated electrons imply a size ≈6× larger for the γ-ray nebula ($R_\gamma / R_X \propto B_n^{-1/2}$). However, the revised estimate for B_n results in a smaller radius for the γ-ray nebula, making it harder to account for its observed large size. Independent of this, the larger nebular field implies smaller sizes at all energies and makes it difficult to account for the size of the extended features in the case of a static nebula.

Pavlov et al. (2007) have measured the proper motion of the pulsar to be (440±50) km s^{-1} at a position angle of ≈10° south of east[1]. The direction of motion then rules out the possibility that the TeV emission maps the location of trailed electrons due to the passage of the pulsar. In addition, it has been proposed that the extension of both the X-ray and γ-ray nebula to the south of the pulsar is due to an asymmetric interaction with the reverse shock of the supernova remnant (Gaensler et al., 2003; Aharonian et al., 2005). However, such remnant has not been detected at any wavelength (including the *Chandra* observation analyzed here) and the origin for such drastic asymmetry is difficult to explain.

Furthermore, current modeling of the γ-ray nebula takes into account the injection conditions at the PWN shock front and the subsequent propagation of these electrons. The observed properties of HESS J1825−137 require an electron injection spectrum >2, which translates into an observed photon index of Γ>1.5 (Lemière & de Jager 2007, in preparation). This places a strong constraint on the spectral characteristics that are expected from the X-ray nebula. However, the spectrum of the inner region of the nebula, which can be used as an estimate for the spectrum at the shock front,

[1] Pavlov et al. (2007) also present an analysis of the *Chandra* data used here and obtain almost identical results to ours.

appears to have a photon index $\Gamma<1.5$, contrary to what is required by these models. As there is a large degeneracy between Γ and N_H, observations having a high enough signal-to-noise ratio to determine these values with high confidence are needed.

A.4 Conclusion

The high spatial resolution of the *Chandra* data allowed for a more accurate determination of the X-ray properties of PSR B1823−13 and its PWN. A smaller size of the inner component of the nebula is found, mainly due to a nearby point source that was unresolved in the *XMM–Newton* data of the PWN. In addition, the spectral properties of different parts of the system were derived. We find a possible contribution from thermal emission from the surface of the star, as well as power-law photon indices that increase with increasing distance from the pulsar but are also lower than estimated from previous observations.

The available data have raised many questions regarding our current understanding and interpretation of the observed properties (e.g., the large size of the γ-ray nebulae, its large displacement to the south of the pulsar, the flatter spectral index of the X-ray nebula than needed to account for the γ-ray spectrum). It seems that, currently, the steepening of the γ-ray spectrum as expected from a correspondence with the X-ray steepening is the strongest argument made to support an association between PSR B1823−13 and HESS J1825−137. Given that richness of the γ-ray data allow for HESS J1825−137 to be used as a prototype for the study of PWNe powered by Vela-like pulsars, further observational and theoretical work of this system are needed.

References

Aharonian, F., et al. 2004, ApJ, 614, 897

Aharonian, F., et al. 2006, A&A, 460, 365

Aharonian, F. A., et al. 2005, A&A, 442, L25

Alpar, M. A. 2001, ApJ, 554, 1245

Arzoumanian, Z., Nice, D. J., Taylor, J. H., & Thorsett, S. E. 1994, ApJ, 422, 671

Baade, W., & Zwicky, F. 1934, Proc. Nat. Acad. Sci., 20, 259

Baring, M. G. 2004, in IAU Symposium, Vol. 218, Young Neutron Stars and Their Environments, ed. F. Camilo & B. M. Gaensler, 267

Baring, M. G., & Harding, A. K. 2001, ApJ, 547, 929

Becker, W., & Aschenbach, B. 2002, in Neutron Stars, Pulsars, and Supernova Remnants, ed. W. Becker, H. Lesch, & J. Trümper, 64

Beloborodov, A. M., & Thompson, C. 2007, ApJ, 657, 967

Bhattacharya, D., & Soni, V. 2007, ArXiv e-prints, 705

Blazek, J. A., et al. 2006, ApJ, 652, 1523

Braun, R., Goss, W. M., & Lyne, A. G. 1989, ApJ, 340, 355

Brisken, W. F., Thorsett, S. E., Golden, A., & Goss, W. M. 2003, ApJ, 593, L89

Buccheri, R., et al. 1983, A&A, 128, 245

Bucciantini, N. 2007, AdSpR, in press (astro-ph/0702084)

Camilo, F., et al. 2004, ApJ, 616, 1118

Camilo, F., et al. 2000, ApJ, 541, 367

Camilo, F., et al. 2006, Nature, submitted, (astro-ph/0605429)

Camilo, F., Ransom, S. M., Halpern, J. P., & Reynolds, J. 2007a, ApJ, 708, accepted (arXiv:0708.0002)

Camilo, F., et al. 2007b, ApJ, 659, L37

Campana, S., et al. 2007, A&A, 463, 1047

Cardall, C. Y., Prakash, M., & Lattimer, J. M. 2001, ApJ, 554, 322

Carroll, B. W., & Ostlie, D. A. 1996, An introduction to modern astrophysics (Reading, Mass. : Addison-Wesley Pub., c1996.)

Caswell, J. L., McClure-Griffiths, N. M., & Cheung, M. C. M. 2004, MNRAS, 352, 1405

Chang, P., Arras, P., & Bildsten, L. 2004, apjl, 616, L147

Chatterjee, P., Hernquist, L., & Narayan, R. 2000, ApJ, 534, 373

Chatterjee, S., & Cordes, M., J. 2002, ApJ, 575, 407

Cheng, K. S., Ho, C., & Ruderman, M. 1986, ApJ, 300, 500

Cheng, K. S., & Zhang, L. 1999, ApJ, 515, 337

Clifton, T. R., et al. 1992, MNRAS, 254, 177

Contopoulos, I., Kazanas, D., & Fendt, C. 1999, ApJ, 511, 351

Contopoulos, I., & Spitkovsky, A. 2006, ApJ, 643, 1139

Cordes, J. M., & Lazio, T. J. W. 2002, ArXiv Astrophysics e-prints, astro-ph/0207156

Crawford, F., et al. 2001, ApJ, 554, 152

Crusius-Wätzel, A. R., Kunzl, T., & Lesch, H. 2001, ApJ, 546, 401

Cutri, R. M., Skrutskie, M. F., van Dyk, S., & et al. 2003, 2MASS All-Sky Catalog of Point Sources (Pasadena: Infrared Processing and Analysis Center)

de Jager, O. C. 2005, in American Institute of Physics Conference Series, Vol. 801, Astrophysical Sources of High Energy Particles and Radiation, ed. T. Bulik, B. Rudak, & G. Madejski, 298, astro-ph/0602078

de Jager, O. C., & et al. 2005, in International Cosmic Ray Conference, Vol. 4, International Cosmic Ray Conference, 239, astro-ph/0510457

de Luca, A., et al. 2006, A&A, 445, L9

den Hartog, P. R., et al. 2007, Ap&SS

Dhillon, V. S., et al. 2005, MNRAS, 363, 609

Dib, R., Kaspi, V., Gavriil, F., & Woods, P. 2006, The Astronomer's Telegram, 845, 1

Dib, R., Kaspi, V. M., & Gavriil, F. P. 2007, ApJ, in press

Dib, R., Kaspi, V. M., & Gavriil, F. P. 2007, ApJ, submitted (astro-ph/0706.4156)

Duncan, R. C., & Thompson, C. 1992, ApJ, 392, L9

Durant, M., & van Kerkwijk, M. H. 2006a, ApJ, 650, 1070

Durant, M., & van Kerkwijk, M. H. 2006b, ApJ, 650, 1082

Durant, M., & van Kerkwijk, M. H. 2006c, ApJ, 652, 576

Ertan, Ü., et al. 2007a, Ap&SS, 59

Ertan, Ü., Erkut, M. H., Ekşi, K. Y., & Alpar, M. A. 2007b, ApJ, 657, 441

Faucher-Giguère, C.-A., & Kaspi, V. M. 2006, ApJ, 643, 332, in press

Fernández, R., & Thompson, C. 2007, ApJ, 660, 615

Fierro, J. M. 1995, Ph.D. thesis, Stanford University

Fierro, j. M., Michelson, P. F., Nolan, P. L., & Thompson, D. J. 1998, ApJ, 494, 734

Frail, D. A., & Scharringhausen, B. R. 1997, ApJ, 480, 364

Gänsicke, B. T., Braje, T. M., & Romani, R. W. 2002, A&A, 386, 1001

Gaensler, B. M., et al. 2002, ApJ, 569, 878

Gaensler, B. M., et al. 2003, ApJ, 588, 441

Gaensler, B. M., et al. 2003, ApJ, 588, 441

Gaensler, B. M., & Slane, P. O. 2006, ARAA, 44, 17

Gaensler, B. M., et al. 2000, MNRAS, 318, 58

Gaensler, B. M., et al. 2004, ApJ, 616, 383

Gavriil, F. P., Dib, R., Kaspi, V. M., & Woods, P. M. 2007a, The Astronomer's Telegram, 993, 1

Gavriil, F. P., Dib, R., Kaspi, V. M., & Woods, P. M. 2007b, ApJ, in preparation

Gavriil, F. P., & Kaspi, V. M. 2002, ApJ, 567, 1067

Gavriil, F. P., & Kaspi, V. M. 2004, ApJ, 609, L67

Geppert, U., Küker, M., & Page, D. 2006, A&A, 457, 937

Geppert, U., & Rheinhardt, M. 2006, A&A, 456, 639

Gil, J. A., & Sendyk, M. 2003, ApJ, 585, 453

Gold, T. 1968, Nature, 218, 731

Goldreich, P., & Julian, W. H. 1969, ApJ, 157, 869

Gonzalez, M., & Safi-Harb, S. 2005, ApJ, 619, 856

Gonzalez, M. E., et al. 2007a, ApJ, submitted, (arXiv:astro-ph/0708.2756)

Gonzalez, M. E., et al. 2005, ApJ, 630, 489

Gonzalez, M. E., et al. 2007b, Ap&SS, 308, 89

Gonzalez, M. E., Kaspi, V. M., Lyne, A. G., & Pivovaroff, M. J. 2004, ApJ, 610, L37

Gonzalez, M. E., Kaspi, V. M., Pivovaroff, M. J., & Gaensler, B. M. 2006, ApJ, 652, 569

Gotthelf, E. V. 2003, ApJ, 591, 361

Gotthelf, E. V., & Halpern, J. P. 2007, Ap&SS, 308, 79

Güver, T., Özel, F., & Göğüş, E. 2007, ApJ, submitted (astro-ph/0705.3982)

Güver, T., Özel, F., Göğüş, E., & Kouveliotou, C. 2007, ApJ, submitted (astro-ph/0705.3713)

Halpern, J. P., Gotthelf, E. V., Camilo, F., & Seward, F. D. 2007, ApJ, 665, 1304

Harding, A. K. 2005, in American Institute of Physics Conference Series, Vol. 801, Astrophysical Sources of High Energy Particles and Radiation, ed. T. Bulik, B. Rudak, & G. Madejski, 241

Harding, A. K. 2006, private communication

Harding, A. K., Arzoumanian, Z., Gonthier, P., & Cordes, J. M. 2003, in Bulletin of the American Astronomical Society, Vol. 35, Bulletin of the American Astronomical Society, 633

Harding, A. K., Grenier, I. A., & Gonthier, P. L. 2007, Ap&SS, 309, 221

Harding, A. K., & Lai, D. 2006, Reports of Progress in Physics, 69, 2631

Harding, A. K., & Muslimov, A. G. 2001a, ApJ, 556, 987

Harding, A. K., & Muslimov, A. G. 2001b, ApJ, 556, 987

Harding, A. K., & Muslimov, A. G. 2002, ApJ, 568, 862

Helfand, D. J., Collins, B. F., & Gotthelf, E. V. 2003, 582, 783

Helfand, D. J., Gotthelf, E. V., & Halpern, J. P. 2001, ApJ, 556, 380

Hessels, J. W. T., et al. 2006, Science, 311, 1901

Hester, J. J., et al. 2002, ApJ, 577, L49

Hewish, A., et al. 1968, Nature, 217, 709

Heyl, J. S., & Hernquist, L. 2005, ApJ, 618, 463

Ho, W. C. G., et al. 2007, MNRAS, 375, 821

Hulleman, F., et al. 2001, ApJ, 563, L49

Hulleman, F., van Kerkwijk, M. H., & Kulkarni, S. R. 2004, A&A, 416, 1037

Ibrahim, A. I., et al. 2004, ApJ, 609, L21

Israel, G. L., et al. 2003, ApJ, 589, L93

Israel, G. L., Mereghetti, S., & Stella, L. 1994, ApJ, 433, L25

Johnston, S., et al. 1992, MNRAS, 255, 401

Juett, A. M., Marshall, H. L., Chakrabarty, D., & Schulz, N. S. 2002, ApJ, 568, L31

Kanbach, G., et al. 1994, A&A, 289, 855

Kaplan, D. L., & van Kerkwijk, M. H. 2005, ApJ, 635, L65

Kaplan, D. L., & van Kerkwijk, M. H. 2005, ApJ, 628, L45

Kaspi, V. M. 2007, Ap&SS, 308, 1

Kaspi, V. M., Dib, R., & Gavriil, F. P. 2006, The Astronomer's Telegram, 794, 1

Kaspi, V. M., et al. 2003, ApJ, 588, L93

Kaspi, V. M., et al. 2000, ApJ, 528, 445

Kaspi, V. M., & McLaughlin, M. A. 2005, ApJ, 618

Kaspi, V. M., Roberts, M. S. E., & Harding, A. K. 2004, in Compact Stellar X-ray Sources, ed. W. H. G. Lewin & M. van der Klis (UK: Cambridge University Press), in press (astro-ph/0402136)

Kaspi, V. M., Roberts, M. S. E., & Harding, A. K. 2006, Isolated neutron stars, ed. W. H. G. Lewin & M. van der Klis (Cambridge University Press, UK: Compact stellar X-ray sources), 279

Kaspi, V. M., et al. 2001, ApJ, 560, 371

Kern, B., & Martin, C. 2002, Nature, 415, 527

Komissarov, S. S. 2002, MNRAS, 336, 759

Kouveliotou, C., et al. 1994, Nature, 368, 125

Kouveliotou, C., et al. 1998, Nature, 393, 235

Kramer, M., et al. 2006, Science, 312, 549

Kramer, M., et al. 2007, MNRAS, 377, 107

Kuiper, L., Hermsen, W., den Hartog, P., & Collmar, W. 2006, ApJ, 645, 556

Kulkarni, S. R., & Frail, D. A. 1993, Nature, 365, 33

Lattimer, J. H., & Prakash, M. 2004, Science, 304, 536

Lattimer, J. M., & Prakash, M. 2000, PhR, 333, 121

Lattimer, J. M., & Prakash, M. 2001, ApJ, 550, 426

Lattimer, J. M., & Prakash, M. 2007, PhR, 442, 109

Lu, F. J., & Aschenbach, B. 2000, A&A, 362, 1083

Lyne, A. G., Pritchard, R. S., Graham-Smith, F., & Camilo, F. 1996, Nature, 381, 497

Lyutikov, M. 2002, ApJ, 580, L65

Lyutikov, M., & Gavriil, F. P. 2006, MNRAS, 368, 690

Manchester, R. N., Hobbs, G. B., Teoh, A., & Hobbs, M. 2005, AJ, 129, 1993

McGowan, K. E., et al. 2003, ApJ, 591, 380

McLaughlin, M. A., et al. 2003, ApJ, 591, L135

Michel, F. C. 1973, ApJ, 180, 207

Migliazzo, J. M., et al. 2002, ApJ, 567, L141

Molkov, S. V., et al. 2004, Sov. Astron. Lett., 30, 534

Monet, D. G., et al. 2003, AJ, 125, 984

Muno, M. P. 2007, in American Institute of Physics Conference Series, Vol. 924, American Institute of Physics Conference Series, 166

Muslimov, A. G., & Harding, A. K. 2004, ApJ, 606, 1143

Nolan, P. L., et al. 1993, ApJ, 409, 697

O'Connor, P., Golden, A., & Shearer, A. 2005, ApJ, 631, 471

Oppenheimer, J. R., & Volkoff, G. 1939, Phys. Rev., 55, 374

Özel, F., & Güver, T. 2007, ApJ, 659, L141

Pacholczyk, A. G. 1970, Radio Astrophysics (San Francisco: Freeman)

Pacini, F. 1967, Nature, 216, 567

Pacini, F. 1968, Nature, 219, 145

Page, D. 1998, in The Many Faces of Neutron Stars, ed. R. Buccheri, J. van Paradijs, & M. A. Alpar (Kluwer Academic Publishers), 539

Page, D., Geppert, U., & Weber, F. 2006, Nuclear Physics A, 777, 497

Patel, S. K., et al. 2003, ApJ, 587, 367

Pavlov, G. G., Kargaltsev, O., & Brisken, W. F. 2007, ApJ, 707, submitted (arXiv:0707.3529)

Pavlov, G. G., Kargaltsev, O. Y., Sanwal, D., & Garmire, G. P. 2001a, ApJ, 554, L189

Pavlov, G. G., Sanwal, D., & Zavlin, V. E. 2005, ApJ, submitted, astro-ph/0511364

Pavlov, G. G., Teter, M. A., Kargaltsev, O., & Sanwal, D. 2003, ApJ, 591, 1157

Pavlov, G. G., Zavlin, V. E., & Sanwal, D. 2002, in Neutron Stars, Pulsars, and Supernova Remnants, ed. W. Becker, H. Lesch, & J. Trümper, 273

Pavlov, G. G., et al. 2001b, ApJ, 552, L129

Pavlov, G. G., et al. 2001, ApJ, 552, L129

Pérez-Azorín, J. F., Miralles, J. A., & Pons, J. A. 2006, A&A, 451, 1009

Perez-Azorin, J. F., Pons, J. A., Miralles, J. A., & Miniutti, G. 2006, ApJ, submitted (astro-ph/0603752)

Pivovaroff, M., Kaspi, V. M., & Camilo, F. 2000, ApJ, 535, 379

Pivovaroff, M., Kaspi, V. M., & Gotthelf, E. V. 2000, ApJ, 528, 436

Pivovaroff, M. J., Kaspi, V. M., & Camilo, F. 2000, ApJ, 535, 379

Pivovaroff, M. J., et al. 2001, ApJ, 554, 161

Pons, J. A., & Geppert, U. 2007, A&A, 470, 303

Pons, J. A., Link, B., Miralles, J. A., & Geppert, U. 2007, Physical Review Letters, 98, 071101

Rajagopal, M., Romani, R. W., & Miller, M. C. 1997, ApJ, 479, 347

Ransom, S. M., Eikenberry, S. S., & Middleditch, J. 2002, AJ, 124, 1788

Ransom, S. M., Gaensler, B. M., & Slane, P. O. 2002, ApJ, 570, L75

Raymond, J. C., & Smith, B. W. 1977, ApJS, 35, 419

Rea, N., et al. 2007a, MNRAS, in press (astro-ph/0707.3363)

Rea, N., et al. 2007b, ApJ, submitted (astro-ph/0703128)

Rudak, B., & Dyks, J. 1999, MNRAS, 303, 477

Rybicki, G. B., & Lightman, A. P. 1979b, Radiative Processes in Astrophysics (New York: Wiley)

Seward, F. D., Harnden Jr., F. R., Szymkowiak, A., & Swank, J. 1984, ApJ, 281, 650

Seward, F. D., & Wang, Z.-R. 1988, ApJ, 332, 199

Sieber, W., & Wielebinski, R. 1973, Astrophys. Lett., 13, 225

Slane, P., Helfand, D. J., van der Swaluw, E., & Murray, S. S. 2004, ApJ, 616, 403

Spitkovsky, A. 2004, in IAU Symposium, Vol. 218, Young Neutron Stars and Their Environments, ed. F. Camilo & B. M. Gaensler, 357 (astro-ph/0310731)

Spitkovsky, A. 2006, ApJ, 648, L51

Stappers, B. W., Gaensler, B. M., & Johnston, S. 1999, MNRAS, 308, 609

Tam, C. R., Kaspi, V. M., Gavriil, F. P., & Dib, R. 2007, ApJ, submitted (astro-ph/0707.2093)

Thompson, C., & Beloborodov, A. M. 2005, apj, 634, 565

Thompson, C., & Duncan, R. C. 1993, ApJ, 408, 194

Thompson, C., & Duncan, R. C. 1995, MNRAS, 275, 255

Thompson, C., & Duncan, R. C. 1996, ApJ, 473, 322

Thompson, C., Lyutikov, M., & Kulkarni, S. R. 2002, ApJ, 574, 332

Thompson, D. J., et al. 1999, ApJ, 516, 297

Tiengo, A., et al. 2005, A&A, 437, 997

Tolman, R. C. 1934, Relativity, Thermodynamics, and Cosmology (Relativity, Thermodynamics, and Cosmology, Oxford: Clarendon Press, 1934)

van Adelsberg, M., & Lai, D. 2006, MNRAS, 373, 1495

Vaughan, B. A., et al. 1994, ApJ, 435, 362

Voges, W., et al. 2000, VizieR Online Data Catalog IX/29

Wang, Z., Chakrabarty, D., & Kaplan, D. L. 2006, Nature, 440, 772

Webb, N. A., Olive, J.-F., & Barret, D. 2004, A&A, 417, 181

Weisskopf, M. C., et al. 2000, ApJ, 536, L81

Weisskopf, M. C., et al. 2004, ApJ, 601, 1050

Woods, P. M., et al. 2004a, ApJ, 605, 378

Woods, P. M., et al. 2004b, ApJ, 605, 378

Woods, P. M., & Thompson, C. 2006, in Compact Stellar X-ray Sources, ed. W. H. G. Lewin & M. van der Klis (UK: Cambridge University Press)

Yakovlev, D. G., et al. 2004, Adv. Space Res., 33, 523

Zavlin, V. E., & Pavlov, G. G. 2002, in Neutron Stars, Pulsars, and Supernova Remnants, ed. W. Becker, H. Lesch, & J. Trümper, 263, astro-ph/0206025

Zavlin, V. E., Pavlov, G. G., & Shibanov, Y. A. 1996, A&A, 315, 141